Improving an Atomic Clock on a Chip via Spin-squeezing

Jose Alberto de la Paz

THÈSE DE DOCTORAT
DE SORBONNE UNIVERSITÉ

Spécialité : Physique

École doctorale n°564 : Physique en Île-de-France

réalisée au

Laboratoire Systèmes de Référence Temps-Espace

présentée par

Jose Alberto de la Paz Espinosa

pour obtenir le grade de

DOCTEUR DE SORBONNE UNIVERSITÉ

Sujet de la thèse :

Improving an Atomic Clock on a Chip via Spin-squeezing

soutenue le 27 octobre 2023

devant le jury composé de

M.	Luca PEZZÉ	Rapporteur
M.	Onur HOSTEN	Rapporteur
M.	Christof JANSSEN	Examinateur
M.	Philipp TREUTLEIN	Examinateur
M.	Carlos L. GARRIDO ALZAR	Directeur de thèse
M.	Jakob REICHEL	Directeur de thèse

Souviens-toi que le Temps est un joueur avide
Qui gagne sans tricher, à tout coup ! c'est la loi.
Le jour décroît ; la nuit augmente, souviens-toi !
L'Horloge, Charles Baudelaire

Dedicada a mis padres y a las almas santas
que han estado siempre ahí.

Preface

In an era where precision timing and synchronization are paramount to the functioning of our modern technological society, the development of increasingly accurate timekeeping devices has become imperative. Among these devices, atomic clocks stand as unrivalled timekeepers, setting the gold standard for accuracy and stability in the measurement of time intervals. Over the years, these clocks have evolved from large, laboratory-scale instruments to compact, portable devices, yet their fundamental operating principles have remained rooted in the properties of atoms and their response to electromagnetic fields.

Simultaneously, a couple of decades have passed since the development of atomic sensors, and since then, a lot of improvements have been made. Clever people smash into interesting walls: as physicists have gotten rid of the technical noise, we have reached the fundamental limits of our sensors, notably quantum projection noise (QPN). This limit arises from the fact that our interferometers tend to prepare atoms in such a way that their internal states are independent of each other, limiting the amount of information we can extract from them due to statistical fluctuations. This fundamental limit was reported in the Caesium fountains at Syrte in 1999; it was later reported in a Sagnac interferometer in 2009, and even today, new commercial gravimeters, such as the one recently presented last year by iXblue and Syrte, have reached this barrier.

An important development in the last two decades was the invention and development of atom chips, a concept that not only promises unprecedented levels of miniaturization but also opens the door to novel techniques and capabilities of control of quantum systems. Specifically, we present the second iteration of the Trapped-atom Clock on a Chip (TACC) experiment. This is a metrology-grade clock, upgraded with on-chip fibre-based Fabry-Pérot cavities. We used this cavity-QED platform to create squeezed states of spin as a key enabler in enhancing the precision and performance of compact atomic clocks.

Squeezed states, a manifestation of quantum mechanics, offer a unique way to manipulate the uncertainties associated with atomic measurements. Squeezed states allow us to reduce the uncertainty in one observable (e.g., the phase of the atomic transition) at the expense of increasing the uncertainty in another (e.g., the number of atoms). This trade-off holds the potential to dramatically improve the short-term accuracy of atomic clocks on a chip. In this thesis, we delve into the intricacies of the squeezing mechanisms, particularly via quantum non-destructive (QND) measurements and the practical challenges faced in achieving precision beyond the standard quantum limit (SQL).

It is our hope that this research contributes not only to the field of precision timekeeping but also to the broader spectrum of applications, including navigation, communication, and fundamental tests of physics, all of which rely on the ever-advancing capabilities of atomic clocks.

Structure of the Manuscript

The manuscript is divided into four main parts:

1. **Context.** In this part, we present the field of Quantum metrology, particularly from the point of view of clock and inertial sensors. We provide a general framework for quantum metrology and introduce the notion of spin squeezing. We go into detail about the generation of spin-squeezing via QND measurements and present some technical limitations in TACC-2.

2. **Experimental Apparatus.** In this second part, we present the more relevant components of the experimental apparatus. Some relevant characterisations have been presented elsewhere, and thus, we limit ourselves to what is relevant to the results presented in this manuscript.
3. **Spin Squeezing and Spatial Correlations.** In this part, we present our first results generating spin-squeezed states and their lifetime. We observe and investigate the interplay between the spin dynamics and the external degrees of freedom of the atoms in the phenomenon we have called *amplification* and present a semiclassical model of it.
4. **Clock Operation.** In this final part, we propose a protocol for phase measurements in the presence of amplifications. We investigate different approaches to control such dynamics and apply our model to a phase measurement under QPN.

Additionally, the fifth part contains some additional calculations that, although interesting or relevant, would have disrupted the flow of the text.

Throughout the text, you will find footnotes in the margins. These are meant to add context when confusion may arise. Sometimes, they are also there as a reference for future students who may be getting familiar with the experiment, for example, when naming explicitly device models for a quick search of their documentation. With respect to the figure, I don't adopt any particular convention when placing them on the margins or in the centre of the text; this has been done exclusively from the point of view of aesthetics, *i.e.*, a picture on the margins is not meant to be less relevant as a picture on the main text, at least not intentionally.

Acknowledgement

It would be remiss of me to say that this work comes from my hands alone. I have been surrounded at every step by an army watching my back and to whom I would like to express my gratitude.

I want to start with my thesis supervisor, Carlos Garrido, who, from the beginning, has made me feel like a valuable member of his team. From him, I have received both an appreciation for fundamental physics and a broad perspective on the applications of our profession. His pragmatism has been relevant to me in times of scientific doubt, and his empathy has made the days of personal doubts lighter. Also, I owe a lot to my co-director Jakob Reichel. It is always motivating to see the emotion in a professor's eyes when he explains something to you, from the technical subtleties of a laboratory device to the simple steps of a cooking recipe. Jakob has treated me as an equal when discussing ideas, and I am sure that the exchanges we have had have built my understanding of my project. I apologise to both of you for my character flaws, and thank you for your patience and support. I must not pass up the opportunity to thank my third advisor, the unofficial one, Myles. This thesis stands on the shoulders of his work. From him, I learned the know-how necessary to inherit TACC, from laser construction to electronics. Myles has been present from the time I arrived at my M2 internship until the last day of writing my manuscript, passing through one or two confinements.

I am grateful to my colleagues at the Paris Observatory. At the time, Frank, Sebastian and Arnaud answered questions and made experimental recommendations for problems that seemed daunting at the time, helping me to move forward. A special mention goes to José, from the electronics department, who always found the time to help us with our circuits, and to Michel, who explained to me the doubts that even I did not know I had every time he saw the confusion in my eyes before a circuit. I was also lucky enough to spend some of my afternoons at ENS with the atom chips team. It is always rewarding to go and enjoy a cup of coffee as it should be made. I especially thank Romain and Alice, who were always willing to listen to our doubts and try to help us find the next step when it was not very clear what to do. Let's not forget Etienne, my successor, that has appreciated my dark humor for... some years now.

On a more personal note, let's go with some anecdotes: I arrived in Paris twice, once in 2016 and once in 2018. On both occasions, I arrived with the unconditional support of María, who believed that I could try harder even in the times when I didn't believe it. I thank you for giving me the pen to write this chapter of my life. On my first arrival, I met Manuel Joffre, who was my stay supervisor during my exchange program. He motivated me to do my master's in France, and because of him, I ended up applying to ICFP, which eventually brought me to this project. At the same time, I met his collaborator, Adeline Bonvalet, who, in addition to always having a valuable conversation, taught me his tricks for aligning, which have been very useful to date.

I thank both Faruck Morcos and Rafael Medina, who have been both my mentors and my friends for many years. They have made me the scientist that I am today and have informed many of my ideas on science and education. Thanks to my team at Morcos Lab back in Dallas, particullarly Charisse that have manage to have our projects move foward. I express my utmost appreciation to my friends, the professors at ITESM, Raul and Carlos, who have received my calls over the years and discussed everything and nothing at the same time. I cannot forget Professor Rodolfo Rodriguez, who has inspired me over the years, not only for his pioneering work on cold atoms in Mexico but also for his kindness.

With respect to my friends, All of you are dear to me, and I'm lucky that you are so numerous, although that complicates this task for me.

For those in Mexico. Bendita sea la tecnología que nos ha permitido seguir en contacto. Jacqueline, Mike, Raul, Emilio, Thelma, Diego, Victoria, Manuel, Grace, Andrés, Mariel... ustedes me han escuchado a lo largo de los años, a veces del otro lado del teléfono, a veces del otro lado de la mesa. En crisis y extasis me han sostenido y han estado para escuchar desde mis ideas más extrañas hasta mis proyectos más intrepidos. Mención obligada a Claudette que se encargo de ponerme en forma para poder escribir esta tesis y creer en mi mismo.

He tenido encuentros y reencuentros incidentales con personas esplendidas que me han hecho extrañar mi tierra: Sam que me hizo reenamorarme de mi ciudad, Alfredo que me inspira con su amor literario y romanticismo, El profe Eriko siempre listo con un mezcal para platicar y una guitarra para hacerme soñar, y Cilau que me inspira orgullo por la historia que se escribe en Nayarit. Y Jordi... tu amistad es una de las semillas que más frutos me ha dado sembrar.

For those in Europe. Astrid, bless you and your family that have received me so lovingly when my own is so far. Lukas and Timothée (well, sometimes in France), you have been good and sincere friends and it is always a pleasure to share a movie, a beer or conversation with both of you. Thank you Kathy, for the sporadic, but gorgeous experiences like bouldering and baking. Tamara, te has asegurado de que este bien acompañado y de que disfrutara la playa cuando me hacia falta. Sophia, you have been there for me since the very beginning until today; your presence has always bring me the joy to stay positive on what's ahead. Special mention to all the art-inclined friends I've crossed here like Zeca, Elodie, Claudia, Lorena, Andrea and Marcelo; obrigado!

Marlet, pasan los años y aqui seguimos avanzando, te veo poco, pero te veo con gusto, gracias por tantos años. Erick, tu nunca te vas, es un placer compartir una misma amistad y una misma fe contigo. Carolina, prefiero no decir nada, porque tengo mucho que decir y estos acknowledgement ya parecen una novela; dejemoslo en gracias y lo demás te lo sigo diciendo en los años que vendrán. Catalina y Agustín, ustedes se volvieron mi familia aquí y esta tesis sólo se escribió porque ustedes estuvierón presentes los años que me tomo hacer este doctorado. Cesia, la perdida, te has esforzado por estar en cada uno de mis cumpleaños desde que nos conocemos; no sabes lo mucho que me ha servido tu compañia. Finally, Jonas: I am fortunate to call you my friend; you have received me in your family and you have been there in my crucial moments these years. You are all great.

To my family. Quiero agradecerles a todos. Se que no siempre estoy en contacto, pero cada que nos hemos encontrado me han recibido en sus casas, me han llevado a comer, me han abrazado. Sea en ciudad de México, San Juan de Abajo, Monterrey, San Diego, etc... Siempre me han recibido con amor y se los reconozco. En particular, agradezco a mi tía Susana, a Alexia y a Mariela, que no sólo me han recibido y tratado con cariño a lo largo de los años, sino que han acompañado a mis padres en mi ausencia, lo cual me es invaluable. Gracias también, Carlos, que has hecho un verdadero esfuerzo por ser mi familia independientemente si estamos en el mismo continente o no. A ti, Felix, te agradezco que te has mantenido cerca a pesar de lo lejos que estamos, estoy muy feliz de llamarte mi hermano.

Finalmente, le agradezco a mis padres Felix de la Paz y Guadalupe Espinosa. Ustedes me hicieron lo que soy. Todo el interés que tengo por la ciencia, la pasión por el trabajo y la ambición viene de ustedes. Les reconozco el trabajo que han realizado a lo largo de los años para cuidarme. Ustedes creyeron que yo podía aun cuando no había evidencias y me amaron cada vez que no pude. Los amo y esta tesis está dedicada a ustedes.

Contents

Introduction

Notation

Here, I present a list of the notation used in this manuscript. When adequate, the definition will be expanded in the text; otherwise, it will be assumed to have the usual convention.

Math	
General	
∂_x	Derivative with respect to x
(θ, φ)	Direction described by $\vec{n} = (\sin\theta\cos\varphi, \sin\theta\sin\varphi, \cos\theta)$ in Cartesian coordinates.
Statistics	
$X \sim Y$	Random variable X is distributed according to Y
$X\|Y$	X conditioned on Y
X_i	A realisation of a random variable X
$\mathcal{N}(\mu, \sigma^2)$	Normal distribution with mean μ and variance σ^2
$\mathrm{Var}(Y\|X) = \mathrm{Var}(Y) - \frac{(\mathrm{Cov}(X,Y))^2}{\mathrm{Var}(X)}$	Variance of $Y\|X$ for (X, Y) distributed like bivariate Gaussian variables
Physics	
General	
$\hat{R}_{\hat{n}}(\alpha)$	Rotation operator with angle α around axis $\hat{n}$ in the corresponding space
$\hat{R}(\alpha; \varphi)$	Rotation operator with angle α around axis $(\pi/2, \varphi)$ in the corresponding space
$\hat{\pi}(\vartheta)$, $\frac{\hat{\pi}}{2}(\vartheta)$	π and $\pi/2$ rotation operator around axis $(\cos\vartheta, \sin\vartheta, 0)$ in the corresponding space
PSN	Photon Shot Noise
QPN	Quantum Projection Noise
From experiment	
$\delta\omega$	Cavity Shift in units of angular frequency
p	Probe detuning in units of angular frequency
M	Measured cavity shift
$\frac{\omega_{\mathrm{at}}}{2\pi} = 6.83468261090429(9)$ GHz	Angular frequency for the $F = 1 \to F' = 2$ transition of the hyperfine manifold $5^2\mathrm{S}_{1/2}$ of Rubidium 87[1]
$\frac{\Gamma_{\mathrm{at}}}{2\pi} = 6.065(9)$ MHz	Natural Line Width of the Rubidium 87 D_2 ($5^2\mathrm{S}_{1/2} \longrightarrow 5^2\mathrm{P}_{3/2}$) optical transition[1]
$n_{i,j}, M_{i,j}$	Detected photon number and inferred cavity shift from ith probe of the jth measurement

Part I

Context

1
Quantum Metrology

1.1 Inertial Sensors and Atomic Clocks

1.1.1 A Brief History of Clocks

Since the birth of quantum mechanics in the XX century, experiments to interfere with matter have been proposed to probe the subtleties of this new framework. In 1937 and 1938, Rabi [2] proposed the first interferometric measurements of atomic properties [3]. His work eventually led to the invention of the first atomic clock based on ammonia in 1948 by Harold and Husten [4]. In 1950, Ramsey [5] developed a new interrogation method that, up to this day, is the conceptual basis for all atomic interferometers.

Since the fifties, efforts were made all around the world to develop an atomic standard of time, gaining at least an order of magnitude per decade [6]. This led to the redefinition of the second in 1968, referenced to the frequency of the ground state hyperfine transition in the caesium-133 atom[7]. The development of laser and cooling technologies[8] allowed for the development of caesium fountains in the nineties. The first of such devices, developed in Paris, reached record accuracies, at the time, of 3×10^{-15}[9]. More recently, new technologies such as optical clocks [10–12] have reached stabilities on the order of 10^{-18}, bringing with them new technological challenges and new physics[13].

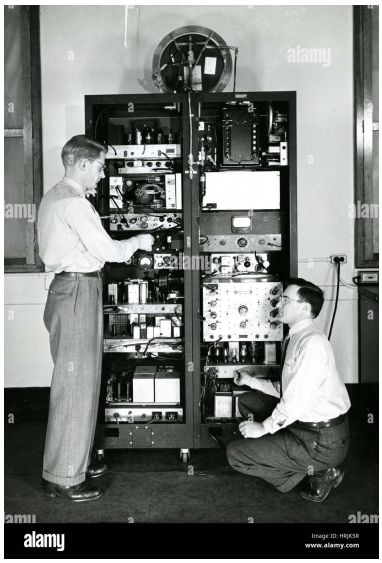

Figure 1.1: Photograph of the back side of ammonia maser, the first molecular clock with B. F. Husten and E. D. Heberling.

1.1.2 On Portability and Inertial Sensors

The use of clocks is not exclusive to the creation of primary time references. Different applications may require different sizes of clocks, notably in the interest of portability. Modern commercial and portable clocks have stabilities on the order of 10^{-12}, and it is of particular interest to increase this stability for at least an order of magnitude while keeping a portable device. Some proposals have reached stabilities of 10^{-13} in the short term and gaining at least an order of magnitude after long integration [14–18]. Apart from building clocks, Bordé [19] propose the use of atomic recoil in an interferometer to measure both rotations and accelerations as frequency shifts in Ramsey fringes. This principle was demonstrated only two years

later[20–24]. Since then, numerous teams around the world have worked to improve both the accuracy and sensitivity of such sensors. This research has been motivated by the practical applications of such technologies in inertial guidance, geophysics, and fundamental physics [25].

Although we do not deal with inertial sensors in this thesis, we consider it relevant to mention them as they face similar challenges to compact clocks in terms of portability and the use of resources. Particularly, both compact atomic clocks and inertial sensors may benefit from the use of entangled states to improve their sensitivity, as will be discussed in section 1.4. The approach of using these states is the main subject of this manuscript. For reference on cold atom sensors, we direct the reader to [26] as a general reference of the field; [27] discusses more directly the problem of portability and transport. Finally, [25] gives a review of the field, particularly focusing on the efforts of the last 10 years.

1.2 Atom chips and Rubidium Trapped Clocks

An atom chip is a specialized device used for the manipulation and control of atoms using electromagnetic fields. It typically consists of a microfabricated substrate, onto which extremely small and precise wire structures are patterned. These wire structures generate magnetic fields and electric potentials that can trap, guide, and manipulate clouds of ultra-cold atoms. Additionally, it is possible to apply mirror coating to the chip surface, allowing for the formation of magneto-optical traps (MOT) near the surface of the chip [28]. The operation of an atom chip relies on the principles of magnetic trapping. When a current flows through the wires on the chip, it creates a magnetic field distribution around them. This magnetic field can be tailored with the help of external bias fields to create complex geometries as traps for the atoms. By adjusting the currents in real time, one can manipulate the position and motion of the trapped atoms. A pedagogical explanation of the most common trap geometries is presented in the thesis by Reinhard [29].

Atom chips have found widespread use in experiments involving cold atoms [30]. They have been used to study properties of Bose-Einstein condensates [31–33], and are also crucial for developing practical applications in quantum information [34] and atom interferometry [35]. A complete overview of these technologies can be found in [28] and [30].

1.2.1 A Trapped Rubidium Clock

We chose Rubidium 87 (^{87}Rb) as the atomic species for this experiment. The reduced interatomic interaction, compared to Cs, results in a reduction of the collisional shift, facilitating both trapping and cooling. The hyperfine splitting of ^{87}Rb is in the microwave range, making it useful as a secondary standard. Particularly, we make

use of the two-photon transition between the magnetically trappable states. $|\downarrow\rangle \equiv |F = 1, m_F = -1\rangle$ and $|\uparrow\rangle \equiv |F = 2, m_F = 1\rangle$; this transition is shown in figure 1.2 c) . An important advantage of such states is that their energy difference reaches a minimum at a "magic field" B_m where the transition frequency is first-order insensitive to the magnetic field, as shown in figure 1.2 b).

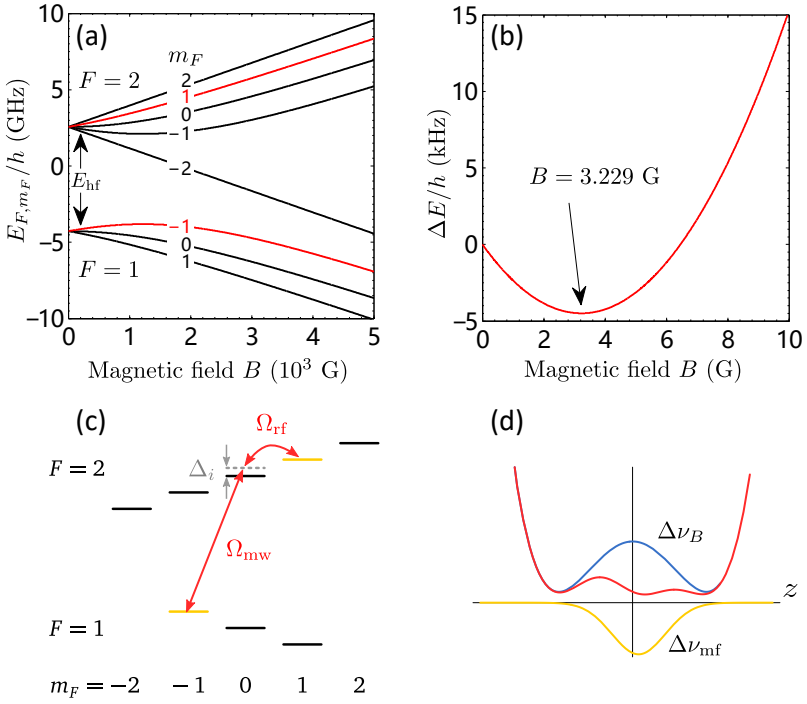

Figure 1.2: The Rb clock transition for trapped atoms and pseudo-magic trap in; adapted from [36]. a) Energy of the $5^2S_{1/2}$ hyperfine ground states of ^{87}Rb in a magnetic field, calculated using the Breit-Rabi formula [1]. b) Energy difference between the clock states $|\downarrow\rangle$ and $|\uparrow\rangle$ showing a magic field at $B_m = 3.229$ G. c) Two-photon transition implemented in TACC, with $\Delta_i = 500$ kHz. d) Mutual compensation between the inhomogeneous Zeeman shift $\Delta\nu_B$ and the mean-field collisional shift $\Delta\nu_{\rm mf}$, at the bottom field slightly lower than B_m ($\Delta B < 0$). The compensation is slightly compromised due to gravitational sag that shifts the cloud away from the trap centre.

Zeeman shift. More precisely, in a harmonic trap with trapping frequencies ω_x, ω_y and ω_z, the Zeeman shift Δ_B is described by [37]:

$$\Delta\nu_B(\vec{r}) = \frac{bm^2}{\mu_{\rm B}^2}\left(\omega_x^2 x^2 + \omega_z^2\left(y^2 + z^2\right) - 2gz + \Delta B\frac{\mu_{\rm B}}{m}\right)^2, \qquad (1.1)$$

where m is the atomic mass, g the gravitational acceleration, $\mu_{\rm B}$ the Bohr magneton, $\Delta B = B - B_m$, and $b \approx 431.356\text{Hz/G}^2$. The second to last term is the shift due to gravitational sag. The curvature of the shift at the trap centre can have different signs depending on the bias field ΔB.

Density shift. For cold thermal clouds, we consider that the ensemble can be treated classically, and the atomic density is given by the Maxwell-Boltzmann distribution at temperature T[38]:

$$n(\vec{r}) = \frac{N}{(2\pi)^{3/2}x_T y_T z_T}\exp\left[-\frac{x^2}{2x_T^2}\right]\exp\left[-\frac{y^2}{2y_T^2}\right]\exp\left[-\frac{z^2}{2z_T^2}\right] \qquad (1.2)$$

where N is the number of atoms, k_B the Boltzmann constant, and $x_T = \sqrt{k_{\rm B}T/\left(m\omega_x^2\right)}$ (similar for y_T and z_T). The collision between

atoms induces a frequency shift that depends on this density. A mean-field treatment leads to a negative shift $\Delta\nu_{\mathrm{mf}} \propto n(\vec{r})$[39].

Partial Shift Compensation. While the collisional shift is stronger towards the cloud centre (a positive curvature), the Zeeman shift can be tuned ($\Delta B < 0$) to have the opposite curvature that almost cancels the inhomogeneity close to the trap centre. The imperfections are twofold: different forms of the magnetic potential (quadratic) and the density (Gaussian), and the fact that gravitational sag displaces the centre of the density profile away from that of the magnetic potential (See figure 1.2).

1.3 Quantum Metrology

The primary tool behind measuring physical quantities is a probe interacting with the system of interest; such interaction modifies the state of the probe in a sensible, well-characterised and controlled manner. Quantum metrology uses the quantum nature of the involved system via non-classical states and entanglement in order to improve the measurement precision. Notably, this can be done by mapping the quantity we are interested in into a phase shift θ to be determined by interferometric techniques.

Grosso modo, an initial N-particle state, described by a density operator (matrix) $\hat{\rho}(0)$ is produced and then is subjected to an evolution $\partial_t\hat{\rho} = i[\hat{\rho}, \hat{H}_\varphi]$ induced by a Hamiltonian $\hat{H}_\varphi$ that depends on the quantity we want to measure φ[1]. This procedure encondes φ into a state that depends on it as $\hat{\rho}(0) \mapsto \hat{\rho}(t_f) = \hat{\rho}_\varphi$. A set of measurements[2] is then performed onto the system, yielding an ensemble of nR measurement results $\vec{\mu} = \{\mu_1, \mu_2, \cdots\}$. This set of measurement results is then used to calculate an estimate $\Theta(\vec{\mu})$ of the phase shift [41]. If the particles are independent, the phase sensitivity, *i.e.*, standard deviation $\Delta\varphi$, scales as $\frac{1}{\sqrt{N}}$. This corresponds to the classical scaling of independent variables, the Standard Quantum Limit (SQL) [42]. This limit has been demonstrated in different metrology scale instruments [43]. However, taking advantage of entangled states, the SQL can be overcome in metrologically useful manners [41, 44]. The most relevant metrological states in this project are the spin-squeezed states, which will be introduced in the following sections.

[1] $\hbar = 1$ for this section.

[2] General measurements are described by probability-operator-valued measures (POVM) [40], a set of operators $\hat{E}_r$ associated with a set of results r such that $\hat{E}_r \geq 0$ and $\sum_r \hat{E}_r = \mathbb{I}$. Given a state described by the density operator $\hat{\rho}$, the probability of obtaining a result r is given by $P(r) = \mathrm{Tr}\{\hat{\rho}\hat{E}_r\}$

1.3.1 Spin Representation and Collective Spin

Single atom. We consider a two-level system with a particular basis $\{|\uparrow\rangle, |\downarrow\rangle\}$. This represents the two levels of an atomic system susceptible to a phase accumulation correlated to the physical quantity to measure. For example, they could be two hyperfine states of an atom, as in the case of an atomic clock, to measure the detunings of a local oscillator with respect to the energy difference of these states. Alternatively, those could be two momentum states, as with inertial sensors that could measure rotations and accelerations. This identi-

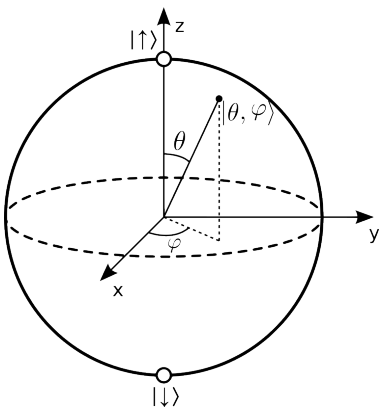

Figure 1.3: Bloch sphere representation of a single qubit. The latitude of a particular state represents the z component of the spin and is related to the amplitude of each state in the $\{|\uparrow\rangle, |\downarrow\rangle\}$ basis. The longitude relative to x represents the relative phase between both states.

fication allows us to treat the system as an effective spin-1/2 where each normalised pure-state can be parametrised as

$$|\theta,\varphi\rangle = \cos\frac{\theta}{2}e^{-i\frac{\varphi}{2}}|\uparrow\rangle + \sin\frac{\theta}{2}e^{i\frac{\varphi}{2}}|\downarrow\rangle = \begin{pmatrix}\cos\frac{\theta}{2}e^{-i\frac{\varphi}{2}}\\ \sin\frac{\theta}{2}e^{i\frac{\varphi}{2}}\end{pmatrix}, \tag{1.3}$$

where $0 \leq \theta \leq \pi$, $0 \leq \varphi \leq 2\pi$. This parameterisation allows us to assign a point on the unitary sphere $\vec{n}(\theta,\varphi) = (\sin\theta\cos\varphi, \sin\theta\sin\varphi, \cos\theta)$ to each effective spin-1/2. This parametrisation[3], named the Bloch sphere, allows for a representation as the one shown in Fig 1.3, where each point corresponds to a spin state. Furthermore, any unitary transformation on the system can be regarded as a rotation on the sphere around an axis $\vec{n}$ and by an angle α, acting on the spin Hilbert space through the representation[4]:

$$\hat{R}_{\vec{n}}(\alpha) = e^{-i\frac{\alpha}{2}\vec{\sigma}\cdot\vec{n}} = \cos\left(\frac{\alpha}{2}\right)\mathbb{I} - i\sin\left(\frac{\alpha}{2}\right)\vec{\sigma}\cdot\vec{n}. \tag{1.4}$$

For later use, we introduce the following notation:

$$\hat{\pi}(\vartheta) \equiv \hat{R}_{\vec{n}_\vartheta}(\pi) = \begin{pmatrix}0 & e^{-i\vartheta}\\ e^{i\vartheta} & 0\end{pmatrix},$$
$$\frac{\hat{\pi}}{2}(\vartheta) \equiv \hat{R}_{\vec{n}_\vartheta}\left(\frac{\pi}{2}\right) = \begin{pmatrix}\frac{1}{\sqrt{2}} & -\frac{i}{\sqrt{2}}e^{-i\vartheta}\\ -\frac{i}{\sqrt{2}}e^{i\vartheta} & \frac{1}{\sqrt{2}}\end{pmatrix},$$
$$\hat{\phi} \equiv \hat{R}_{\vec{z}}(\phi) = \begin{pmatrix}e^{-i\frac{\phi}{2}} & 0\\ 0 & e^{i\frac{\phi}{2}}\end{pmatrix},$$

where $\vec{n}_\vartheta = \vec{n}(\pi/2,\vartheta)$ and $\vec{z} = \vec{n}(0,0)$

Many atoms. To describe an ensemble of atoms, we consider the collective spin vector $\hat{\vec{S}} = \sum_i^N \hat{\vec{s}}_i$ with $\hat{\vec{s}}_i = \frac{1}{2}\left(\hat{\sigma}_x^{(i)}, \hat{\sigma}_y^{(i)}, \hat{\sigma}_z^{(i)}\right)$, where the $\hat{\sigma}_{x,y,z}^{(i)}$ are Pauli matrices for the ith atom. The measurement of the ensemble's z component is given by the population difference $\langle S_z\rangle = (N_\uparrow - N_\downarrow)/2$, where $N_\uparrow$ and $N_\downarrow$ are the atom numbers in $|\uparrow\rangle$ and $|\downarrow\rangle$ states, respectively. The collective spin vector, as such defined, obeys the angular momentum algebra with the expected commutation relationships between its components.

The simplest pure state that can be created from an ensemble of N atoms is called a Coherent Spin State (CSS) and consists of all atoms prepared along the same axis in spin space. For an axis $\vec{n} = (\sin\theta\cos\varphi, \sin\theta\sin\varphi, \cos\theta)$, we defined the corresponding CSS as

$$|\theta,\varphi;N\rangle = \bigotimes_i^N |\theta,\varphi\rangle_i, \tag{1.5}$$

with $\left\langle\hat{\vec{S}}\right\rangle = \frac{N}{2}(\sin\theta\cos\varphi, \sin\theta\sin\varphi, \cos\theta)$. These collective states can be represented in a generalised Bloch sphere through a quasi-probability distribution of the state, as described by Pezzè et al. [41]. For the case of a CSS with a large N, this distribution approximates a Gaussian around the expected value of the state. We pictorically[5] represent this in figure 1.4.

[3] In the text, we will use the physics convention of Spherical coordinates: r for the radial distance r, polar angle θ, and azimuthal angle φ.

[4] Here, $\vec{\sigma}\cdot\vec{n}$ denotes $\sum_i \sigma_i n_i$, where σ_i stands for the three Pauli matrices. For more details, one can refer to Chapter 3 of Sakurai and Napolitano [45]

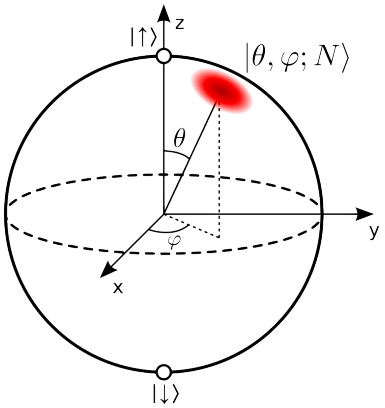

Figure 1.4: Generalised Bloch sphere representation of a CSS. The centre of the distribution represents the expected value of the collective spin operator $\hat{\vec{S}}$. The distribution around the centre of the state represents the uncertainty of measurements in the corresponding quadrature for the case of a CSS. More generally, this representation is the pictorial representation of some quasi-distribution of the atomic state projected on the unitary sphere[41].

[5] Unless otherwise specified, the Bloch sphere representation of many-atom states we use is mostly pictorial.

The generalised Bloch sphere representation allows us to exploit our intuitions and notions of rotations. If we rotate every spin around the same axis $\vec{n}$ by an angle α, we can represent this through a collective rotation operator $\bigotimes_i^N e^{-i\frac{\alpha}{2}\vec{\sigma}_i\cdot\vec{n}} = e^{-i\alpha\vec{S}\cdot\vec{n}}$. This type of operator describes most classical operators used in atomic interferometers. The type of interactions used to create superpositions addresses the atoms independently from each other, rotating them along the same axis[6]. For all practical purposes, when calculating collective rotations, we can manipulate the single spin state and then consider the effect on the complete state. However, as discussed below, other evolutions can also be induced through interactions between the spins or via interactions with external systems.

[6] The case of inhomogeneous coupling can be treated via an effective spin of reduced length $\mathcal{S}$ as described by Hu et al. [46].

Second quantisation approach. The Dicke states are a natural basis for the collective spin state formed by the states that are symmetric under particle exchange for a given atom number N. These are the common eigenbasis $|S, S_z\rangle$ of the $\hat{S}^2, \hat{S}_z$ operators, with $S = \frac{N}{2}$ and $S_z \in \{-S, \cdots, S\}$. The CSS can be written in terms of Dicke states as [47]:

$$|\theta, \varphi; N\rangle = \sum_{S_z=-S}^{S} C(S_z, \theta, \varphi)\, |S, S_z\rangle\,, \tag{1.6}$$

$$C(S_z, \theta, \varphi) = \binom{2S}{S+S_z}^{1/2} \left(\sin\frac{\theta}{2}\right)^{S+S_z} \left(\cos\frac{\theta}{2}\right)^{S-S_z} e^{-i(S+S_z)\phi}. \tag{1.7}$$

This basis allows us to consider S_z as symmetrical excitations with well-defined population differences. Furthermore, in addition to the previous angular momentum formalism of spin states, we can use second quantisation and introduce bosonic operators a, b for the states $|\uparrow\rangle$ and $|\downarrow\rangle$ respectively[7]. Spin operators can now be written as:

[7] For these states $\hat{N}_\uparrow = a^\dagger a$, $\hat{N}_\downarrow = b^\dagger b$ and
$\left[a, a^\dagger\right] = 1, \quad \left[b, b^\dagger\right] = 1, \quad [a, b] = 0.$

$$\hat{S}_x \equiv \frac{1}{2}\left(a^\dagger b + b^\dagger a\right), \tag{1.8}$$

$$\hat{S}_y \equiv \frac{1}{2i}\left(a^\dagger b - b^\dagger a\right), \tag{1.9}$$

$$\hat{S}_z \equiv \frac{1}{2}\left(a^\dagger a - b^\dagger b\right). \tag{1.10}$$

This formalism will allow us to deal with varying numbers of atoms in sections 2.3.3 and 12.2[48, 49].

1.3.2 *Ramsey Interferometer*

A Ramsey interferometer is a measurement scheme where an atomic ensemble is initially prepared in a coherent superposition along the equator of the Bloch sphere. Then, the ensemble state can accumulate a phase φ during a free evolution time t_d. In the case of an atomic clock, the phase that we care about is proportional to the detuning of the local oscillator Δ_{LO} with respect to the atomic transition: $\varphi = \Delta_{\mathrm{LO}} t_d$. Finally, a second rotation of the internal state turns

this phase into a population difference that can be measured. This sequence of steps can be modelled by a pair of rotations separated by a time t_d. In the case of relatively small detuning, this corresponds to $\pi/2$-rotations. Different combinations of the relative phases of these pulses allow us to make the final measurement more or less sensitive to the value of interest. Take, for example, the sequence where the two pulses have a phase difference of π:

$$\frac{\hat{\pi}}{2}(\pi+\vartheta)\cdot\hat{\phi}\cdot\frac{\hat{\pi}}{2}(\vartheta)=\hat{R}_{\vartheta+\pi/2}(\phi)\,.$$

This sequence is illustrated in figure 1.5, where the accumulated phase transfers into a population difference. For an initial state $|\downarrow\rangle^{\otimes N}$ and $\vartheta=-\frac{\pi}{2}$, the final state of the interferometer is $|\pi-\varphi,\frac{\pi}{2};N\rangle$, for which

$$\langle S_z\rangle=-\frac{N}{2}\cos\varphi,\qquad \Delta S_z=\frac{\sqrt{N}}{2}\sin\varphi. \tag{1.11}$$

From equation (1.11), the phase uncertainty is given by:

$$\Delta\varphi=\frac{\Delta S_z}{\frac{\mathrm{d}\langle S_z\rangle}{\mathrm{d}\varphi}}=\frac{1}{\sqrt{N}}. \tag{1.12}$$

This noise level is the Standard Quantum Limit (SQL), to be discussed more generally in the next section.

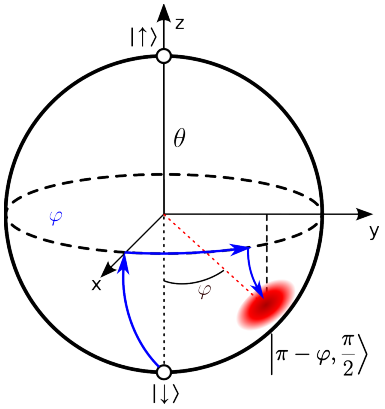

Figure 1.5: Ramsey sequence where the two $\pi/2$ pulses that open and close the interferometer have opposite phases.

1.4 Fisher Information and Standard Quantum Limit

Whenever we consider a separable spin state $|\psi\rangle=\bigotimes_i^N|\psi_i\rangle$, a CSS, for example, we can treat the measurements performed on it as an ensemble of independent measurements. From this, we expect the information we obtain to be limited by the statistics of uncorrelated random variables that scale with the squared root of the number of variables; for the interferometer, this is the number of atoms.

Fisher Information. More generally, given a general quantum state and a POVM $\{\hat{E}_\mu\}$, we may define a probability distribution over the results μ, conditioned on the encoded parameter φ as $P(\mu|\varphi)=\mathrm{Tr}\left\{\hat{\rho}_\varphi\hat{E}_\mu\right\}$. From this distribution, we may build the *Fisher information* defined as;

$$F(\varphi)\equiv\sum_\mu P(\mu|\varphi)\left(\frac{\mathrm{d}\ln P(\mu|\varphi)}{\mathrm{d}\varphi}\right)^2, \tag{1.13}$$

which is a measure on how much the distribution $P(\mu|\varphi)$ changes as the parameter φ changes [40]. More intuitively, the Fisher information describes how easy it is to distinguish two different values of the parameter ϕ from the results we obtained by measuring them. With this quantity, it is possible to bound the uncertainty on the inference on the parameter φ for one measurement as:

$$\Delta\varphi\geq\Delta\varphi_{\mathrm{CR}}=\frac{1}{\sqrt{F(\varphi)}}. \tag{1.14}$$

This bound is known to be saturated by the Maximum Likelihood estimator of φ value, and it is known as the Cramér-Rao Bound.

Information relevant bounds. Furthermore, it is possible to extend this notion by considering the set of all possible POVM on $\hat{\rho}_\varphi$, giving rise to an upper bound on the Fisher information known as the Quantum Fisher Information (QFI):

$$F_Q[\hat{\rho}_\varphi] = \max_{\{\hat{E}_\mu\}} F(\varphi).$$

where the maximization is taken over the set of all possible POVMs. The QFI tells us about the potential of a state described by the density matrix $\hat{\rho}_\varphi$ to give information about the quantity φ when choosing the best possible measurement scheme. Therefore, by construction,

$$\Delta\varphi_{\mathrm{CR}} \geq \Delta\varphi_{\mathrm{QCR}} = \frac{1}{\sqrt{F_Q[\hat{\rho}_\varphi]}}. \tag{1.15}$$

Two relevant bounds have been shown by Pezzé and Smerzi [44] to be the Heisenberg limit:

$$F_Q[\hat{\rho}_\varphi] \leq N^2, \tag{1.16}$$

valid for any spin state, giving the maximum phase sensitivity. On the other hand, we found that for separable states

$$F_Q[\hat{\rho}_\varphi] \leq N. \tag{1.17}$$

Pure states saturate these bounds and are a more general version of the SQL we described above. Violations of this bound are criteria for entanglement[8]. Furthermore, this construction allows us to distinguish which states are helpful or not for metrology. Some of the useful entangled states that are of common interest are Dicke states, NOON states[9], and squeezed states, to be introduced in the next section.

[8] It should be noted that not all entangled states reduce the uncertainty on the phase estimations, but the only violations for this bound can come from entangled spin states.

[9] Also known as Greenberger-Horne-Zeilinger (GHZ), defined as $\frac{|\uparrow\rangle^{\otimes N}+|\downarrow\rangle^{\otimes N}}{\sqrt{2}}$

Figures of merit. With these bounds, we can introduce three relevant figures of merit. Maybe the most evident metric in this context is the metrological gain, $1/\zeta^2$ with respect to the QFI [50]:

$$\zeta^2 = \frac{N}{F_Q[\hat{\rho}_\varphi]}.$$

However, in practice, we measure population difference, *i.e.*, S_z. Thus, we prefer the notion of number squeezing, which compares the variance of the adequate spin component with the result we expect from an optimal pure and separable state, a CSS:

$$\xi_N^2 = \left(\frac{\Delta S_z}{\Delta S_z|_{CSS}}\right)^2 = \frac{4\,(\Delta S_z)^2}{N}. \tag{1.18}$$

Finally, an intermediate between these two metrics is the Wineland parameter, which considers the "available resources", including the coherence of the state via the contrast $\mathcal{C}$ of the Ramsey fringes:

$$\xi^2 = N\frac{(\Delta S_z)^2}{\left|\left\langle \vec{S}\right\rangle\right|^2} = \frac{4\,(\Delta S_z)^2}{N\mathcal{C}^2}. \tag{1.19}$$

We note that this quantity is the actual metrological gain we obtained from using this particular state [51–53].

2
Spin Squeezing

2.1 Spin Squeezed States

Consider a collective spin state prepared along a direction $\vec{n}(\pi/2, \varphi)$ axis in such a way that $\langle \hat{S}_{\vec{n}} \rangle \approx |\left\langle \vec{S} \right\rangle| = S$. Given the two orthogonal directions $\vec{\varphi}$ and $\vec{z}$, both perpendicular to $\vec{n}$, the uncertainty principle implies that

$$(\Delta S_\varphi)^2 (\Delta S_z)^2 \geq \frac{1}{4} S^2 = \frac{N^2 \mathcal{C}^2}{16}. \tag{2.1}$$

Rewriting equation (2.1) in terms of the squeezing parameter, we get

$$\frac{4(\Delta S_\varphi)^2}{N\mathcal{C}^2} \frac{4(\Delta S_z)^2}{N} = \xi_\varphi^2 \cdot \xi_{N,z}^2 \geq 1. \tag{2.2}$$

This tells us that any metrological gain on the phase measurement is accompanied by an increase in the uncertainty of the z-component of the spin ensemble. Such states are referred to as spin-squeezed states (SSS). They were first introduced by Wineland et al. [51] in 1992, and Kitagawa and Ueda [53] proposed its application to interferometry. These are the primary states of interest for this work, and in the following subsection, we discuss the mechanism for generating them and their characterisation.

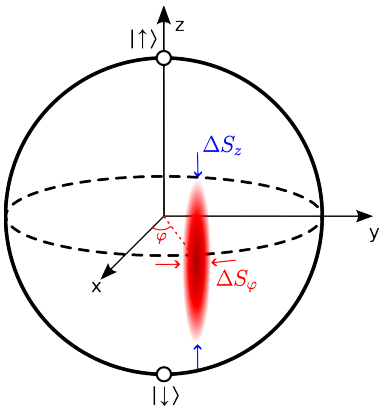

Figure 2.1: Bloch sphere representation of an SSS. In red, we see the squeezed quadrature and in blue, the anti-squeezed component, in this case, S_Z.

2.1.1 *Squeezing via Interactions*

The first mechanism for generating squeezing is via spin interactions [53]. Some of the typical Hamiltonians to achieve this are of the form:

$$\begin{aligned} H_{1-\text{axis}} &= -\hbar\chi \hat{S}_z^2, && \text{One-axis twisting;} \\ H_{2-\text{axis}} &= \hbar\chi \left(\hat{S}_y^2 - \hat{S}_x^2 \right), && \text{Two-axis counter twisting;} \\ H_{\text{TaT}} &= \hbar\Omega_{\text{HF}} \hat{S}_x + \hbar\chi \hat{S}_z^2, && \text{Twist and turn,} \end{aligned}$$

where the χ is the shearing parameter, describing the strength of spin-spin interactions, and a coupling strength Ω_{HF} given by the microwave and radio-frequency radiation, this is a rotation term corresponding to an external drive. Quadratic Hamiltonians as such, particularly the one-axis twist and the twist-and-turn, can be and have

been achieved experimentally before through atomic collisions[54–60]. Alternatively, one can introduce interactions through the coupling with light. For example, we can couple the atomic ensemble with the mode $\hat{c}$ of a cavity with Hamiltonians including the term

$$H_{\text{light-atom}} = -\hbar\Omega\hat{n}_c\hat{S}_z, \tag{2.3}$$

where $\hat{n}_c$ is the photon number operator and Ω is the lightshift per single photon. The intracavity photon number depends on the spin state, leading to an effective quadratic term on spin[61]. Indeed, the atoms inside the cavity produce a refractive index shift in the cavity resonance, therefore modifying the ability to couple light into the cavity.

A complete treatment of this approach has been detailed elsewhere [50, 53, 61]. The basic idea is that, in a rotating frame of reference, given a Hamiltonian $\hbar\Delta_{\text{LO}}\hat{S}_z$, the spin state precess at an angular speed of Δ_{LO}. A Hamiltonian with a second-order term, such as $\hbar(\Delta_{\text{LO}} + \chi\hat{S}_z)\hat{S}_z$ has the effect of changing the rate of rotation of the state to $\Delta_{\text{LO}} + \chi\hat{S}_z$, making it dependent on the z spin-component. This mechanism produces the stretching of its distribution, as depicted in figure 2.2, squeezing the state along an oblique quadrature.

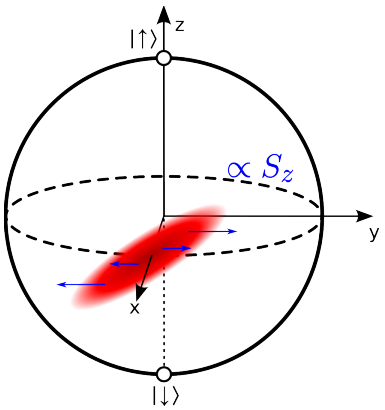

Figure 2.2: Pictorical representation of the one-axis twist action. The rotation speed in the Bloch sphere depends on the value of the S_z component, effectively stretching the collective spin state.

2.2 Measurement Generated Squeezing

This approach consists of entangling another quantum system with the atomic ensemble, usually a cavity light mode. Measuring the light state then allows one to infer information about the atomic state, reducing the uncertainty on a spin component without destroying the state coherence. The amount of information obtained by this method will be limited by the fundamental fluctuations of the light state used. In our system, as we will se below, we have a superposition of coherent states condition on the atomic state; this sets our fundamental limit at Photon Shot Noise (PSN[1]). We utilize this method for creating squeezing and will thoroughly explain the involved steps. The following treatment is adapted from [62].

Consider a spin ensemble with two hyperfine ground states equally coupled to an excited state $|e\rangle$, with opposite detunings $\pm\Delta$ via a single cavity mode described by $\hat{c}$ and effective linewidth γ (HWHM). Adiabatic elimination of the excited level in the low-saturation regime leads to the evolution governed by the Hamiltonian $\hbar(\delta + \Omega)\hat{S}_z\hat{n}_c + i\eta_p(\hat{c}^\dagger - \hat{c})$, where δ is the probe detuning with respect to the empty-cavity, η_p is the cavity pumping rate and $\frac{\Omega}{2\gamma}$ is the single-photon light shift. Initially, the atoms are prepared in a coherent state on the equator of the Bloch sphere; from equation (1.7):

$$|\varphi; S\rangle = \sum_m C_m(\varphi)\,|m\rangle\,, \qquad m \in [-S, S] \tag{2.4}$$

where $C_m(\varphi) = \sqrt{\binom{2S}{S+m}}2^{-S}e^{-i(S+m)\varphi} \approx (\pi S)^{-1/4}e^{-\frac{m^2}{2S} - i(S+m)\varphi}$. Light is then sent at a pumping rate η_p. There are no light-light interactions for a small enough pumping rate ($\eta_p^2/\gamma^2 \ll 1$), and the cavity

[1] A coherent state $|\alpha\rangle$, has the statistics of Poisson variable when measuring photon number, in particular, its mean and variance follow the relation:

$$\langle n\rangle = \text{Var}\,(n) = |\alpha|^2$$

The fluctuations when measuring the photon umber n for such states are named Photon Shot Noise.

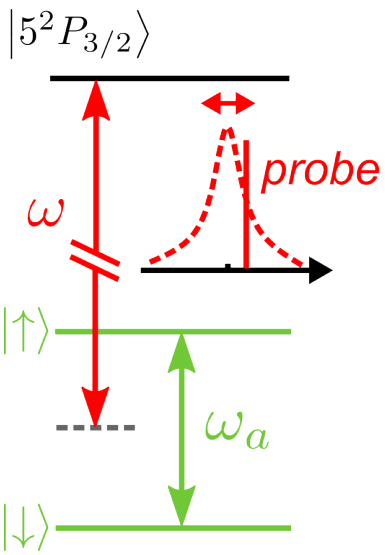

Figure 2.3: Energy level structure and the cavity-probing scheme for Rubidium 87.

reaches a superposition of coherent states conditioned to the atomic state for times larger than γ^{-1}. Written in terms of the intracavity light field, the state after interaction will be given by

$$|\psi_{\text{at+lightin}}\rangle = \sum_m C_m(\varphi)\,|m\rangle \otimes |\alpha_{in,m}\rangle\,, \qquad m \in [-S, S]$$
$$\alpha_{in,m} = \frac{\eta_p}{\gamma + i(\delta + m\Omega)}.$$

Considering a decay rate due to transmission κ_t and symmetrical losses[2] κ_t, the state of the system after transmission through the cavity is:

[2] For a pair of identical mirrors with transmission $\mathcal{T}$ and losses $\mathcal{L}$, we have $\kappa_t = 2\gamma\frac{\mathcal{T}}{\mathcal{T}+\mathcal{L}}$

$$|\psi_{\text{at+light}}\rangle = \sum_m C_m(\varphi)\,|m\rangle \otimes |\alpha_m\rangle\,, \qquad m \in [-S, S]\,, \tag{2.5}$$
$$\alpha_m = \left(\frac{\kappa_t}{4\gamma}\right)\frac{\eta_p}{\gamma + i(\delta + m\Omega)}. \tag{2.6}$$

Photon detection. We focus now on the detection of the light component of our state. The light component is measured with a photon counter with efficiency η. This can be modelled with a beamsplitter B with transmittance η at the output port of the cavity[63]. We take a two-mode light-state $|\alpha, 0\rangle$, where $|\alpha\rangle$ represents the light state to be (imperfectly) detected and $|0\rangle$ is the vacuum state entering the second port of the beamsplitter. In this two-mode representation, B can be represented by a unitary matrix

$$B = \begin{pmatrix} \cos\vartheta & i\sin\vartheta \\ i\sin\vartheta & \cos\vartheta \end{pmatrix}, \qquad \eta = \cos^2\vartheta.$$

When acting on a bi-coherent state $|\alpha, \beta\rangle$, the action of the beam splitter can be calculated by applying B directly to the amplitudes of the coherent states individually[64]:

$$B \cdot |\alpha, \beta\rangle = |\alpha', \beta'\rangle\,, \quad \text{where} \begin{pmatrix} \alpha' \\ \beta' \end{pmatrix} = B^{-1} \begin{pmatrix} \alpha \\ \beta \end{pmatrix}.$$

Applying this to the cavity mode, we obtain the output state before measurement:

$$|\psi_{\text{final}}\rangle = \sum_m C_m(\varphi)\,|m\rangle \otimes |\alpha_m \cos\vartheta, -i\alpha_m \sin\vartheta\rangle\,, \tag{2.7}$$

where we have access only to the photon counts of the first mode, while the rest are lost. Finally, to describe the final state in the cloud, we first trace over the lost photons[3]:

[3] We simplify the second line using $\sum_n |n\rangle\langle n| = \mathbb{1}$. For simplicity, we drop the explicit dependence on φ

$$\begin{aligned}
\hat{\rho}_{\text{measurable}} &= \text{Tr}_{\text{lost}}\left\{|\psi_{\text{final}}\rangle\langle\psi_{\text{final}}|\right\} \\
&= \sum_{n,m,m'} C_m \bar{C}_{m'} \langle n \,|\, -i\alpha_m \sin\vartheta\rangle \langle -i\alpha_{m'} \sin\vartheta \,|\, n\rangle\, |m; \alpha m \cos\vartheta\rangle \langle m'; \alpha m' \cos\vartheta| \\
&= \sum_{m,m'} C_m \bar{C}_{m'} \langle -i\alpha_{m'} \sin\vartheta \,|\, -i\alpha_m \sin\vartheta\rangle\, |m; \alpha m \cos\vartheta\rangle \langle m'; \alpha m' \cos\vartheta| \\
&= \sum_{m,m'} \mathcal{A}_{m,m'}\, |m; \alpha_m \cos\vartheta\rangle \langle m'; \alpha_{m'} \cos\vartheta|\,,
\end{aligned}$$

where we introduce the matrix element

$$\begin{aligned}\mathcal{A}_{m,m'} =& C_m \bar{C}_{m'} \left\langle -i\alpha_{m'} \sin\vartheta \right| \left. -i\alpha_m \sin\vartheta \right\rangle \\ \approx& \frac{1}{\sqrt{\pi S}} e^{-\frac{m^2+m'^2}{2S} - i(m-m')\varphi} e^{-\frac{\sin^2\vartheta}{2}\left(|\alpha_m|^2+|\alpha_{m'}|^2-2\bar{\alpha}_{m'}\alpha_m\right)}.\end{aligned}$$

Observe that the distribution of the spin state **is not** affected by the fact that this photons are not detected by us (nothing learnt, implies the same noise as the original CSS)

$$P(m) = \mathcal{A}(m,m) \approx \frac{1}{\sqrt{\pi S}} e^{-\frac{m^2}{2\frac{S}{2}}}, \qquad m \sim \mathcal{N}\left(0, \frac{S}{2}\right). \tag{2.8}$$

Photon distribution. The probability of detecting n photons is given by:

$$\begin{aligned}P(n) &= \mathrm{Tr}\left\{\mathrm{Tr}_{at}\left\{\hat{\rho}_{\text{measurable}}\right\}\left|n\right\rangle\left\langle n\right|\right\} \\ &= \sum_m \mathcal{A}(m,m) e^{-|\alpha_m\cos\vartheta|^2} \frac{1}{n!}\left(|\alpha_m|^2\cos^2\vartheta\right)^n \\ &= \sum_m P(m) \frac{e^{-\eta\langle n\rangle_m}\left(\eta\left\langle n\right\rangle_m\right)^n}{n!}.\end{aligned}$$

which is simply the conditional probability of finding the atoms in a particular state m and measuring the associated Poisson distribution for the state that corresponds, $|\alpha_m|^2 = \left\langle n\right\rangle_m$, scaled with a parameter η for the detection efficiency.

2.2.1 *Internal State After Measurement*

Let us say we measure n_d photons at the photon counter. The atomic component of the system is then described by $\hat{\rho}_{\text{f,atoms}} \propto \left\langle n_d\right| \hat{\rho}_{\text{measurable}} \left| n_d\right\rangle$ with

$$\begin{aligned}\hat{\rho}_{\text{f,atoms}} &\propto \left\langle n_d\right| \hat{\rho}_{\text{measurable}} \left| n_d\right\rangle \\ &= \sum_{m,m'} \mathcal{A}_{m,m'} e^{-\cos^2\vartheta\frac{|\alpha_m|^2+\left|\alpha_{m'}\right|^2}{2}} \frac{\left(\alpha_m\bar{\alpha}_{m'}\cos^2\vartheta\right)^{n_d}}{n_d!} \left|m\right\rangle\left\langle m'\right| \\ &= \sum_{m,m'} \mathcal{A}_{m,m'} e^{-\eta\frac{|\alpha_m|^2+\left|\alpha_{m'}\right|^2}{2}} \frac{\left(\alpha_m\bar{\alpha}_{m'}\eta\right)^{n_d}}{n_d!} \left|m\right\rangle\left\langle m'\right|.\end{aligned}$$

We can now focus on the diagonal terms, which give us the spin distribution conditioned to the detected photon number. Moreover, for large mean photon numbers. we can approximate the resulting Poisson's factor with a normal distribution $\mathcal{N}\left(\eta\left\langle n\right\rangle_m, \eta\left\langle n\right\rangle_m\right)$

$$P(m|n_d) = \mathcal{A}(m,m) e^{-\eta\langle n\rangle_m} \frac{\left(\left\langle n\right\rangle_m\eta\right)^{n_d}}{n_d!} \approx e^{-\frac{m^2}{2\frac{S}{2}}} e^{-\frac{\left(n_d-\eta\langle n\rangle_m\right)^2}{2\eta\langle n\rangle_m}}. \tag{2.9}$$

Note that our coupling[4] is such that $m\Omega \ll \gamma$. We define the n_0 as the expected number of photons to be detected after several realisations, i.e. $n_0 = \left(\frac{\kappa_t}{4\gamma}\right)^2 \frac{\eta}{\gamma^2} \frac{|\gamma_p|^2}{1+\left(\frac{\delta}{\gamma}\right)^2}$. Then, one can linearise the cavity profile,

[4] For our experiment $\hat{\Omega} = 2\pi \times 16.2(3)$ kHz, $\gamma = 2\pi \times 22.9(3)$ MHz, while m is "bounded" by QPN with $\frac{\sqrt{N}}{2} \lesssim 160$ for all experiments presented, or $\Omega\frac{\sqrt{N}}{2} \lesssim 2\pi \times 2.6$ MHz

as will be seen in equation 7.4:

$$\eta|\alpha_m|^2 = n_0(1-\beta\Omega m),$$
$$\beta = \frac{1}{1+(\delta/\gamma)^2}\frac{2\delta}{\gamma^2}.$$

If we write $\bar{m}$ the inferred spin from the measured n_d, and approximate the variance of the distribution by taking $n_d \approx n_0$ in the denominator of the second exponential of equation (2.9), we obtain:

$$P(m|\bar{m}) \propto e^{-\frac{m^2}{2\frac{S}{2}}} \exp\left(-\frac{(\bar{m}-m)^2}{2\frac{1}{n_0\beta^2\Omega^2}}\right),$$

and the conditional distribution

$$m|\bar{m} \sim \mathcal{N}\left(\frac{\bar{m}\frac{S}{2}}{\frac{S}{2}+\frac{1}{n_0\beta^2\Omega^2}}, \frac{\frac{S}{2}\frac{1}{n_0\beta^2\Omega^2}}{\frac{S}{2}+\frac{1}{n_0\beta^2\Omega^2}}\right) \tag{2.10}$$
$$\sim \mathcal{N}\left(\frac{\bar{m}}{1+\frac{4}{n_0\Omega^2\beta^2 N\mathcal{C}}}, \frac{\frac{S}{2}}{1+\frac{Nn_0\beta^2\Omega^2}{4}}\right). \tag{2.11}$$

Here, the metrological gain is brought by the denominator of the variance[5]:

$$\xi^2 = \frac{4\mathrm{Var}\,(m)}{N\mathcal{C}^2} = \left(1+\frac{Nn_0\beta^2\Omega^2}{4}\right)^{-1}\mathcal{C}^{-2}. \tag{2.12}$$

[5] Note that the initial spin distribution brings the term S before the light interaction, thus $S = \frac{N}{2}$ without the contrast term.

2.3 Technical Limitations for Our Experiment

The use of SSS is limited by the mechanism used to generate them, the states' lifetime and particular limits from our cavity experiment. With respect to its generation, the light in the cavity induces a loss in contrast due to the back-action of the scattered photons, which collapses atoms[61] and due to the dephasing induced by the inhomogeneous lightshift[65]. Also, the scattering processes can lead to spin flips (Raman scattering). Secondly, for values of $\langle S_z\rangle = 0$, the antisqueezed component of the state contributes to the noise of the squeezed component due to the curvature of the Bloch sphere[61, 66] leading to a loss of contrast. Finally, once the SSS is created, the atom losses in the magnetic trap lead to a degradation of the spin state. In the next subsections, we detail these phenomena.

2.3.1 *Contrast Loss*

Every time a photon is scattered into free space, the scattering atom loses its coherence with the rest of the ensemble. If the number of photons scattered by atoms is given by n_s, the contrast loss due to scattering is $\mathcal{C}_{sc} = e^{-n_s}$. The number of photons scattered is proportional to the number of photons in the cavity and the cooperativity C. We can relate the number of photons inside the cavity to the number of photons detected via the decay rate due to losses, *i.e.*, κ_t and

the detection efficiency η. It can be shown that $n_s = n_0 \frac{4\gamma C}{\eta\kappa_t}\left(\frac{\omega_{at}}{\Gamma_{at}}\right)^2$, leading to

$$\mathcal{C}_{sc} = e^{-\frac{n_0}{\gamma_1}}, \qquad \gamma_1 = \frac{\eta\kappa_t}{4\gamma C}\left(\frac{\Gamma_{at}}{\omega_{at}}\right)^2 \approx 1.05\times 10^5. \tag{2.13}$$

On the other hand, the antisqueezed component of the state wraps around the sphere, leading to a further reduction of the of the spin length. Introducting the shearing strength [6][53, 61, 67], $Q = \frac{Nn_0}{2\eta}\left(\frac{\Omega}{\gamma}\right)^2$, the reduction of contrast due to this back-action can be approximated by $\mathcal{C}_{BA} = e^{-\frac{Q^2}{2N}}$ [61], or in terms of the average photon number detected:

$$\mathcal{C}_{BA} = e^{-\left(\frac{n_0}{\gamma_2}\right)^2}, \qquad \gamma_2 = 2\eta\sqrt{\frac{2}{N}}\left(\frac{\gamma}{\Omega}\right)^2. \tag{2.14}$$

[6] This parameter quantifies the shearing effect described in 2.1.1 with $Q \propto \chi$ and can be defined as $Q \equiv N\chi\tau$.

2.3.2 *Effects on Noise due to Antisqueezing*

Besides the loss of contrast, another effect of the antisqueezed component due to the curvature of the Bloch sphere is the addition of noise in the radial direction. Consider, for example, figure 2.4 where a squeezed state, regarded from the z-axis with antisqueezed quadrature S_y wraps around the arc, adding noise in the S_x quadrature. Let $(\Delta S_z)^2 = \frac{S}{2}\xi_S^2$ and $(\Delta S_y)^2 = \frac{S}{2}\xi_A^2$ be the squeezed and antisqueezed components of the spin state[7]. Braverman et al. [68] showed that within the Holstein-Primakoff approximation[48, 69, 70], the variance of the radial component can be written as

$$(\Delta S_A)_r^2 \approx \frac{1}{8}\left(\xi_A^2 - \xi_A^{-2}\right)^2. \tag{2.15}$$

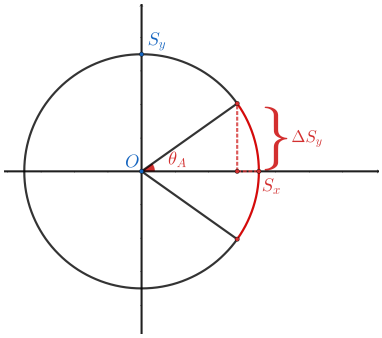

Figure 2.4: Radial component of the antisqueezed component. Say that the extend of the antisqueezed component is measured to be $\Delta S_y = \Delta S_{\theta=90^\circ} = S\sin\theta_A$. The associated radial component would be $(\Delta S_A)_r = S(1-\cos\theta_A)$

[7] Non-unitary squeezing could prevent the saturation of the Heisenberg limit such that $A = \xi_S\xi_A \geq 1$

Consider the perspective of the sphere with respect to the S_z axis as in figure 2.5. From this, it is clear that the contribution from the antisqueezing to the uncertainty on S_z is given by $(\Delta S_A)_z = (\Delta S_A)_r \sin\varphi$. Considering both components as independent contributions to the measurement noise, the variance for a measurement M_2 of the z component of spin would be given by

$$(\Delta S_z)^2\Big|_{M_2} = \frac{S}{2}\xi_S^2 + \frac{\sin^2\varphi}{8}\left(\xi_A^2 - \xi_A^{-2}\right)^2 + \gamma_{M_2}^2, \tag{2.16}$$

where we have included a term to consider the noise associated with any verification measurement, in our case, the photon shot noise associated with the cavity measurement.

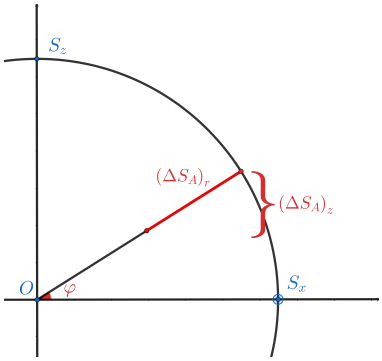

Figure 2.5: Contribution of antisqueezing to the noise on S_z.

2.3.3 *One-body Losses*

The atoms in the magnetic trap have a finite lifetime; in our case, by the vacuum's quality, the atom lifetime due to 1-body losses is $\gamma_{1b}^{-1} = 3.0(1)$ s. The effect of atom loss is two-fold: the decrease of the spin size and a random walk on the spin space. The former is the decrease of the size of the spin length according to $S(t) = S(0)e^{-\gamma_{1b}t}$. The latter comes from the fact that, since an atom goes

out of the trap, it does not contribute to the superposition anymore and has no label on whether it was in the up or down state. For an analytical treatment, we use the formalism introduced in 1.3.1 based on [49, 71]. Assume that both modes have the same one-body loss rate γ_{1b}. Using the jump operators $\sqrt{\gamma_{1b}}a, \sqrt{\gamma_{1b}}b$, the master equation in the interaction picture is:

$$\frac{d\rho}{dt} = \gamma_{1b}\left(a\rho a^\dagger - \frac{1}{2}\{a^\dagger a, \rho\} + b\rho b^\dagger - \frac{1}{2}\{b^\dagger b, \rho\}\right).$$

Which leads to:

$$\frac{d}{dt}\langle S_i\rangle = -\gamma_{1b}\langle S_i\rangle, \qquad \frac{d}{dt}\langle N\rangle = -\gamma_{1b}\langle N\rangle.$$

We can also calculate an extensive list of higher moments, and some calculations, for illustration, can be found in 12.2. In particular, notice that:

$$\frac{d}{dt}\langle S_i\rangle^2 = 2\langle S_i\rangle\frac{d}{dt}\langle S_i\rangle = -2\gamma_{1b}\langle S_i\rangle^2,$$
$$\frac{d}{dt}\left\langle S_z^2\right\rangle = -2\gamma_{1b}\left\langle S_z^2\right\rangle + \frac{\gamma_{1b}}{4}\langle N\rangle.$$

Combining the two equations, we end up with the system

$$\frac{d}{dt}\langle N\rangle = -\gamma_{1b}\langle N\rangle,$$
$$\frac{d}{dt}\Delta S_z^2 = -2\gamma_{1b}\Delta S_z^2 + \gamma_{1b}\frac{\langle N\rangle}{4}.$$

with the solution given by

$$\Delta S_z^2(t) = \Delta S_z^2(0)\, e^{-2\gamma_{1b}t} + \frac{\langle N\rangle}{4}\left(1 - e^{-\gamma t}\right). \tag{2.17}$$

The first term accounts for the reduction of the spin length, while the second term accounts for the uncorrelated losses from each spin state. Written in terms of the number squeezing, $\xi_N^2 = \frac{4\Delta S_z^2}{\langle N\rangle}$:

$$\left(\xi_N^2(t) - 1\right) = \left(\xi_N^2(0) - 1\right)e^{-\gamma_{1b}t}. \tag{2.18}$$

2.3.4 *Overall Squeezing*

Consider a preparation where the spin state is squeezed through the cavity measurement and left to evolve during a time t before a confirmation measurement is applied. Since no additional rotations are induced on the state, we expect no phase accumulation and, thus, no particular evolution of the state. This allows us to ignore the antisqueezed component's effect due to the radial component's projection. However, we cannot neglect the modification of the contrast. In this case, the expected squeezing from this state is:

$$\xi_{\text{th}}^2(t) = \left(\left(1 + \frac{n_0 N_0 \beta^2 \Omega^2}{4}\right)^{-1} e^{-2\gamma_{1b}t} + \left(1 - e^{-\gamma_{1b}t}\right)\right)\mathcal{C}^{-2}, \tag{2.19}$$

$$\mathcal{C} = e^{-\frac{n_0}{\gamma_1} - \left(\frac{n_0}{\gamma_2}\right)^2}. \tag{2.20}$$

Notice that we replaced $S = 2N_0$. The atom number is the initial one since this term comes from the prior given by the initial CSS that the measurement has now updated.

Part II

Experimental Apparatus

3
TACC and TACC-2 platforms

Our experiment is based on the trapped-atom clock on a chip (TACC) described in [72, 73], with the particularity that now it incorporates two fibre Fabry-Pérot cavities [74]. The magnetic hyperfine states $|\downarrow\rangle \equiv |F=1, m_F=-1\rangle$ and $|\uparrow\rangle \equiv |F=2, m_F=1\rangle$ are chosen as clock states [39, 72]. The cavities mounted on the chip allow for probing of the hyperfine states. Used as a clock with standard Ramsey interrogation and coherent spin states (CSSs), the experiment currently reaches fractional frequency stability of $6.5 \times 10^{-13}\,\mathrm{s}^{-1/2}$. Due to background collisions, it has a phase-coherence time of 20 s, longer than the trap lifetime.

Complete descriptions of the experimental apparatus can be found in the thesis by Ott [75] and Huang [67]. This chapter presents the electronic and mechanical components of the experiment relevant to this manuscript. For further details, we refer to the previously mentioned theses. All the descriptions of the optical system are relegated to chapter 4.

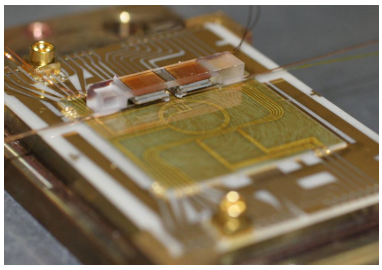

Figure 3.1: Photograph of the chip assembly before glueing to the vacuum

3.1 Atom Chip

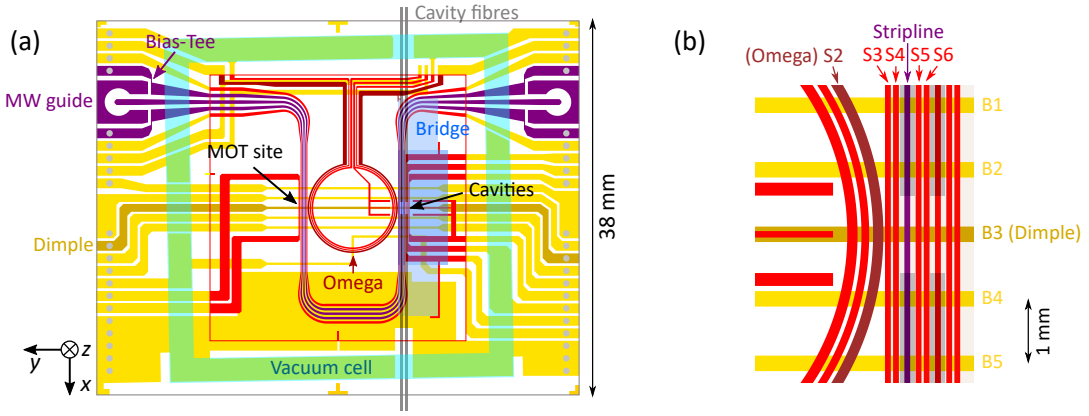

Figure 3.2: a) Atom Chip Layout. Red Patterns are on the science chip on top of the yellow patterns of the base chip. The walls of the glass vacuum cell are shown in green. b) Zoom-in of the cavity region.

The atom chip is a bonded two-layered structure: the case chip and the science chip. Both layers are on an aluminium nitride substrate with electroplated gold conductors patterned by photolithography. The complete layout of the chip is shown in figure 3.2 a). We

recognise two major regions, separated by 9 mm: The mirror-MOT site on the left and the cavity region on the right. Both sites are crossed by a U-shaped coplanar waveguide (CPW) used to deliver the microwave (MW) photons for interrogation. The central conductor of the CPW also produces DC currents for magnetic confinement at both sites; this conductor is referred to as the *Stripline* in the text. A wire parallel to the Stripline (S6) delivers the RF photons. In the centre of the chip, we also find a circular *Omega* wire, used for trapping at the MOT site and transport between the MOT site and the cavity region. A transversal wire runs through the middle of the base chip, referred to as the *Dimple*. The Dimple generates magnetic traps on both sides, while the parallel cables help shift the centre of such trap for alignment with the cavity centre.

To assist in creating magnetic fields for confinement, the chip is backed by a copper block containing a U-shape conductor (macro-U) used during the initial MOT. On the same structure, there is a bent copper wire (macro-I) used for the compressed MOT and the first magnetic trap (see section 3.5). Both conductors are parallel to the Stripline at the MOT site. Also, external coils surrounding the vacuum cell provide magnetic bias fields in the x, y, and z directions. Finally, a water cooling system stabilises the temperature of the chip to reduce thermal effect due to heating by the currents on the chip.

Mirror-MOT site. The mirror-MOT site captures atoms at the beginning of an experimental cycle. A 2D-MOT in the lower part of the set-up (see section 3.2) provides a cooled atomic beam that can be captured with the macro-U and appropriate bias fields. As mentioned above, this site is crossed by both the Stripline and the Omega wires. We can choose whether to create the magnetic traps using either of both wires, depending on whether we want to interrogate the atoms directly on site or if we're going to transport them to the cavity region. The macro-I wire is aligned parallel to the Stripline at the MOT site to assist in generating the magnetic field for the compressed MOT.

Cavity Region. After capture and initial cooling, the atoms are then transported to the cavity region using the Omega wire (see section 3.5). In the cavity region, two fibre cavities are mounted and glued to the chip side by side[1]. Figure 3.3 shows a photograph of the cavities hanging about 400 μm from the surface of the chip.

Both cavities share a common piezo stack on each side. Each side can be controlled independently from the other side, but both cavities move together. The shared bridge then allows to lock of the length of both cavities with the locking light exclusively at the high finesse cavity, while the science cavity only has the interrogating light. This mode of lock was tested and reported by Huang [67]. A low-frequency relative drift between cavities was found and some schemes to correct this were proposed, but we opted to keep the single-cavity lock system described in chapter 5 since the theoretical

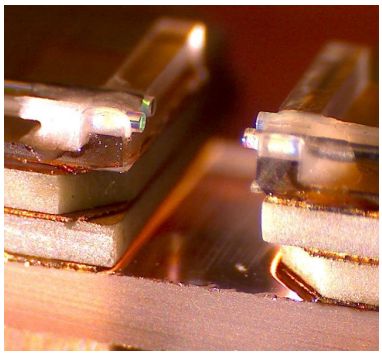

Figure 3.3: Photograph of the fibre cavities glued to the chip.

[1] The cavity closer to the Omega wire is the low finesse cavity, at $2.69 \pm 0.1 \times 10^3$, referred in the text as science cavity, while the second cavity is at a finesse of $38.2 \pm 2.1 \times 10^3$ at 780 nm

limit on this locking system could be made smaller than PSN which seemed to be enough at the time[2].

A close-up of the cavity region wires can be found in figure 3.2 b). A light shading on top of the Stripline shows the science cavity. Cables S2, S3 and S4 are used for the parallel transport of the cloud into the cavity (see section 3.5). The Dimple wire generates confinement in the x direction, while the wires B2 and B4 align the atomic cloud with the centre of the cavity.

[2] It should be mentioned that the second cavity could also allow to study interrogation at another finesse regime; we left this for future studies. No further studies were conducted using the second cavity for this thesis.

Current Sources and Connections. Silver wires are bonded to the chip conductors using silver-filled conductive glue and soldered to copper. Those silver wires connect to a printed circuit adaptor board. The connection goes to standard ribbon wires on the other side of the adaptor.

All DC currents passing through the chip are generated using SYRTE-made low-noise current sources designed by Reinhard [29]. They can deliver up to 3 A and have a relative rms noise (bandwidth from 20 Hz to 100 kHz) below 4×10^{-6}, with a long-term relative stability of about 10^{-5} . In addition, homemade switches were added to almost all current sources to invert the polarity. Currents used to generate bias fields B_y and B_x are also from such sources. Macro-U, Macro-I and a bias field B_y are produced using commercial Delta Elektronika sources[3]. All currents are controlled with a digital signal from a National Instrument card with a 16-bit resolution programmed using GoodTime, a software developed by Jakob Reichel.

[3] The B_y bias field is mainly generated using the low-noise sources. The Delta source is used exclusively during the first mirror-MOT and the evaporative cooling.

3.2 Vacuum System

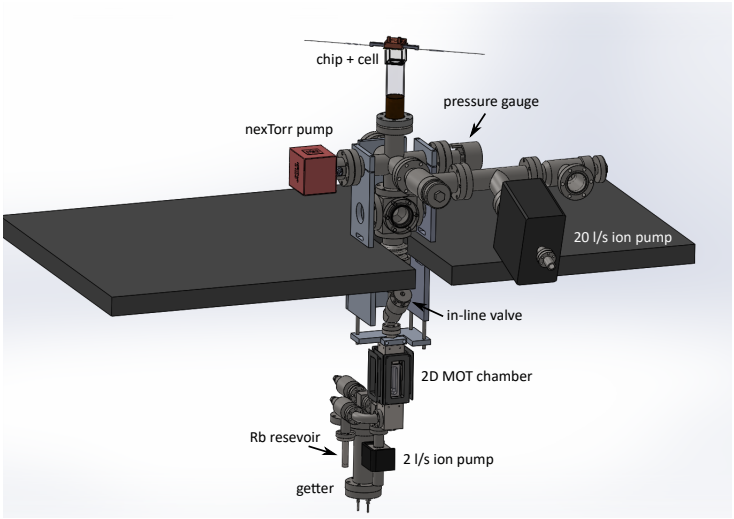

Figure 3.4: Schematics of the vacuum system. The main chamber with the atom chip is at the top. An in-line valve connects The main chamber to the 2D MOT chamber, allowing for differential pumping between chambers. The main chamber is pumped by a 100 l/s getter pumper, a 5 l/s ion pump (Nextorr D 100-5) and a 20 l/s ion pump (Varian StarCell). The 2D-MOT chamber is pumped by a 50 l/s getter (SEAS GP-50) and a 2 l/s ion pump (Varian). The Rb reservoir can be found at the bottom.

There are two vacuum chambers, depicted in figure 3.4: the main vacuum cell and the 2D MOT chamber. The main cell, seen in figure 3.5, is a cubic AR-coated Pyrex cell with one of its walls replaced by the chip. A hole at the bottom allows the atomic beam to enter from

the 2D MOT chamber. Two 1 mm^2 trenches were cut at the sides to let through the fibres and later sealed with UHV-glue (EPO-TEK 353ND).

The 2D MOT is there to shorten the loading time of the MOT[76]. The differential pumping provides a pre-cooled atomic flux while keeping a good vacuum in the main chamber. The 2D MOT chamber is made of titanium alloy with indium-sealed windows. A Rubidium reservoir made from pure metal is in a glass cell inside the enclosing. The cell is broken after the vacuum is placed, releasing the Rb.

The pressure achieved after bake-out and once the chip was in place was around 3.0×10^{-10} mbar, but degraded gradually until reaching 1.5×10^{-9} mbar at the pressure gauge. A similar pressure was achieved in the previous experiment (TACC). However, at the time, the atom lifetime in the trap was much higher, almost 6 s. This led us to hypothesize that outgassing occurs at the main chamber, degrading the atom lifetime to around 2 or 3 s, depending on the chip's temperature.

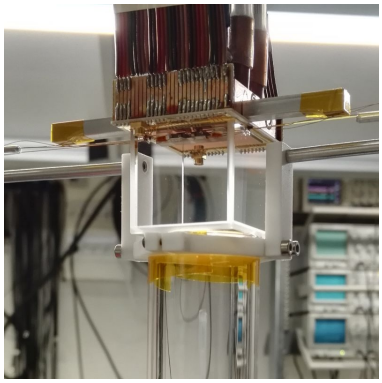

Figure 3.5: Photograph of the main vacuum chamber and the chip glued to it. Electrical connections and the water cooling tubes can be seen on the side. Fibre supports are coming out from the sides of the chamber. The copper block holding the macro-I and macro-U is visible at the top.

3.3 Imaging

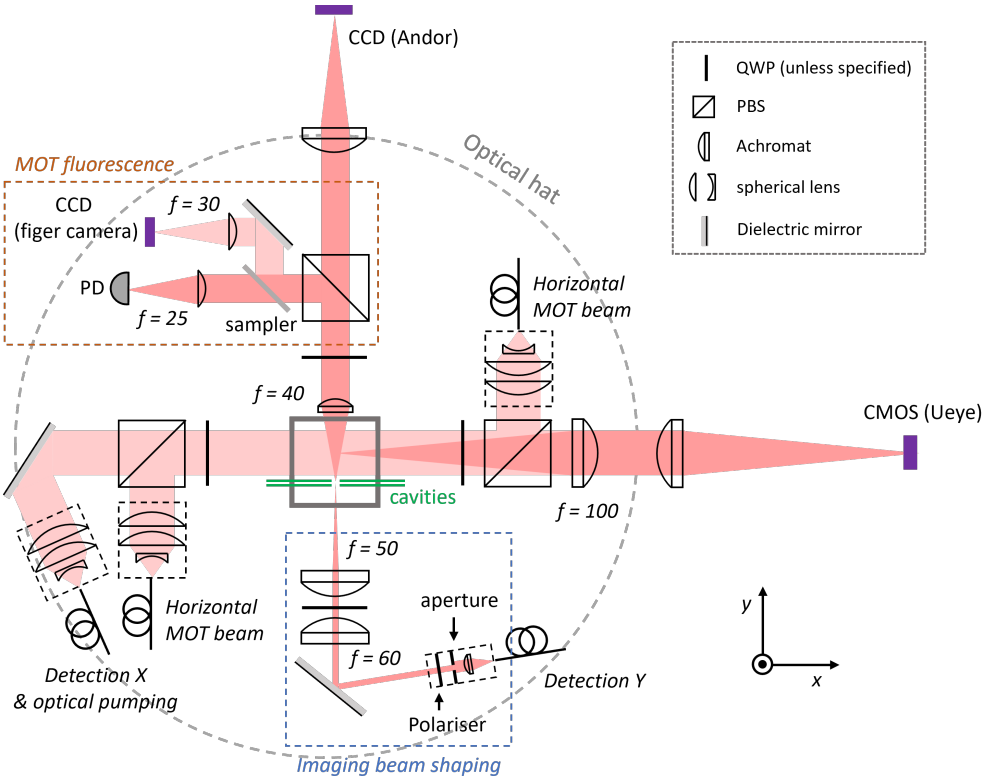

Figure 3.6: Schematics of the optics on the optical hat seen from the top. Three cameras allow for imaging at different sites of the chip. A CCD finger camera captures the MOT fluorescence at the mirror-MOT site. A CMOS camera (Ueye) is aligned along the x direction; this camera is used to image the mirror-MOT site. A CCD camera (Andor) aligned along the y axis images the atoms through the cavity.

Around the main chamber, optical components are aligned on top of an aluminium plate. Non-magnetic fibre connectors feed the light necessary for detection, optical pumping, and the horizontal beams for the mirror-MOT. The main components can be seen in figure 3.6. Three imaging systems are present: a finger camera to capture the MOT's fluorescence, a CMOS camera to see the mirror-MOT site, and

a CCD camera to image through the cavity.

MOT Camera and Fluorescence. A finger camera to capture the fluorescence of the MOT has been placed inside the magnetic shielding. This camera facilitates the adjustment of the relative intensity of the beams at the MOT site. A photodiode was also introduced to capture the fluorescence signal during the MOT phase, allowing for feedback control of the MOT loading time.

CMOS (uEye) camera. As mentioned, we can use a CMOS camera to image the MOT site. The detection along x is only used for the characterisation of the traps at the MOT site, hence the use of an economical industrial camera [4]. This camera has a CMOS sensor with 3 MP resolution, a frame rate of 120 fps and a QE of 32% at 780 nm.

[4] IDS uEye UI-3070CP

CCD (Andor) camera. Imaging along the y direction requires low-noise detection for clock operation in the cavity. We use a CCD camera[5] with a QE of 95% operating at $-60°$C to reduce noise and dark current. To account for the presence of the cavity, the beam was shaped to avoid scattering with the fibres or the bridge holding them. An aperture is imaged to the atom's plane in the cavity, then imaged again into the CCD camera. Because of this solution, it is not possible to use this camera to image the MOT site. Additionally, the imagining lens has a limited NA and is partially obstructed by the chip. To avoid fringes due to diffraction, we require a minimum of 1 ms TOF to image a thermal cloud.

[5] Andor iKon M934-BRDD

Absorption Imaging and ARP. At the end of an experimental cycle, atoms are released from their trap. Imaging of the atoms in $|F = 2\rangle$ is performed by a detection beam resonant on the $F = 2 \rightarrow F' = 3$ cycling transition. A second image (bright frame) is subsequently performed once the atoms are removed. The two frames are then combined to obtain the absorption image of the atomic cloud. The absorption is governed by the atomic density integrated over the imaging axis. We work at a strong saturation regime to achieve a high signal-to-noise ratio (SNR) while also reducing PSN[77].

A typical way to detect the two clock states is to perform a double detection scheme, where a repumper is added during the bright frame. The two states get spatially separated due to the free fall, allowing for the second image to work as a bright frame for the state $|F = 2\rangle$. However, this scheme is susceptible to power and frequency fluctuations between frames, and the detectivity of both states is different due to the repumping process.

An alternative method for detection, developed in TACC-1, consists of transferring the atoms in $|\downarrow\rangle$ into $|2, 0\rangle$ via an adiabatic rapid passage (ARP)[78]. We sweep the transition frequency by varying the bottom field in an integrated Blackman profile while ramping up the MW delivered by the CPW. We achieve 100% transfer efficiency

limited by detection noise. The atoms in $|2,0\rangle$ begin to fall while the atoms in $|\uparrow\rangle$ remain trapped. Once the two clouds are sufficiently separated, the atoms in $|\uparrow\rangle$ are released and imaged after 2.5 ms TOF. Technical noise is common for both clouds, and the difference in detection efficiency between $|2,0\rangle$ and $|\uparrow\rangle$ is negligible. The main drawback of this detection scheme is the perturbation of the cloud's temperature due to the applied MW, particularly in the x direction. This could be avoided by a frequency sweeping of the MW instead.

Detection Noise. The main contribution to noise comes from PSN, which, at saturation, is about 2.2 atoms per pixel[67, 78]. More precisely, we can decompose the noise on a measurement of $P_\uparrow = N_\uparrow/(N_\uparrow + N_\downarrow)$ into:

$$\sigma^2_{P_\uparrow} = \frac{\sigma^2_{\text{det}}}{2N^2} + \frac{1}{4N} + \sigma^2_{\text{tech}}. \tag{3.1}$$

The first term in equation 3.1 is the contribution of the photoelectron's shot noise noise to detection; the second term is the quantum projection noise (QPN) contribution and, finally, σ^2_{tech} is the technical noise, which is bounded below 10^{-6} and can be neglected for this analysis[6]. Here, we have introduced the detection noise σ_{det} as the standard deviation in the atom number of each state, assuming it to be the same for both spin states. At the time, Huang [67] measured σ_{det} to be around 48.2. For our typical atom number, between 1×10^3 and 2×10^4 atoms, the contribution due to detection is between 23% and 46% in variance[7].

[6] Already, the QPN term is on the order of 10^{-5} for the number of atoms we typically use.

[7] The shape of the imaged cloud is elliptical. This means that we have a contribution of noise from 22% of the pixel, which does not contain atoms. We have recently added an elliptical digital mask around the atom cloud to reduce the impact of noise by detection, but this has not been thoughtfully characterised since we have focused mostly on the detection of the state via the cavity.

Another contribution to the detection noise is the optical fringes due to vibrations or frequency fluctuation between the two frames. We apply postprocessing of the images to remove optical fringes by reconstructing a bright frame that perfectly matches the image frame in the region, excluding the atoms from a basis of previously taken images. The efficiency of the fringe recomposition has been analysed in [78].

3.4 Microwave and RF photons

The clock transition between the clock states $|1,-1\rangle$ and $|2,1\rangle$ requires two photons in σ^+ polarisation, via an off-resonant intermediate state $|2,0\rangle$. This is accomplished with one photon close to the hyperfine splitting, about 6.834 GHz, and the other close to the Zeeman splitting in RF, generated by a homemade frequency chain and a direct digital synthesiser (DDS), respectively. The detuning to the intermediate state is about 500 kHz, which sets an upper bound for the Rabi frequency between the clock states.

3.4.1 Microwave Chain

Our MW source is a homemade low-noise synthesiser, referenced to the stable 100 MHz reference available at SYRTE. The architecture

is presented in figure 3.7. The principle is to phase-lock a dielectric resonator oscillator (DRO) running at 6.434 GHz to the 100 MHz SYRTE reference, buffered by a phase-locked quartz oscillator[8][79]. A stable 6.4 GHz signal is generated by the quartz reference through a non-linear process to lock the DRO, with a tunable offset of about 34 MHz provided by a DDS.

A second signal at 400 MHz is derived from the quartz oscillator. A voltage variable attenuator[9] is used to control the power of this signal. The stabilized signal from the DRO then drives the output mixer, combined with the 400 MHz, to control the output power. This approach allows for easy control of the output power of the MW chain but introduces a phase imbalance that depends on power. Such imbalance is fairly replicable and can thus be simply accounted for during the configuration of the interrogation pulses (see section 3.6.4).

[8] NEL frequency controls Inc., a 100 MHz oscillator internally multiplied from a 10 MHz crystal

[9] Minicircuits TFAS-1SM+

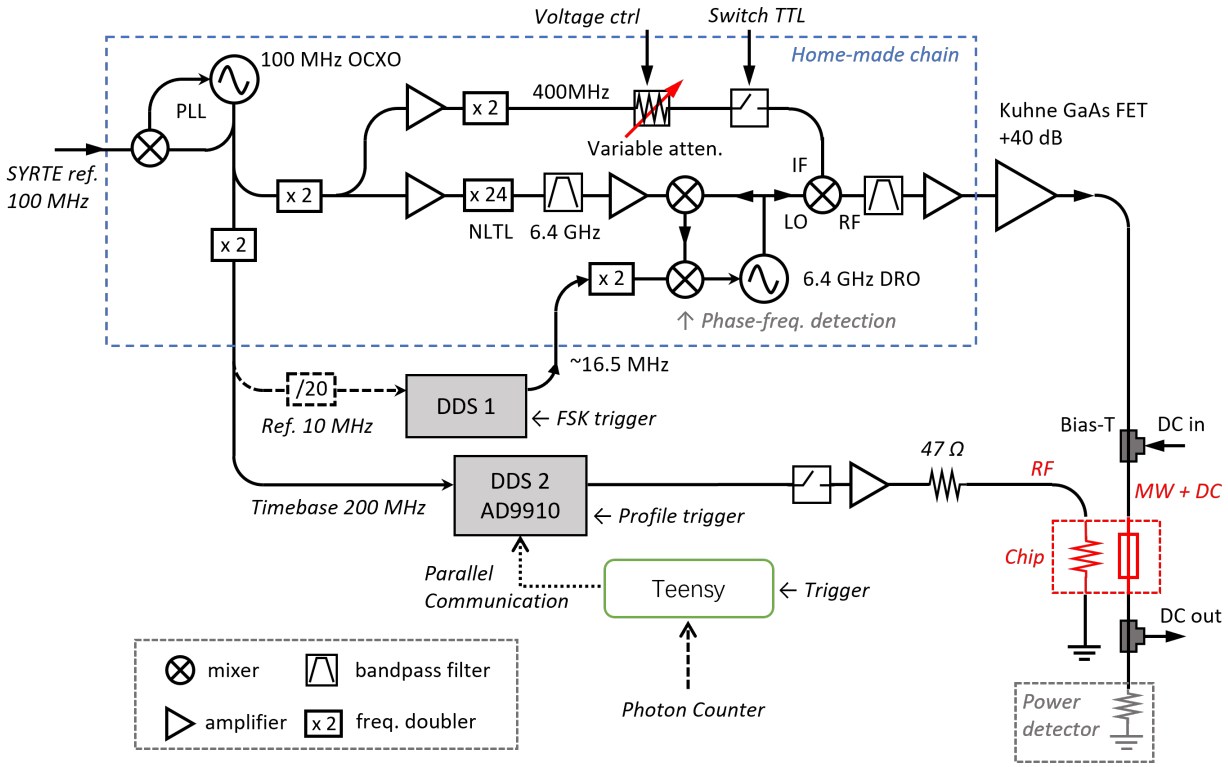

Figure 3.7: Schematics of the generation of MW and RF photons. Only a simplified scheme of the MW chain is shown. The DDS1 is temporally a Rigol DG1032Z, with frequency-shift keying (FSK) functionality. DDS2 is based on AD9910, allowing faster switching between 8 stored output profiles. OCXO: oven-controlled crystal oscillator; NLTL: non-linear transmission line.

3.4.2 *The RF Photons*

The RF photons are generated directly by a DDS AD9910 that has been referenced to a 10 MHz signal down-converted from the stabilised 100 MHz reference. Both the phase and frequency control of the applied pulses is done directly through the RF photons. The AD9910 can store 8 output profiles (independent frequency, phase and amplitude) that can be selected in real time. The switching is phase continuous and stabilises within 1.5 μs (at 1.7 MHz output). A homemade controller allows to toggle between these profiles with a

single trigger. It adds a delay of 100 ns, negligible for our application.

Teensy Microprocessor. Previously, all control of the phase, frequency and amplitude of the RF pulses was programmed at the beginning of the experimental cycles and change "on the way" with the aforementioned trigger. However, our recent work requires us to change the phase of some of the applied pulses during the sequence itself. This is to account for the phase imprinted by the probe photons into the atomic state (see section 8.1). These phase changes cannot be instructed directly from the usual communication using GoodTime due to the time constraints of the sequence and cannot be programmed ahead of time since they depend on the results of the cavity measurement. Our solution is to use a Teensy 4.0 microprocessor. The Teensy is a USB-based microcontroller that can perform similar tasks to an Arduino but with a faster CPU performance[80].

When a phase correction is needed, we send a copy of the raw signal from the photon counter monitoring the cavity transmission (see section 4.3) to one of the Teensy ports. Using the FreqCount library[81], the Teensy microprocessor is capable of counting the number of pulses received accurately under 15 MHz rates[10]. An external trigger synchronised with the experimental sequence indicates when to begin and finish the photon counting. The corresponding phase correction ϑ is calculated by the Teensy in real-time according to independent calibrations (see 6.1.2). The adequate instructions are codified into some of the Teensy pins for parallel communication with the AD9910. The instructions are finally sent when a second trigger from Goodtime instructs the Teensy, overwriting the current profile in use during the sequence.

[10] In practice, our probe pulses always have photon rates under 3 MHz.

3.5 Trapping and Transport

We now describe the steps that are followed for a typical experimental cycle to capture, transport and evaporate the atoms until getting them to the clock trap. The optical benches required to produce the corresponding light beams are presented in chapter 4.

2D MOT. Atoms are initially cooled down in the 2D MOT chamber under the main chamber. A part of the beam used for cooling the 2D MOT is split to generate a push beam that sends an atom into the main chamber. No detailed characterisation of the atomic beam has been done or required.

Mirror 3D MOT. While the 2D MOT is illuminated, the 3D MOT loads. A coarse alignment of the 45-MOT beams and horizontal beams is done with the help of the finger camera; a picture of the loading can be seen in figure 3.8. A more precise alignment can be done with a precise measurement of the atom number using absorption imaging. The loading of the mirror-MOT with the assistance of the 2D MOT can reach atom numbers on the order of 10^7 in 300 ms.

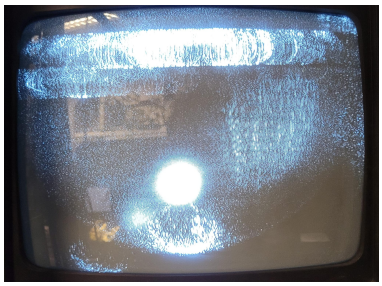

Figure 3.8: Photograph of mirror-MOT loading through the finger camera.

Compressed MOT and Molasses. After capture, the atoms are transferred to a compressed MOT to get them closer to the atom chip. The macro-I assists the Omega wire in creating the main confinement of the trap. A molasses stage follows the compressed MOT. The cloud can reach about 5 μK in molasses. An image of the molasses obtained with the uEye camera is shown in figure 3.9. At the end of the molasses, a short optical pumping is performed at the $1-1$ and $2-2$ transitions.

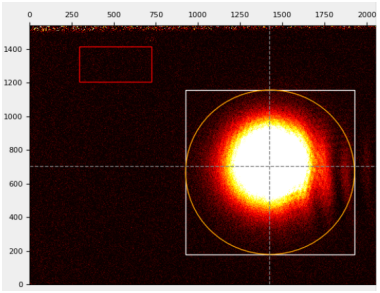

Figure 3.9: Absorption imaging of the molasses with the uEye camera.

First Magnetic Trap and Rotation. After optical pumping, the atoms are captured at the first magnetic trap. The Dimple forms the trap for the confinement in the x direction, while the Omega wire and the macro-I form the main confinement. Once loaded, the atoms are immediately transported into the transport trap. The trap for rotation is a quadrupole trap formed by the Omega wire and the combined B_x and B_y fields. By varying the strength of both bias field components, the minimum of the quadrupole trap displaces, rotating the atoms along the Omega wire. The temperature of the atoms when loading the rotation trap is around 50 μK.

Parallel Parking. Once the atom cloud has reached the cavity region, we begin the parallel transfer. We refer to figure 3.2 for context. The first transport turns off the Omega wire while ramping up the current through the S3 wire. At the same time, perpendicular wires B2 and B4 form a U-type trap, keeping the trap a quadrupole trap. The second transport from S3 to S4 ramps up the Dimple to form a Dimple trap, and this shape is maintained as the S4 is turned off and the Stripline is ramped up.

Evaporation Trap. Once below the Stripline, the trap is tightened to begin evaporative cooling. At this point, the atoms are in the state $|1,-1\rangle$. An RF signal, blue-detuned from the $|1,-1\rangle \rightarrow |1,0\rangle$ transition, expells the atoms at higher energies. By sweeping the RF frequency closer to the Zeeman splitting while allowing sufficient time for the atoms left in the trap to reach thermal equilibrium, the atoms are cooled down. The RF radiation used for this process is provided by an SRS DS345, using its internal exponential frequency sweep and analogue amplitude modulation to control the power.

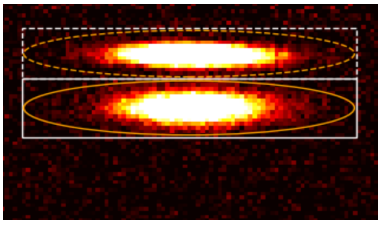
Figure 3.10: Atom clouds imaged through the cavity after being released from the clock trap. Upper cloud corresponds to state $|\uparrow\rangle$ and the lower cloud are atoms in state $|\downarrow\rangle$

Interrogation Trap. After evaporation, the trap is decompressed to form a dimple trap that will serve as the main clock trap. The decompression is performed in two stages described in [67] to reduce residual oscillations. To correct for the centre's positions inside the cavity, the Dimple is assisted by the B2 wire to move the cloud in the x direction. Also, an additional bias B_z is used to displace the cloud in the y direction. Figure 3.10 shows an image of a state prepared at the equator of the Bloch sphere, obtained with the Andor camera. As explained in section 3.3, an ARP is used to transfer all the atoms in $|\downarrow\rangle$ into $|2,0\rangle$ and begin falling. After 2.5 ms, the current through

the stripline is cut, releasing the atoms in state $|\uparrow\rangle$. After 2.5 ms, both clouds are imaged as shown where the upper cloud are the atoms in $|\uparrow\rangle$, while the atoms in the lower cloud are those in $|\downarrow\rangle$.

3.6 Interrogation Pulses

Here, we briefly describe the basic tuning procedures of the interrogation pulse. We first introduce our criteria for the pulse length based on the field inhomogeneity. Then, once the magic bias field is found[11], one can adjust the frequency and amplitude of the MW and RF pulses such that the light shift induced by them compensates for each other.

[11] The determination of magic field was described by Huang [67]. This is when the energy splitting is immune to magnetic field fluctuations to the first order. The basic idea is to use Rabi spectroscopy with approximately well-calibrated pulses to recover the quadratic relationship between the bias field B_x and the transition frequency.

3.6.1 *Field Inhomogeneity*

The excitation fields delivered by the chip wires are intrinsically inhomogeneous as the field strength decays away from the conductor. We have observed evidence of the field inhomogeneity [67]. However, this inhomogeneity can be largely ignored as long as the minimal pulse length is kept a multiple of the oscillation period[12] of the trap in the z direction, *i.e.*, 8.85 ms.

To make sure the field inhomogeneity can be neglected, we adjust the length of our pulses such that $T_\pi = 120$ ms so that our $\pi/2$ pulses are at least 6 times the oscillation of the trap. We also need shorter π pulses to perform echo protocols. To account for the reduction of the pulse length, we make use of composite pulses (see section 3.6.3.

[12] Additionaly, we have found evidence of the state $|2,2\rangle$ being populated for shorter pulses, probably due to the extended spectral width of a shorter pulse.

3.6.2 *Two-photon Lightshift*

Due to the imperfect polarisations of the RF pulses, there is a residual light shift induced on the clock transition. Interestingly, the sign of the light shift depends on which side of the chip wire we deliver the RF signal. We choose the one that gives an opposite sign to the one induced by the MW photons. We chose the MW and RF amplitudes such that the light shift induced by both pulses cancels each other. Note that there is a linear relationship between the induced shift for each field and its amplitude. Thus, this configuration does not eliminate the linear dependence on amplitude fluctuations of each field.

We can determine the light shift of the RF or the MW separately by comparing a normal Ramsey sequence with one keeping either the RF or the MW field on during the Ramsey time, respectively. As the $\pi/2$ pulses are in common, the difference between the central fringes directly indicates the frequency shift during the Ramsey time. By running three Ramsey spectroscopy sequences (normal, RF on during t_d, and MW on during t_d), one can determine the associated shift. To choose the amplitude to be used, we recall from the adiabatic elimination method [82] that the Rabi frequency associated with a two-photon transition is proportional to the amplitude of both fields. Also, the light shift induced by each field follows a quadratic

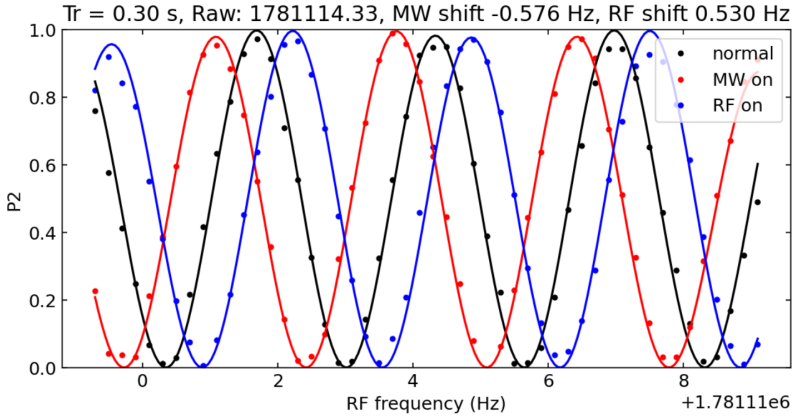

Figure 3.11: Typical data of two-photon light shift compensation, by letting RF or MW field on during t_d.

relationship to its amplitude. Using this, we can adjust the amplitude of both fields such that the lightshift is compensated. Typical data for this sequence is shown in figure 3.11.

3.6.3 *Composite Measurements and Composite Pulses*

To partially compensate for the light shift induced by the probe beam on the atoms, we make use of an echo sequence: A first probe imprints a phase on the atoms in the trap. A π pulse is sent to the atoms, effectively reversing the shift imprinted by the probe. Finally, a second probe also imprints a phase that partially compensates for the one induced by the first one. For this scheme to make sense, the time between the two probe pulses is required to be as short as possible. However, we are confronted with the limitations on the duration of pulses due to field inhomogeneities that we discussed in section 3.6.1.

To solve this issue, we used composite pulses. Composite pulses are combinations of pulses that are able to compensate for imperfections in both amplitude and frequency. These combinations of pulses have wide applications in the field of nuclear magnetic resonance (NMR) [83]. There is a large selection of composite pulses[84]; we settled for the SCROFOLOUS pulses, *i.e.*, $\hat{\pi}(\vartheta - \pi/3) \cdot \hat{\pi}(\vartheta + \pi/3) \cdot \hat{\pi}(\vartheta - \pi/3)$. Other pulses we tried are U(3), U(5) and Waltz. We choose to have the constituent π pulses to have a fixed length of 8.85 ms to allow for averaging along the oscillation period. We kept the shortest pulses (three *pi* pulses instead of five) that have the better population transfer. The effect on contrast of the atomic state is shown in figure 3.12.

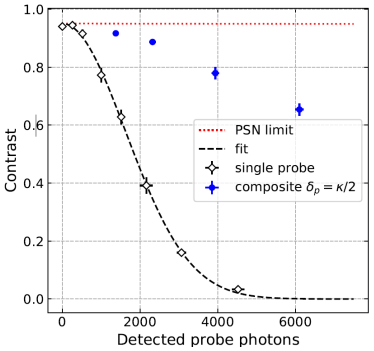

Figure 3.12: The contrast of Rabi oscillations after a composite measurement as a function of detected probe photons. The probe detuning is adjusted at half transmissions. The data after a single probe (open black circles) is compared with the composite measurement with a SCROFOLOUS pulse in between probes (solid blue circles).

To calibrate our composite pulses, we first adjust for single 8.85 ms π pulses. We proceed as we described in section 3.6.2: Three different Ramsey interrogations are used to measure the lightshift induced by the probe. Then, we use this measurement to obtain new values for the amplitude of the MW and RF such that the RF light shift cancels the light shift induced by the MW. We perform Rabi interrogation after a cavity measurement with a single probe

to obtain a contrast measurement as a function of the number of photons in the probe. We do the same protocol after a composite measurement. Some typical data of this comparison is shown in figure 3.12. We can note a clear improvement with respect to the use of a single probe. The contrast loss with composite measurement follows the description presented in section 2.3.1.

3.6.4 *Phase Calibrations*

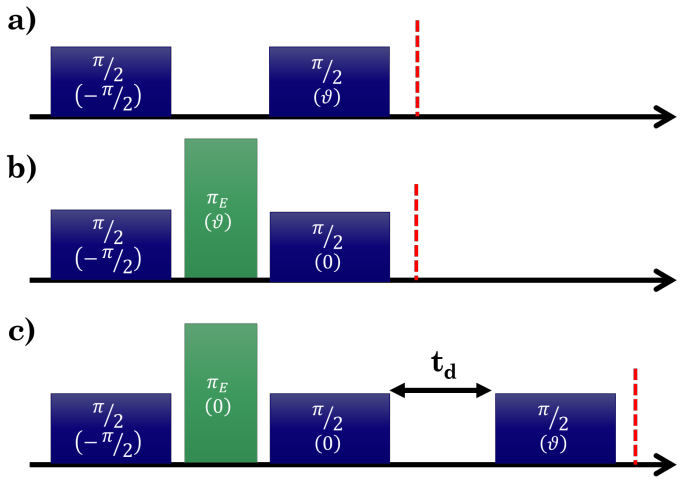

Figure 3.13: Phase calibration protocols. The blue and green rectangles show MW+RF pulses on the clock transition. The blue rectangles are $\pi/2$ pulses with a duration of 60 ms. The green rectangles are composite SCROFOLOUS pulses. The global phase of the pulses is shown in parentheses. The red line marks the absorption imagined. a) We leave the phase of the first $\pi/2$ pulse fixed and leave enough time to apply a composite measurement. Then, we scan the phase ϑ of a second $\pi/2$ pulse. This allows us to find the phase accumulated at the second pulse due to imperfect calibration of the RF frequency. b) We leave the phase of the first $\pi/2$ pulse fixed. We introduce a SCROFOLOUS pulse identical to the one we use in composite measurement with enough time before and after to send the corresponding probe pulses. Then, we send a $\pi/2$ pulse with a fixed phase. Then, we scan the global phase ϑ of the composite π pulse. This allows us to find the phase correction of the composite pulse due to the phase imbalance introduced by the power control (see section 3.4.1). c) We repeat the same process, this time leaving the phase of the SCROFOLOUS pulse fixed. We leave a time t_d pass after the second $\pi/2$ pulse. We then send a $\pi/2$ pulse after a delay corresponding to the sequence we would like to run (see section 8 for an example) and scan its phase ϑ. This allows us to find the phase due to imperfect calibration of the RF frequency

When measuring the phase accumulated by the atomic state, it is important to account for the contributions coming from an imperfect calibration. As mentioned in section 3.4.1, the power control used at the MW chain introduces a phase imbalance that has to be compensated for. Also, imperfect calibration of the RF frequency can introduce a phase that has to be accounted for when orienting the spin state in the Bloch sphere. We use a complete protocol of adjustment like the one described in section 3.6.2 at least once a month. However, we routinely verify the duration and frequency of our pulses. We show in figure 3.13 the routine protocols we use to calibrate the adequate phase offsets.

All phases are referred to the first $\pi/2$ pulse, creating the CSS in the equator of the Bloch sphere. We take as convention its phase to be $-\pi/2$. To account for the phase due to imperfect calibration of the RF frequency, we send a $\pi/2$ pulse after a delay of 46 ms and scan its phase. We measure the final population difference with absorption imaging and use the corresponding Ramsey fringe to find the phase shift. This protocol is shown in figure 3.13 a). Once the phase of the second $\pi/2$ pulse is accounted for, we introduce an SCROFOLOUS pulse in between both $\pi/2$ pulse and scan its phase. This measures the phase imbalance introduced by the MW power control that we discussed in section 3.4.1. This protocol is shown in figure 3.13 b). Finally, we leave the phase of the three pulses fixed and we add third long $\pi/2$ pulse after a time t_d corresponding to the desired accumulation (see chapter 8).

3.6.5 *Clock Stability*

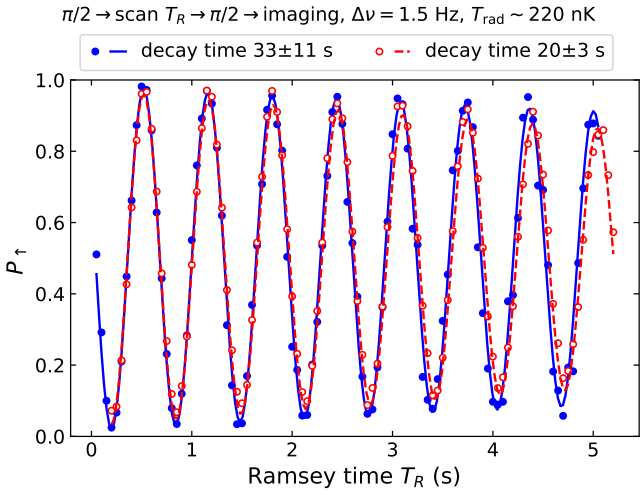

Figure 3.14: Ramsey fringes in the time domain, showing the coherence of the system. The LO is strongly detuned (1.5 Hz) to see fringes as a function of T_R. Two sets of data are for two slightly different traps: $\{\omega_x, \omega_y, \omega_z\} \approx 2\pi \times \{5, 97, 84\}$ Hz at $\Delta B = -40$ mG (solid blue) and $\{\omega_x, \omega_y, \omega_z\} \approx 2\pi \times \{3, 110, 99\}$ Hz, $\Delta B = -30$ mG (open red). The latter is the one used for clock measurements in figure 3.15. The difference in ΔB is the main cause of the different decay times. Retrieved from [67]

One of the main objectives of TACC-2 is not to use squeezed states as a simple proof of principle. TACC-2 was designed and built to function in metrologically relevant regimes even without the use of entangled states. Huang [67] characterised both the phase coherence time to be on the order of 20 s as shown in figure 3.14 for our trap geometry. The coherence time is much longer than the trap lifetime of the atoms, which allows us to see the effects to be described in chapter 6.

Preliminary characterisation of the clock stability at $T_R = 1$ s shows a stability figure of $6.5 \times 10^{-13}\tau^{-1/2}$ as shown in figure 3.15. This is comparable with the previous TACC iteration, which reached a fractional frequency stability of $5.8 \times 10{-}13$ at 1 s [73]. Other compact clocks using thermal vapour and buffer gas or laser-cooled atoms have reached short-term stabilities in the same order of magnitude [14–18] on their record performances.

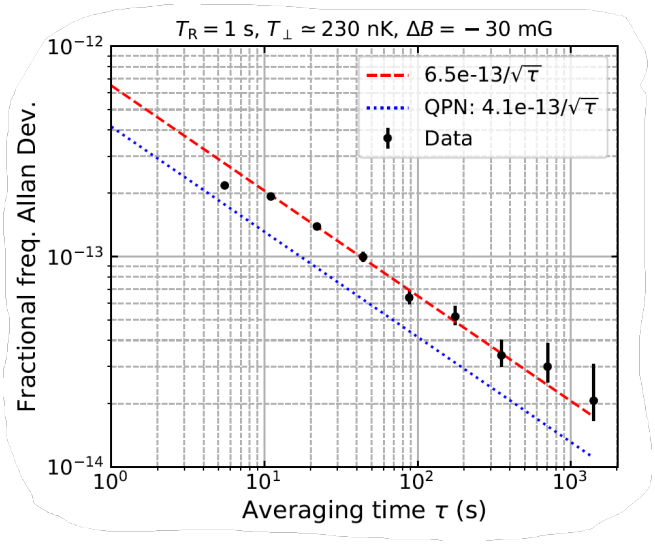

Figure 3.15: One of the best clock stability results at $T_R = 1$ s. The initial atom number is 2.7×10^4. The QPN alone contributes nearly half of the noise. Retrieved from [67].

4
Optical Modules: Main, 2DMOT and Probe Bench

The experiment TACC-2 has three separate fuctional optical tables

1. **Main Bench:** For generating cooling beams for the mirror MOT on the chip and detection beams.

2. **2D MOT bench:** For generating cooling beams used at the 2D MOT and the push beam to send the atoms to the chip.

3. **Probe laser bench:** For generating beams used for cavity lock and atom interrogation.

Most of the main and 2D MOT benches remain as described by Huang [67], so we include them together in this chapter as a reference for completeness and to point out recent changes. We treat the probe bench and frequency lock in this chapter but leave the cavity lock and probing analysis for the next chapter.

Both modules discussed in this chapter make use of SYRTE-designed extended-cavity diode lasers (ECDL) as the ones described in [85], with laser diodes from Thorlabs. Most current sources for our lasers and locking electronics are also made at SYRTE, with the exception of the current sources for the cooling laser at the 2D MOT bench and the slave laser of the main bench, both being also commercially available at Thorlabs.

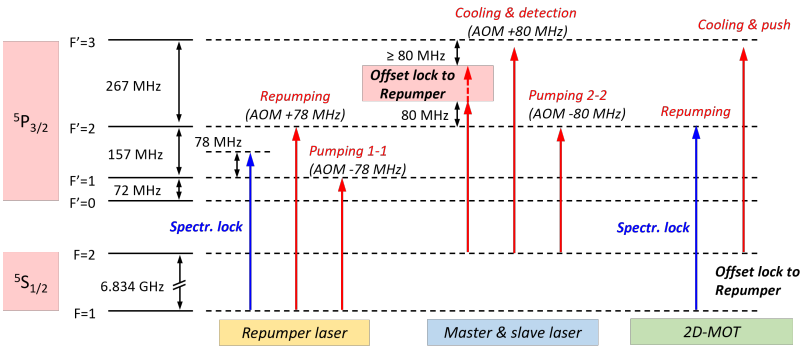

Figure 4.1: Diagram of laser frequency generation, including that of the 2D-MOT. AOM: acousto-optic modulator. Retrieved from Huang [67].

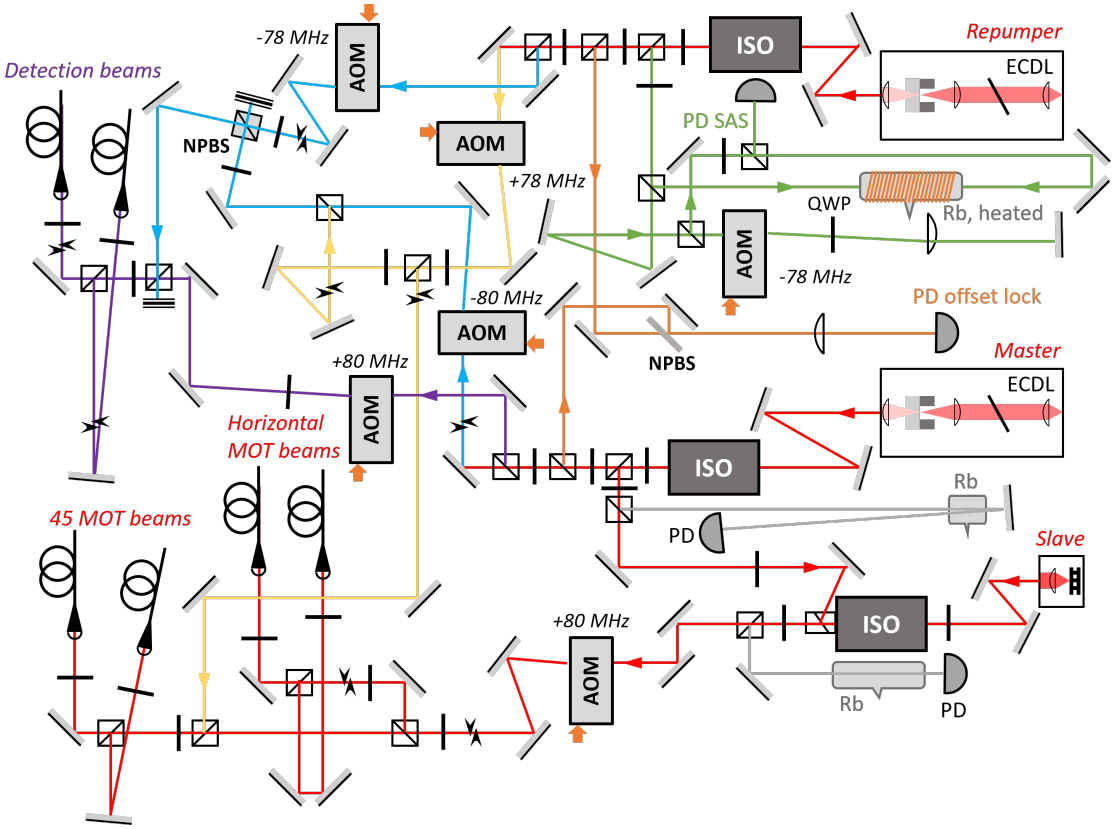

Figure 4.2: Main module. Functionalities colour laser beams: green: SAS; orange: offset lock; yellow: repumping; blue: optical pumping; purple: imaging; grey: monitoring; red: cooling; and others. ISO: optical isolator; HWP: half waveplate; QWP: quarter waveplate; (N)PBS: (non-)polarising beam splitter; PD: photodiode. Retrieved from Huang [67].

4.1 Main Bench, Mirror MOT and Detection.

The laser module for the Mirror MOT remains as described by Lacroûte [86] for TACC and Huang [67] for TACC-2, except for the repumper laser that has been replaced due to the degradation of the previous diode. All lasers are frequency referenced to the repumper laser[1]. Repumper is locked between the ^{87}Rb transitions $5^2S_{1/2}(F=1) \rightarrow 5^2P_{3/2}(F'=1)$and $5^2S_{1/2}(F=1) \rightarrow 5^2P_{3/2}(F'=2)$ by saturated absorption spectroscopy (SAS) [87] to access both transitions for pumping and repumping, respectively. The master laser (master in the sense of the slave diode) is locked to the repumper by beat-note, hence more widely tunable, to generate either the cooling beams near the $5^2S_{1/2}(F=2) \rightarrow 5^2P_{3/2}(F'=3)$ transition or the pumping beam at the $5^2S_{1/2}(F=2) \rightarrow 5^2P_{3/2}(F'=2)$ transition.

[1] Most of the main bench was used for TACC-2 as it was done for TACC-1, with the exception of an additional split of the repumper beam to allow for it to be used when imaging through the cavity.

4.2 2D MOT Bench

Most of the laser module for the 2D MOT bench remains in a similar configuration as described by Huang [67]. The repumper is an Extended-Cavity Laser Diode (ECLD) from SYRTE, locked via SAS to the ^{87}Rb transition $5^2S_{1/2}(F=1) \rightarrow 5^2P_{3/2}(F'=2)$ by directly modulating the diode current at 70 kHz.

The cooling laser originally was a self-seeded tapered amplifier (TA) laser (TAL-780-1000). After the first squeezing measurements reported in part III, this cooling laser went out of service and was

replaced with another homemade ECLD[2]. The power measured at the output seemed to be less than the one obtained by the TA laser. However, in the latter, an important amount of optical power was lost to fluorescence, and mode quality was suboptimal due to the large divergence of the beam and difficulty in aligning its lenses. Besides, fabrication and alignment of the ECLD is simpler, so we opted for this solution. The cooling laser is frequency locked to the repumper via beat note with a $\sim$ 6.6 GHz offset to be close to the ^{87}Rb transition $5^2S_{1/2}(F = 2) \rightarrow 5^2P_{3/2}(F' = 3)$. For simplicity, the push beam is split from the cooling beam, incapable of independent frequency tuning. Due to the long distance ($\sim$ 0.7 m) between the 2D-MOT and the atom chip, the MOT loading is very sensitive to the push beam power and alignment, exhibiting a clear optimum. The characteristics of the atomic beam out of the 2D-MOT have not been rigorously examined. But loading the mirror-MOT works reasonably well so that 10^7 atoms can be loaded in the MOT within 0.5 s, sufficient for our experiments.

[2] Thorlabs LD785-SH300

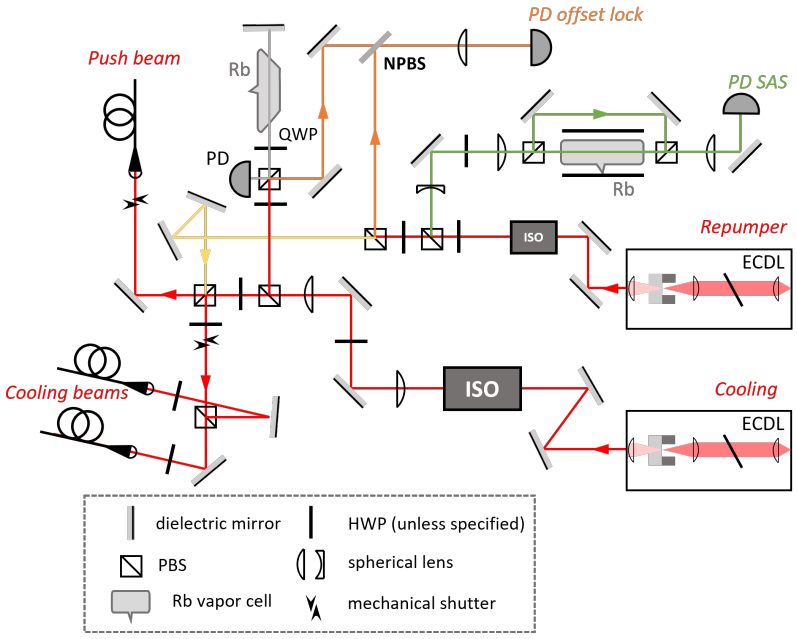

Figure 4.3: 2D-MOT module. Laser beams are colour-labelled based on function: green: SAS; orange: offset lock; yellow: repumping; blue: optical pumping; purple: imaging; grey: monitoring; red: cooling and the rest. ISO: optical isolator; HWP: half waveplate; QWP: quarter waveplate; (N)PBS: (non-)polarising beam splitter; PD: photodiode. Updated from Huang [67].

Atom Number Fluctuations. During the last 3 years, we have observed an increase in the fluctuations in atom number both in the shot-to-shot number and the average fluctuation, particularly being affected by the room's temperature. A first solution for this was to isolate the 2D MOT bench with a cover; this improved the situation marginally. We found a defect on the breadboard[3] on what the bench is mounted, which made it susceptible to mechanical deformations. However, after replacing the TA laser with the ECLD, the fluctuations decreased; this may be because the TA laser required a large heat dissipator attached to the side that deformed the surface of the breadboard

[3] We are working on a replacement for this bench with a more rigid breadboard. We also plan to modify the geometry of the paths, particularly before the fibre coupling, to reduce power fluctuations.

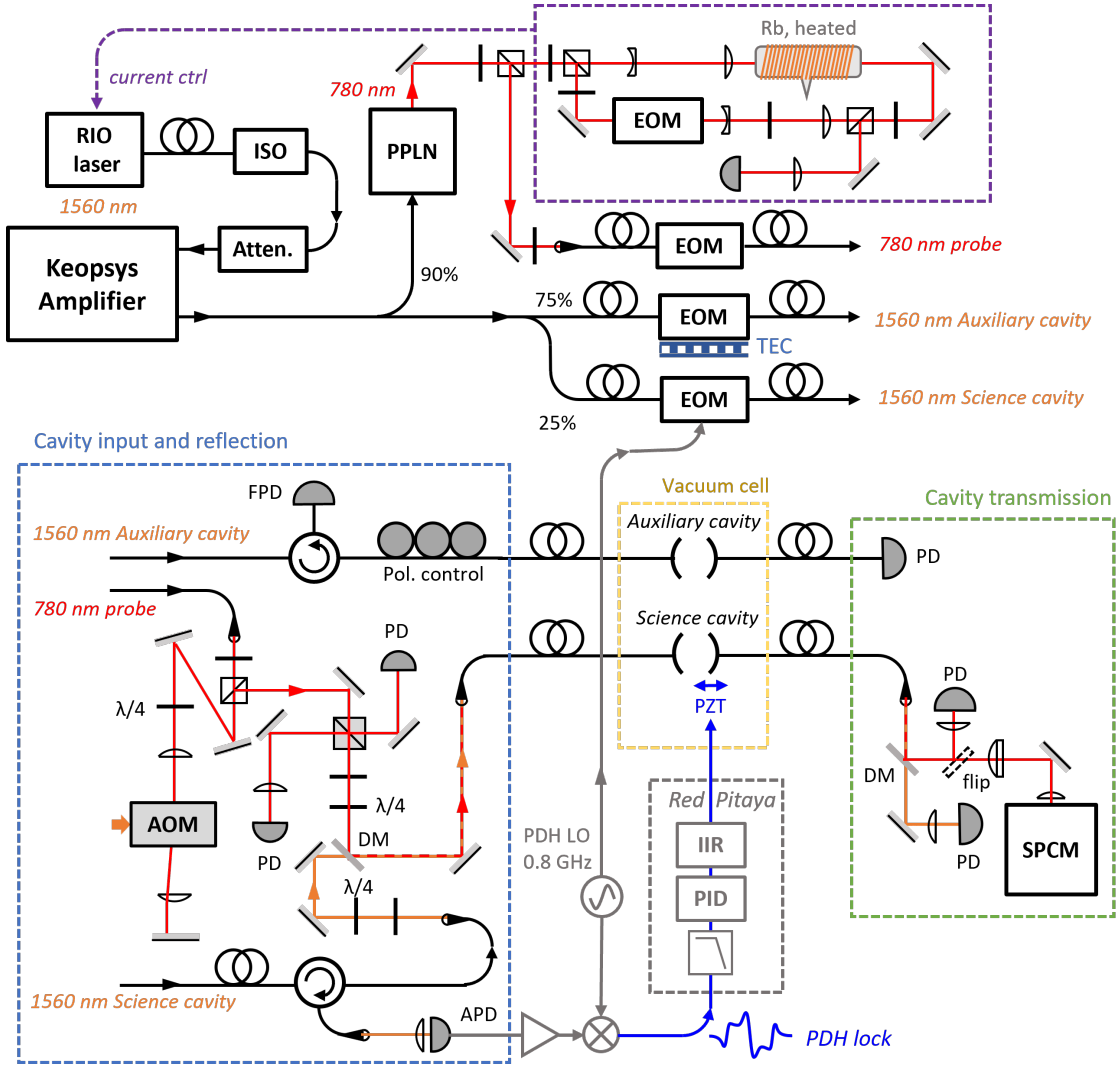

Figure 4.4: Schematics of the complete laser setup for cavity probing and stabilisation. Here, we show direct Pound-Drever-Hall (PDH) locking of the science cavity. Electronics are shown in grey. APD: avalanche photodiode; DM: dichroic mirror; FPD: fast photodiode; PZT: piezoelectric stack; SPCM: single photon counting module; TEC: thermoelectric cooler. Retrieved from Huang [67].

4.3 Probe Laser Bench

No relevant changes in the generation of the probing light have been realized since Huang [67] reported it. A diagram of the bench is shown in figure 4.4. Our setup uses a fibre-based 1560 nm laser from RIO[4] amplified with a fibre amplifier[5]. A fibre-injected periodically-poled lithium niobate (PPLN) crystal generates a frequency-doubled 780 nm laser into free space. One part is sent to reference the source laser via a modulation transfer spectroscopy (MTS) on Rb vapour[88, 89] with correction signal onto the current control of the laser diode. We lock the laser to the cycling transition of ^{85}Rb ($F = 3 \rightarrow F' = 4$). The 780 nm light is coupled again to another fibre. Both the 780 nm and 1560 are passed through EOM[6] to generate sidebands (see next paragraph). Both are sent into free space; the 780 nm light goes through a double-pass AOM used as an optical switch before recombining in free space with the 1560 nm light to be coupled with the science-cavity fibre.

[4] PLANEX 1550 nm Laser Diode

[5] Keopsys CEFA-C-PB-HP

[6] EOSPACE PM-5V5-UV for the 1560 nm light and iXblue NIR-MPX800-LN-05 for the 780 nm.

Lock and frequency control. To implement QND measurements of S_z in the dispersive regime, the cavity resonance is detuned in between the ^{87}Rb transitions $5^2S_{1/2}(F = 1) \rightarrow 5^2P_{3/2}$ and $5^2S_{1/2}(F = 2) \rightarrow 5^2P_{3/2}$, a detuning so large that we can neglect hyperfine splittings of the excited state. For the science cavity, our target mode is about 800 MHz away from the laser at 1560 nm, while the 780 nm is about 2.5 GHz away from the ^{85}Rb reference. We apply a PDH modulation at 805 MHz to the 1560 nm light and lock the cavity to the blue sideband. This has the secondary effect of reducing the amount of locking light in the cavity to reduce its trapping effect. As the detuning determines the atom-cavity coupling for the two clock states, a precise and stable adjustment of the cavity frequency is required. The probe laser frequency should also be independently tunable to vary the detuning to the cavity mode. For this, an electro-optical modulator (EOM) is fed by a 2.4 GHz signal[7] to generate sidebands. We use the higher frequency one as a probe with the unwanted carrier and red sideband being sufficiently filtered by the cavity. Its power and frequency are easily tunable by both the Agilent generator and the AOM used as a switch. The general frequency scheme for the probing system is shown in figure 4.4. To control whether we perform an interrogation on the red or blue profile of our cavity, we use an Frequency-shift keying (FSK) scheme centred around the cavity resonance with a shift of ± 20 MHz depending on the desired profile[8].

[7] Agilent PSG Vector Signal Generator (E8267D)

[8] We use a 40 MHz step instead of a 45.8 MHz step due to the limitation for the frequency toggle of the FSK available at the device (Agilent VSG). However, this does not seem to be detrimental to the measurements (see $\beta\Omega$ values in section 5.3)

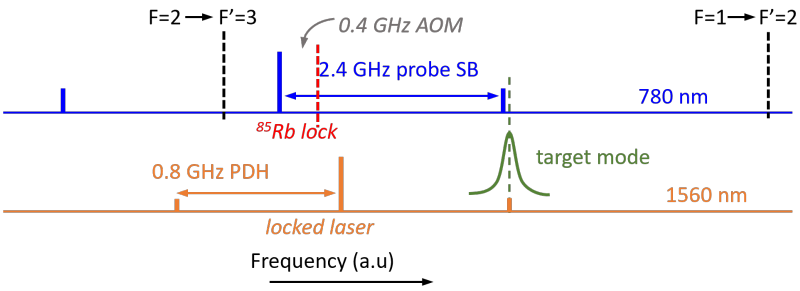

Figure 4.5: Frequency scheme for the cavity locking light and probe. Retrieved from Huang [67].

5
Cavity Probe

One of the key differences between TACC-2 and its predecessor is the use of fibre cavities.[67, 75]. The set-up includes a Low Finesse cavity (LF), also referred to as the Science cavity and a High Finesse (HF) cavity[1]. The difference in finesse could allow us to study the system in different atom-cavity coupling regimes while having two cavities could serve to lock the cavity length with one cavity while the other one is used for interrogation, as they are both glued to the same mechanical holder. This locking scheme has been discussed by Huang [67]. For the work on this thesis, we focus almost exclusively on the science cavity both for lock and interrogation. However, we do describe some of the common cavity parameters for both of them for reference. A more detailed description of both the fabrication and characterisation can be found in [74, 74, 90, 91].

[1] The high and low finesse are relative to the 780 nm light. Both have relatively high finesse for the 1560 nm light.

5.1 Laser and Cavity Lock

5.1.1 Experimental Realisation of the Fibre Cavities

Both the high and low finesse cavities are machined using a multi-shot technique to achieve a large radius of curvature [74, 90, 91]. The cavity length is approximately 1.2 mm, which is particularly long. Because of this, the mode size at the mirror could be particularly large with respect to some single-mode fibres. To account for this, a large-mode photonic crystal (PC) fibre (LMA-20) is at the input to improve the mode-matching to potentially 60%. The output fibre employs a multi-mode (MM) fibre to ensure maximum collection of the intra-cavity photons.

In TACC-2, atoms should be trapped magnetically, so the commensurate wavelength is not essential for a squeezed clock. We adopted this scheme for technical convenience and also for the possibility of exploring intra-cavity lattice experiments with optimum coupling. However, the mirror phase shift is only correctly engineered for the LF cavity. For the HF cavity, the 780 nm mode and the exact-double-wavelength 1560 nm mode are not resonant at the same time but with a detuning of 25 GHz of the 1560 nm mode.

Parameter	Units	Low Finesse (LF)	
Length L	μm	1215 ± 20	
$\mathrm{ROC}_{\mathrm{MM}}$	μm	1612	
$\mathrm{ROC}_{\mathrm{PC}}$	μm	1559	
$\mathrm{ROC}_{\mathrm{eff}}$	μm	1560	
z_R	μm	745	
ν_{FSR}	GHz	123 ± 2	
		780 nm	**1560 nm**
w_0	μm	13.6	19.2
w_{mirror}	μm	17.5	24.8
$\frac{\kappa}{2\pi} = \frac{\gamma}{\pi}$	MHz	45.8 ± 0.6	5.35 ± 0.08
$\mathcal{F}$	$\times 10^3$	2.69 ± 0.1	23.06 ± 0.8
$T(\delta = 0)$	%	25.8	10.8
$R(\delta = 0)$	%	10.4	40.8
$R(\delta \gg \kappa)$	%	42.1	65.0
$\frac{g_0}{2\pi}$	MHz	10.9	-
$C_0 = \frac{4g_0^2}{\kappa\Gamma}$		1.9	-
$\frac{\Omega_0}{2\pi} = \frac{4g_0^2}{\omega_{\mathrm{at}}}$	kHz	69.5	-
C_{eff}		0.42	-
$\frac{\Omega_{\mathrm{eff}}}{2\pi}$	kHz	17.1	-

Table 5.1: Cavity parameters recovered from [67] for both 780 and 1560 nm. $\mathrm{ROC}_{\mathrm{eff}}$ are deduced from the higher-order mode spectra [75]. $\frac{\kappa}{2\pi}$ is FWHM, while $\frac{\gamma}{2\pi}$ is HWHM. g_0, C_0 and $\Omega_0 = \frac{4g_0^2}{\omega_{\mathrm{at}}}$ use the D2 dipole matrix elements summed over all sublevels. The effective values, however, use the σ^+ transitions relevant in the experiment and assume a cloud at $T = 200$ nK in the trap with $\omega_z = 2\pi \times 110$ Hz. The effective values are calibrated in sequences described later in the text.

We notice that, due to mode-matching issues, the overall transmission is about one-fourth of full transmission at resonance with the 780 nm mode, as can be seen in figure 5.1. Considering a transmission function given by:

$$T(\delta) = \left(\frac{\kappa_t}{2\gamma}\right)^2 \frac{1}{1 + \left(\frac{\delta}{\gamma}\right)^2}, \tag{5.1}$$

we can deduce that $\kappa_t = 1.01587\gamma \approx \gamma$. This is the approximation we will use for the rest of the text. A second peak on the upper side of the cavity profile may be more relevant for our system. This is a higher-order mode about 100 MHz away from the fundamental mode. Previous simulation by Ott [75] showed this mode to be compatible with a 7-th order mode and it weakly couples with the atoms when placed in the cavity, as will be seen later.

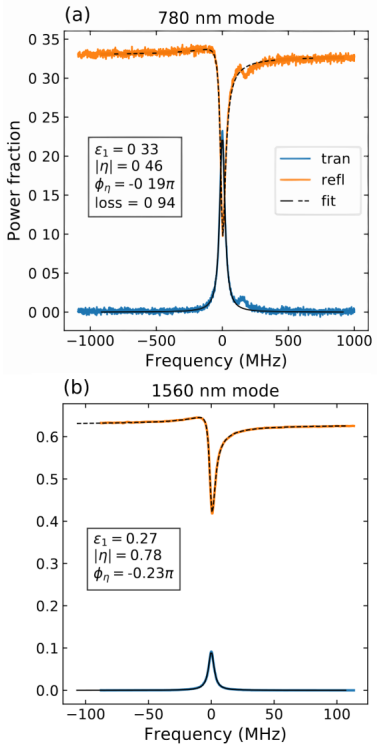

Figure 5.1: Transmission and reflection spectra of the (a) 780 nm mode and the (b) 1560 nm mode in the science cavity. A High-order mode close to the fundamental mode in 780 nm is visible in (a).

5.1.2 *Cavity Lock, Feedback and Feedfoward*

We use a Pound-Drever-Hall (PDH) scheme feeding the error signal to lock the cavity through a PI scheme [92, 93]. An 800 MHz modulation is applied to the 1560 nm light through an EOM to generate the PDH signal. This EOM is passively-stabilized to prevent temperature-dependant residual amplitude modulation (RAM)[2]. We lock to the blue sideband to reduce the leakage of the 1560 nm light, reducing lightshift and trapping effects. More precisely, the squeez-

[2] The RAM is limited to 2.5%; this is not the limiting factor of the lock.

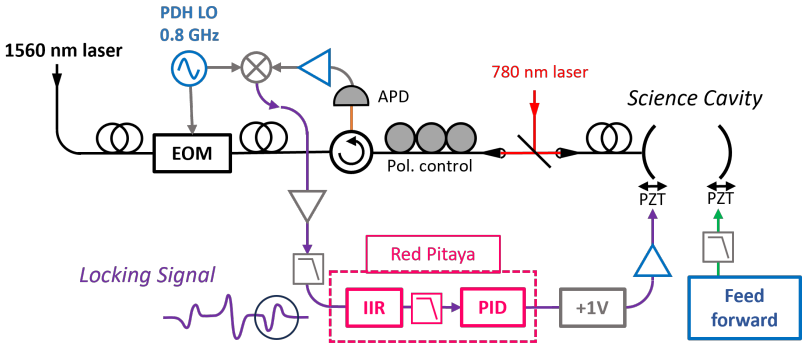

Figure 5.2: Locking cavity system. A PDH signal is produced with a 800 MHz modulation, reference to an external highly-stable 10 MHz reference. The signal is amplified, demodulated, and low-pass filtered before being sent to the Red Pitaya. The signal is passed through the IIR filter implemented from the PyRPL library before applying a second-order LP filter and being sent to the PID module. An external module shifts the locking signal by +1V (See paragraph on quantisation noise) and is finally amplified before being sent to the cavity piezo. Home-made elements are marked in grey, while ready-made devices are marked in light blue.

ing measurements were performed at 9 nW in-coupled power, keeping the lightshift on the order of a couple of tenths of mHz as reported by Huang [67]. On the other hand, more recent measurements for clock sequences ran at 20 nW in-coupled power, leading to about -500 mHz lightshift. This increase in power was due to technical difficulties with the cavity lock, which will be explained below.

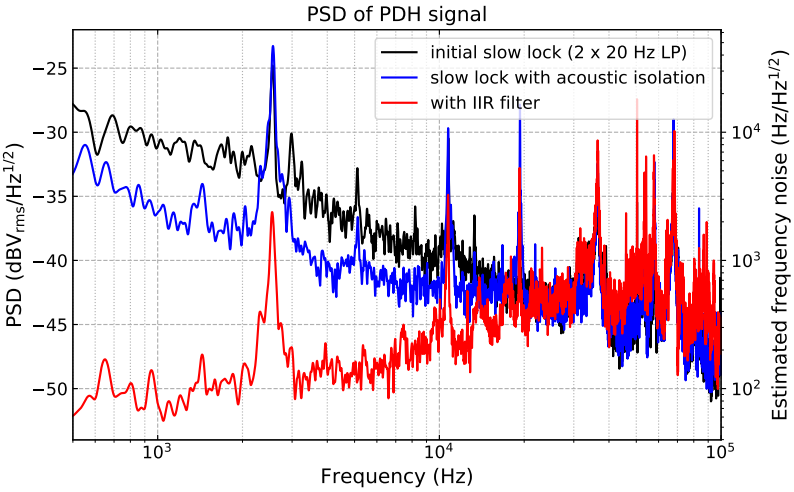

Figure 5.3: Power spectral density of cavity lock. Blue and black curves show slow lock before IIR implementation. Blue curve is taken after acoustic isolation with PVC curtains around the experiment. In red, we see the improvement of the lock up to the 20 kHz crossing. Retrieved from [67]

Mechanical Resonances. Mechanical resonances of the cavity can limit the locking bandwidth. In usual PID feedback loops, the error signal has to be filtered below the lowest resonance of the system[92]. Using a network analyser, our cavity has been characterized to possess resonances at 2.6 kHz, 8.8 kHz and 10 kHz, corresponding to flexure modes. This had the effect of limiting the lock bandwidth to about 100 Hz. A digital solution to avoid imposing such frequency cut-off is the use of Infinite Impulse Response (IIR) filters[93]. In practice, such filters can be best implemented digitally. For this, we make use of a Red Pitaya[3] device paired with the Python Red Pitaya LockBox (PyRPL) developed by Neuhaus et al. [94]. The library already contains a network analyzer module that allows the measurement of the transfer function of the cavity and calculates an IIR filter accordingly.

[3] This is a low-cost field programmable gate array by STEMlab with integrated microprocessor and 14-bit ADC as input and 14-bit DAC as output

After implementation, this solution extends the locking bandwidth to 20 kHz (see figure 5.3).

Thermal Drift and Feedforward. The DC currents used to generate the trap, mainly from the stripline, induce a strong thermal drift that perturbs the cavity length. During a typical experimental cycle, the cavity resonance can be shifted by up to 8.5 GHz, which is much larger than the range of capture of the lock. However, the thermal drift becomes reproducible for cycles of fixed length after some time.

We fixed the time the stripline is on to 2.2 s from the moment the atoms are placed in the clock trap, the moment it is turned off for imaging the atoms, and turn on again for the empty cavity measurements. Scanning the cavity length, we find the resonance and interpolate a spline over 5 consecutive cycles. Inverting this signal gives a feedforward signal that we send to an amplifier and then to the piezo that is not controlled by the locking signal. This signal reduces the thermal drift to about 100 MHz in the 1560 nm light, which can be easily followed by the PDH lock as long as the feedforward signal is smooth enough.

Quantisation Noise and RedPitaya. A drawback of using a Red Pitaya is the introduction of quantisation noise, which can limit the lock quality. The RedPitaya has a DAC at the output with a range from 0 to 2 V in 14 bits, corresponding to 122 μV for the least significant bit, implying a quantisation noise of 35.2 μV rms[4]. The output of the RedPitaya is later displaced by -1 V to bring it to a $\pm 1V$ range. This range is insufficient to drive our cavity's piezo, so it is later amplified outside the FPGA. To determine the effect of the quantisation noise, we perform a scan of the cavity length by modulating the piezo at a fixed amplification until we are able to see the PDH error signal, particularly the sideband. The width of the PDH signal corresponds to half the cavity width at the 1560 nm of the modulation[5] at a given amplification, which allows to obtain a conversion factor between the output voltage of the FPGA and the effect in frequency. Reducing the signal amplification reduces the quantisation noise but makes the lock unstable. For usual, stable amplifications, the inferred quantisation noise at the 780 nm cavity mode is about 30 kHz, about one-fourth of PSN (see 5.2.1), which is good enough in principle.

However, in 2016 L. Neuhaus [95] noted that for some gains, the DAC from the RedPitaya behaved nonmonotonically. This is due to the RedPitaya deriving the -1 V offset after the DAC directly from the 3.3 V digital supply voltage while lacking integrated voltage regulators. Because of this, every time the indicator LED flickers or the bits of the DAC itself toggle, the offset voltage is affected; this can remove at least 3 significant digits of precision[6], which in our case is already of the same order of magnitude as PSN. We followed the solution proposed by L. Neuhaus [96]: We modified the RedPitaya card and connected the output of its DAC directly to the SMA con-

[4] Considering a uniformly distributed noise from LSD of mean 0 and range 122 μV, leading to a standard deviation of $1/\sqrt{12}$ of the range

[5] $\frac{\gamma_{1560}}{2\pi} = 2.675$ MHz

[6] A factor of 6.6 in noise power according to L. Neuhaus [95]

nector. Then we shifted the output with a homemade level shifter that added a 1 V shift from a low-noise 2.5 V reference[7] connected to the fixed voltage divider.

[7] MAX6325: 1ppm/°C Max and 1.5 μV_{pp} Noise (0.1Hz to 10Hz)

5.2 Cavity Lock and Shift Inference

5.2.1 *Cavity Shift Inference*

To reduce the influence of low-frequency noise and eventual drifts of the cavity lock, we inferred the cavity shift by comparing the cavity resonance frequency in the presence of atoms with its bare resonance frequency during the same cycle. To reach this goal, at the end of each experimental cycle, after the atoms have left the cavity, the stripline current is turned on again to recover the same thermal conditions of the chip. With the cavity still locked, two probes are sent, one after the other, on both sides of the cavity profile to reconstruct the cavity profile. This cavity profile is used to compare the relative shift induced by the atoms.

Empty cavity shift. We set a relative origin at the centre frequency of the FSK toggle[8]. The cavity profile is known to have a line-width (FWHM) of $\kappa = 2\pi \times 45.8(6)$ MHz. For convenience, we introduce $\gamma = \kappa/2$. Let n_b, n_r be the number of photons measured at transmission for the probes at the blue and red profile, respectively. We use a photon counter of efficiency η. If the probes are detuned by $\pm p$ with respect to some reference. The cavity profile, centred at ω_0 can be described by the Lorentzian shape[9]:

$$n_b = \frac{I}{1+\left(\frac{p-\omega_0}{\gamma}\right)^2}, \qquad n_r = \frac{I}{1+\left(\frac{p+\omega_0}{\gamma}\right)^2}, \tag{5.2}$$

from which we can infer the cavity centre as

$$\tilde{\omega}_0 = \begin{cases} p\left(\frac{n_b+n_r}{n_b-n_r} - \sqrt{\left(\frac{n_b+n_r}{n_b-n_r}\right)^2 - 1 - \left(\frac{\gamma}{p}\right)^2}\right) & \text{if } n_b < n_r \\ 0 & \text{if } n_b = n_r \\ p\left(\frac{n_b+n_r}{n_b-n_r} + \sqrt{\left(\frac{n_b+n_r}{n_b-n_r}\right)^2 - 1 - \left(\frac{\gamma}{p}\right)^2}\right) & \text{if } n_b > n_r \end{cases}$$

and the maximal detected transmission at resonance, as we can simply solve for I:

$$\tilde{I} = \frac{n_b}{2}\left(1+\left(\frac{p-\tilde{\omega}_0}{\gamma}\right)^2\right) + \frac{n_r}{2}\left(1+\left(\frac{p+\tilde{\omega}_0}{\gamma}\right)^2\right). \tag{5.3}$$

Atoms in the cavity. When atoms are present in the cavity, a shift in the profile centre can be measured due to the phase shift induced by the atoms. Consider a probe with detuning sp, where s stands for the sign of the detuning. We detect n photons and assume that the

[8] Recall from section 4.3 that the probes are generated as a sideband of the 780 nm beam through an EOM. We choose a central frequency of about 2.41 GHz and toogle by ±20 MHz to probe either side

[9] With respect to our previous notation, $\delta = \omega_0 \pm p$, and $I = \left(\frac{\kappa_t}{4\gamma}\right)^2 \frac{\eta}{\gamma^2}|\eta_p|^2$, also for simplicity of calculations we introduce $\chi = n_b/n_r$

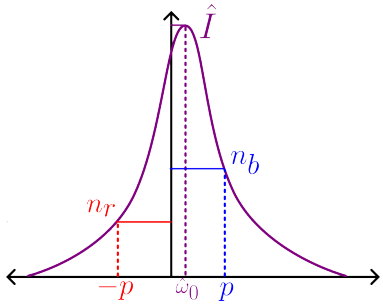

Figure 5.4: Knowing the cavity linewidth (HWHM) and two measurements on both profiles of the cavity transmission line, we can reconstruct a cavity profile to take our measurements of the cavity shift with respect to it.

presence of atoms does not affect the cavity's maximal transmission. We can infer the new cavity centre ω_0' as:

$$\delta\tilde{\omega}_c = \tilde{\omega_0'} - \tilde{\omega}_0 = ps - s\gamma\sqrt{\frac{\tilde{I}}{n} - 1} - \tilde{\omega}_0,$$

All our measurements are expected to be limited by photon shot noise. To account for this, we study the deviations[10] around $\omega_0 = 0$ where $\langle n_b \rangle = \langle n_r \rangle = n$. Since both photon measurements are not correlated, and $\sigma^2_{n_b} = \sigma^2_{n_r} = n$ we have from the typical error propagation formula[97]:

[10] Details and calculations can be found in 11.1.

$$\begin{aligned}
\sigma_{\omega_0} &\approx \sqrt{\left|\partial_{n_b}\omega_0\right|^2 \sigma^2_{n_b} + \left|\partial_{n_r}\omega_0\right|^2 \sigma^2_{n_r}} = \sqrt{2n\left(\frac{p^2+\gamma^2}{4np}\right)^2} \\
&= \frac{p^2+\gamma^2}{\sqrt{8n}p} \approx \frac{16.341\ \text{MHz}}{\sqrt{n}}, \\
\sigma_I &\approx \sqrt{\left|\partial_{n_b} I\right|^2 \sigma^2_{n_b} + \left|\partial_{n_r} I\right|^2 \sigma^2_{n_r}} = \sqrt{2n\left(\frac{p^2+\gamma^2}{4\gamma^2}\right)^2} \\
&= \frac{\sqrt{n}}{2\sqrt{2}}\left(1 + \left(\frac{p}{\gamma}\right)^2\right) \approx 0.623\sqrt{n}.
\end{aligned}$$

When we have atoms in the cavity, we measure n_s photons on the s side of the cavity. As before $\omega_0 \approx 0$ and also $\omega_0' \approx 0$. If the empty cavity calibration is done using n photons per probe and the interrogation is done using n_s, we can consider the typical error propagation formula[11]:

[11] We ignore any correlation between $\tilde{I}$ and $\tilde{\omega}_0$.

$$\sigma_{\delta\omega_c} = \frac{\gamma^2}{p}\left(1 + \frac{p^2}{\gamma^2}\right)\sqrt{\frac{1}{8n} + \frac{n}{32n_s^2} + \frac{1}{4n_s}}.$$

Moreover, we can introduce $r_p = n_s/n$:

$$\sigma_{\delta\omega_c} = \frac{\gamma^2}{2p\sqrt{n}}\left(1 + \frac{p^2}{\gamma^2}\right)\sqrt{\frac{1}{2} + \frac{1}{r_p} + \frac{1}{8r_p^2}}. \tag{5.4}$$

In practice, we consider two interrogation schemes to infer the cavity shift: the first consists of a first interrogation with $n_s = n$ followed by an echo MW+RF pulse and a second probe, then both measurements are considered together for the inference, i.e. $r_p = 2$. The second method considers a single long probe such that $n_s = 6n$, $r_p = 6$. Notice that there is a lower bound when $r_p \to \infty$ such that:

$$\sigma_{\delta\omega_c} \geq \frac{\gamma^2}{2p\sqrt{2n}}\left(1 + \frac{p^2}{\gamma^2}\right) \approx \frac{\kappa}{2\sqrt{2n}}, \tag{5.5}$$

as expected for an interrogation of the cavity at σ detuning with $2n$ photons [67].

5.3 Common Configuration

Most experiments described in the rest of this thesis are performed in similar conditions. To avoid redundancy, here is a description of the standard configuration used for the rest of the text unless otherwise specified.

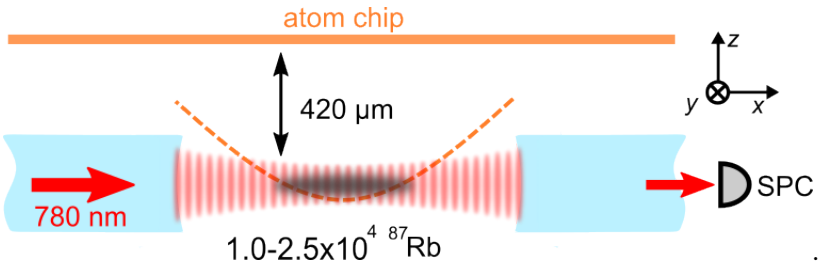

Figure 5.5: Magnetic trap and cavity scheme. ^{87}Rb atoms are magnetically trapped by the atom chip (the dashed orange curve illustrates the trap potential). The transmitted photons are collected by a single-photon counter (SPC). The absorption images are taken along $\hat{y}$. The cavity-locking light at 1560 nm is not shown. Figure retrieved from [65]

The trap. In the interrogation trap, the magnetic field at the bottom of the trap points along $\hat{x}$ and has a value $B_x = B_m - 35\,\mathrm{mG}$, where $B_m = 3.229\,\mathrm{G}$ is the "magic" field for which the linear differential Zeeman shift between the clock states vanishes [39]. The 35-mG offset maximizes the coherence time [72]. The trap is cigar shaped, with frequencies $\{\omega_x, \omega_y, \omega_z\}/2\pi \approx \{7.5, 122, 113\}\,\mathrm{Hz}$, with the cavity axis along $\hat{x}$. We operate at typical temperatures of $T \approx 200\,\mathrm{nK}$ transversely and atom numbers N between 6×10^3 and 2.1×10^4. The cloud is in the collisionless regime such that each atom preserves its motional energy over many oscillations in the trap (see the time scales in 5.2).

The cavity. The optical cavity is symmetric with a finesse $\mathcal{F} = 2.7(1) \times 10^3$ for the 780-nm mode. The cavity has a mode waist ($1/e$ radius) $w_0 = 13.6\,\mu\mathrm{m}$, length $L = 1215(20)\,\mu\mathrm{m}$, and line width (full width at half maximum) $\kappa/2\pi = 45.8(6)\,\mathrm{MHz}$. This gives a maximum single-atom cooperativity $C_0 = 24\mathcal{F}/\pi k_{780}^2 w_0^2 \approx 1.9$, where k_{780} is the wave vector of the probe laser. Considering the inhomogeneity for our trapped cloud with $T \sim 200\,\mathrm{nK}$, the effective cooperativity is $C_{\mathrm{eff}} \approx 0.42$. The cavity is simultaneously resonant for a stabilisation wavelength at 1560 nm. The stabilisation laser is constantly on during the experiment, but its intracavity intensity is sufficiently weak to prevent trapping of the atoms (trap depth $\lesssim 20\,\mathrm{nK}$).

Spin-cavity coupling. The cavity is tuned midway between the 780-nm D_2 transitions $|{\downarrow}\rangle \to 5P_{3/2}$ and $|{\uparrow}\rangle \to 5P_{3/2}$, such that to a good approximation $\delta\omega = \bar{\Omega} S_z$, where $\bar{\Omega} = \sum_i^N \Omega_i/N$ is the ensemble-averaged shift per spin flip and Ω_i is the coupling strength of the i-th atom. The value $\bar{\Omega} = 2\pi \times 16.3(3)\,\mathrm{kHz}$ has an uncertainty limited by the temperature and is determined experimentally by measuring the cavity shift after preparing a CSS with different $\langle S_z \rangle$.

Probe lightshift We calibrate the phase shift induced by the cavity probe using a Ramsey sequence (with the probe pulse occurring during the Ramsey time). We obtain the ensemble-average phase shift per detected photon $\bar{\phi}_d = 4.16(2) \times 10^{-4}\,\pi\,\mathrm{rad}$. Ideally, for a given atom i, the phase shift is given by $\phi_i = \frac{\Omega_i}{\kappa_t} n_t$, where n_t is the transmitted photon number and $\kappa_t = \mathcal{T}c/(2L) \approx \gamma$ is the transmission rate, in which $\mathcal{T} = 1000$ parts per million is the designed mirror transmission and c the speed of light. This allows us to estimate the

overall photon detection efficiency $\eta \approx 0.63(2)$ by comparing $\bar{\phi}_d$ with the expected phase shift per *transmitted* photon ($\langle \phi_i \rangle / n_t = \Omega_e / \kappa_t$).

Probing scheme. In our experiment, the inhomogeneity of the coupling Ω_i is predominantly in the transverse directions due to the cavity mode intensity profile. In contrast, it is almost averaged out by atomic motion along the cavity axis. To reduce inhomogeneity-induced dephasing [98, 99], we fix the probe-pulse duration to the vertical trap period, $\tau_p = 8.85\,\text{ms} = 2\pi/\omega_z \approx 2\pi/\omega_y$. Thus, Ω_i only depends on the transverse motional energy of an atom and remains constant until a lateral collision occurs. The remaining inhomogeneity between atoms with different motional energies is further suppressed by employing a spin-echo sequence as in previous experiments [98, 99].

For the first sequence of squeezing experiments described in 6.2, we measure $\delta\omega$ with a probe laser blue detuned from the cavity resonance by approximately γ [Fig. 5.6] and detect the transmitted photons using a single-photon counter, with an overall detection efficiency $\eta = 0.63(2)$. For the experiments after that one, we change to an FSK protocol that can toggle the frequency by $p = \pm 2\pi \times 20$ MHz with respect to the cavity resonance at $S_z = 0$. It will be clarified which probing scheme is being used when pertinent to do so. For each probing scheme, we have introduced the shape parameter β in equation (7.5); some typical values are:

$$\beta|_{p=\gamma} = \frac{7.07424 \times 10^{-4}}{\bar{\Omega}}$$
$$\beta|_{p=2\pi\times 20\,\text{MHz}} = \frac{7.00988 \times 10^{-4}}{\bar{\Omega}}$$

where we have included the factor $1/\bar{\Omega}$ for convenience.

Atomic coherence To determine the atomic coherence after a composite measurement M_1, we apply a second $\pi/2$ pulse after a first composite measurement M_1, forming a Ramsey sequence with M_1 occurring during the Ramsey time. By varying the phase of the second $\pi/2$ pulse, we obtain Ramsey fringes (S_z versus phase). However, M_1 induces an average phase shift depending on the measured S_z value, which fluctuates from shot to shot due to quantum projection noise. We correct this phase shift in the data analysis using the calibrated phase shift per detected photon and the number of detected photons in M_1 in each shot. We can then obtain the contrast with a sinusoidal fit to the Ramsey fringes. We fit the contrast decay as a function of average detected photons per probe to $\mathcal{C}(n_0) = \exp[-n_0/\gamma_1 - (n_0/\gamma_2)^2]$, in accordance to (2.20) yielding $\gamma_1 = 1.3(6) \times 10^5$, $\gamma_2 = 9.4(4) \times 10^3$.

Optimal interrogation Using (2.19) and our contrast calibration, we can infer an optimal number of photons yielding the best squeezing. Numerical optimisation with $p = 2\pi \times 20$ MHZ and our γ_1, γ_2 and

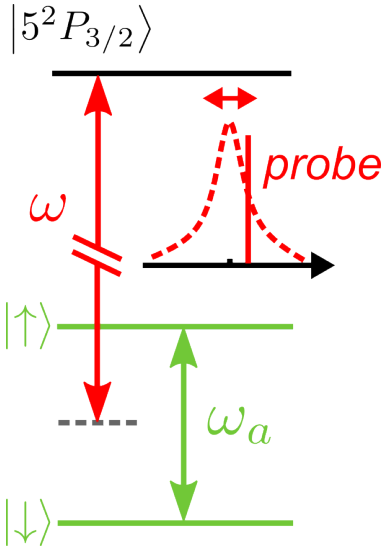

Figure 5.6: The energy level structure and the cavity-probing scheme. Figure retrieved from [65]

γ as above using $N \approx 1.8 \times 10^4$, give an optimal squeezing of -8.18 dB with $n_0 \approx 4.3 \times 10^3$ photons. Moreover, the squeezing remains below 8 dB for $n \in (4.0 \times 10^3, 7.0 \times 10^3)$

Imaging. $N_\uparrow$ and $N_\downarrow$ are also measured by absorption imaging after the time of flight (TOF). The state-resolved imaging starts with a MW pulse that adiabatically transfers atoms from $|\downarrow\rangle$ to $|F = 2, m_F = 0\rangle$, where they are no longer trapped and start to fall. The trap is turned off several milliseconds later to release atoms in $|\uparrow\rangle$ so that the two clouds are well separated and imaged in a single shot or picture. However, the adiabatic transfer also perturbs the trap, so the temperature estimation is slightly biased. We verify that both cavity and absorption measurements agree within the noise of the absorption imaging, which is close to the SQL [Fig. 5.7].

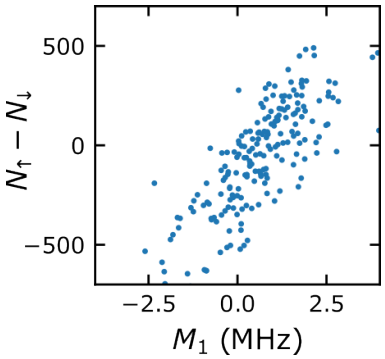

Figure 5.7: Typical data of the correlation of a cavity measurement with absorption imaging. The correlation with absorption imaging is limited by imaging noise, $\Delta(N_\uparrow - N_\downarrow) \sim 100$, comparable to the SQL. Figure retrieved from [65]

PSN threshold for cavity shift Considering an interrogation at $p = 20$ MHz and equation (5.4), we can evaluate both possible interrogation schemes: double with $r_p = 2$ and single long probe with $r_p = 6$

$$\sigma_{\delta\omega_c}|_{\gamma=2} = \frac{\gamma^2}{p\sqrt{n}}\left(1 + \frac{p^2}{\gamma^2}\right)\frac{\sqrt{66}}{16} \approx \frac{23.47\ \text{MHz}}{\sqrt{n}}, \tag{5.6}$$

$$\sigma_{\delta\omega_c}|_{\gamma=6} = \frac{\gamma^2}{p\sqrt{n}}\left(1 + \frac{p^2}{\gamma^2}\right)\frac{\sqrt{386}}{48} \approx \frac{18.92\ \text{MHz}}{\sqrt{n}}. \tag{5.7}$$

Also, we include the lower bound proposed in (5.5) for completeness:

$$\sigma_{\delta\omega_c}|_{\gamma\to\infty} = \frac{\gamma^2}{p\sqrt{8n}}\left(1 + \frac{p^2}{\gamma^2}\right) \approx \frac{16.34\ \text{MHz}}{\sqrt{n}}.$$

5.3.1 *Time Scales*

Table 5.2 summarizes the relevant time scales involved in the experiment.

Transverse trap frequency	$\frac{\omega_y}{2\pi}, \frac{\omega_z}{2\pi}$	≈ 120 Hz
Longitudinal trap frequency	$\frac{\omega_x}{2\pi}$	~ 7.5 Hz
Spin-exchange rate	$\frac{\omega_{\text{ex}}}{2\pi} = 2\hbar\lvert a_{\uparrow\downarrow}\rvert \bar{n}/m$	~ 1 Hz
Lateral collision rate	$\gamma_c = \frac{32\sqrt{\pi}}{3} a_{\uparrow\downarrow}^2 \bar{n} v_T$	~ 0.3 Hz
Background loss rate	γ_{1b}	~ 0.33 Hz
Phase-decoherence time		~ 0.05 Hz

Table 5.2: A summary of the experimental time scales, in which $\bar{n} \sim 1.6 \times 10^{11}$ cm^{-3} is the average atomic density, $a_{\uparrow\downarrow} \approx 98.09 a_0$, with $a_0 = 0.0529$ nm, is the relevant scattering length, m is the atomic mass, v_T is the thermal velocity $v_T \approx \sqrt{k_B T/m}$ and k_B is the Boltzmann constant.

Part III

Spin Squeezing and Spatial Correlations

6
Spin Squeezing Measurement Protocol

Most sections of this chapter and the following one are recovered from our work in [65]. However, I extended our model to describe more recent measurements and to improve our understanding. Because of this, some of the notation has been modified to simplify the matters.

6.1 Previous Calibrations.

6.1.1 *Average spin coupling*

To measure $\bar{\Omega}$, we prepare CSSs with different $\langle S_z \rangle$ via Rabi oscillations, *i.e.*by applying a weak MW+RF pulse of variable length. Cavity transmission spectra are obtained by scanning a weak probe laser over 20 cavity line widths in 50 ms. We obtain the prepared $\langle S_z \rangle$ from the imaging data. A linear fit of the cavity frequency versus the prepared $\langle S_z \rangle$ yields $\bar{\Omega}$. Our preparation procedure leads to a small dependence between the temperature and the prepared atom number. Therefore, the measured $\bar{\Omega}$ depends slightly on N (1.5% deviation for 10% change in N).

6.1.2 *Probe lightshift*

We calibrate the phase shift induced by the cavity probe using a Ramsey sequence with the probe pulse occurring during the Ramsey time. We obtain the ensemble-average phase shift per detected photon $\bar{\phi}_d = 4.16(2) \times 10^{-4}\,\pi\,\text{rad} = (7.49(4) \times 10^{-2})^\circ$. Ideally, for a given atom i, the phase shift is given by $\phi_i = \frac{\Omega_i}{\kappa_t} n_t$, where n_t is the transmitted photon number and $\kappa_t = \mathcal{T}c/(2L) \approx \sigma$ is the transmission rate, in which $\mathcal{T} = 1000$ parts per million is the designed mirror transmission and c the speed of light. This allows us to estimate the overall photon detection efficiency η by comparing $\bar{\phi}_d$ with the expected phase shift per *transmitted* photon, *i.e.*$\langle \phi_i \rangle = \frac{\bar{\Omega} n_0}{\eta \kappa_t} = \frac{\bar{\phi}_d}{\eta}$. This leads to the reported $\eta = 0.63(2)$. In practice, the expected lightshift $\langle \phi_i \rangle$ was calculated from Monte-Carlo simulations by Huang [67] to consider the thermal distribution and the spread of the cloud at 200 nK. However, the same result, within the resolution, can be obtained replacing $\bar{\Omega} \to \Omega_{\text{eff}}$, where Ω_{eff} is introduced in section 7.2.1 and

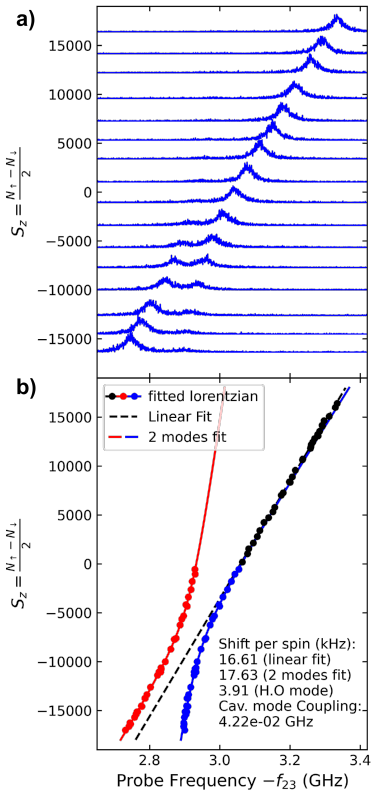

Figure 6.1: Cavity shif as a function of the population difference with σ^+ polarisation. The population difference is measured by absorption imaging. A linear fit obtains $\bar{\Omega}$. A two-mode fit shows the higher-order mode present on the red profile of the cavity: This mode couples with the atoms modifying the linear response of the cavity for large, negative vallues of S_z. The frequency axis is taken from the modulation applied to the EOM that generates this sideband.

obtained numerically.

6.1.3 *Coherence measurements*

To determine the atomic coherence after a composite measurement [Fig. 6.4(b) and Fig. 7.5, inset], we apply a second $\pi/2$ pulse after M_1, forming a Ramsey sequence with M_1 occurring during the Ramsey time. By varying the phase of the second $\pi/2$ pulse, we obtain Ramsey fringes (S_z versus phase). However, M_1 induces an average phase shift depending on the measured S_z value, which fluctuates from shot to shot due to quantum projection noise. We correct this phase shift in the data analysis using the calibrated phase shift per detected photon and the difference between the number of detected photons in the two probes that constitute M_1. We can then obtain the contrast with a sinusoidal fit to the Ramsey fringes.

6.2 Spin squeezing measurement

As described in section 2.2, monitoring the transmission of a cavity allows us to perform a measurement that reduces the uncertainty of the spin state. When captured by a magnetic field, we expect S_z to behave like a constant of motion, except for the one-body loss contribution, *i.e.* $\langle S_z(t)\rangle = \langle S_z(0)\rangle\, e^{-\gamma_{1b}t}$. A way to verify this reduction would be to measure the spin state again once the squeezing has been performed. If the technical noise coming from the second measurement and the one-body loss contribution is small enough, the discrepancy between the first and second measurements would be less than QPN; this is what we call conditional squeezing.

6.2.1 *Experimental sequence*

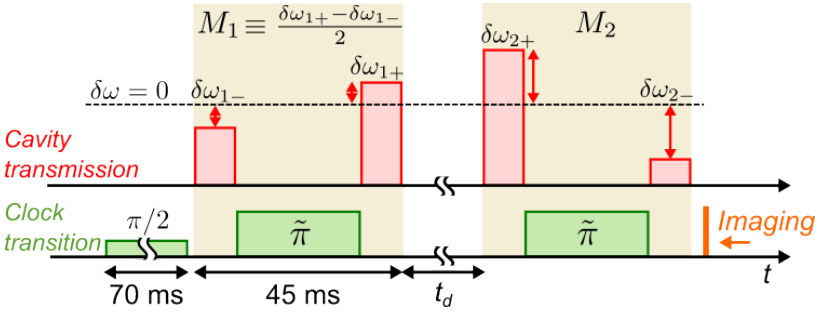

Figure 6.2: Squeezing and verification sequence. An experimental sequence with two composite cavity measurements, M_1 and M_2, for squeezing verification. The green boxes represent pulses on the clock transition, and the red boxes cavity-probe transmission, from which $\delta\omega_\pm$ are deduced. The delay t_d between measurements varies from milliseconds to 1 s. $\tilde{\pi}$ denotes a composite π pulse. Figure retrieved from [65]

An ensemble of $N \sim 2\times10^4$ ^{87}Rb atoms is magnetically trapped as in the trap described in section 5.3. As shown in Fig. 6.2. We start with all atoms in $|\downarrow\rangle$ and apply a $\pi/2$ pulse on the clock transition to prepare a CSS on the equator of the Bloch sphere. A composite cavity measurement M_1 measures the cavity detuning to determine S_z. A cavity measurement comprises two cavity-probe pulses separated by a π pulse on the clock transition [Fig. 6.2]. The measured S_z is deduced from the cavity shifts $\delta\omega_\pm$ of the two probe pulses

as $S_z = M/\bar{\Omega}$ where $M \equiv (\delta\omega_+ - \delta\omega_-)/2$. Then, a second identical measurement M_2 after a minimum delay $t_d = 6\,\text{ms}$ verifies the measurement uncertainty and spin squeezing.

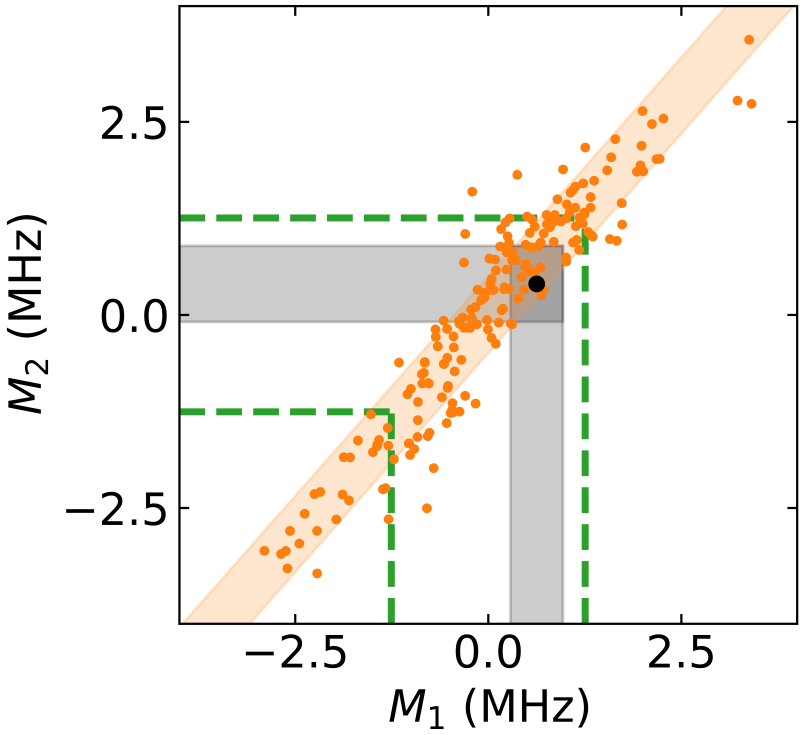

Figure 6.3: A squeezing measurement. Ensemble of 200 cycles for squeezing verification. Green dotted lines at $\pm\sigma_{\text{QPN}}$. The black dot is a representative data point; the vertical grey region represents 1σ PSN around the data point. The horizontal grey region representing 1σ of conditional noise $\sqrt{\text{Var}\,(M_2|M_1)}$ around the data point. The orange shading represents $\pm\sqrt{\text{Var}\,(M_2|M_1)}$ around a simple linear data fit. For context, in this set $\bar{n}_s \approx 4782.97$ photons, $\bar{N} \approx 23 \times 10^3$.

A QND measurement produces "conditional squeezing": M_1 yields a different result every time, following the quantum fluctuations of the CSS. The squeezing manifests itself in the correlation with the second measurement M_2, which for a squeezed state agrees with M_1 to be better than the SQL [41]. A typical ensemble of measurements would look like figure 6.3. We expect the noise distribution of the first measurement as a CSS with $\text{Var}\,(M_1) \approx \sigma^2_{\text{QPN}} + \sigma^2_{\text{PSN}}$ where $\sigma_{\text{QPN}} = \frac{\sqrt{N}}{2}\bar{\Omega}$ and $\sigma_{\text{PSN}} = \frac{23.255\,\text{MHz}}{\sqrt{n}}$ from equation (5.7) with $p = \gamma$ for this data set[1]. We have marked $\pm\sigma_{\text{QPN}}$ in green. Suppose we treat both measurements like a pair of correlated Gaussian variables. In that case, we can evaluate the uncertainty on predicting M_2 given M_1 as the conditional variance $\text{Var}\,(M_2|M_1) = \text{Var}\,(M_2) - \frac{\text{Cov}(M_1,M_2)^2}{\text{Var}(M_1)}$ which we would expect to correspond with[2] $\text{Var}\,(S_z|M_1)\,\bar{\Omega}^2 + \sigma^2_{\text{PSN}}$. Given one data point, as the one marked in black, we can associate a conditional spin state within its PSN resolution (shown in the vertical grey shading); then, we can associate a confidence interval where we expect M_2 to be found approximately within $\text{Var}\,(M_2|M_1)$ (shown in the horizontal grey shading), the reduction of this confidence interval with respect to σ_{QPN} is the conditional squeezing. As we will see in the following subsection, our experiments do show a reduction of noise[3], but it does not follow a simple relationship as the ones described above due to spin interactions to be discussed in the next part of this manuscript.

[1] We emphasise here that we would also expect $\text{Var}\,(M_1) \approx \text{Var}\,(M_2)$ since for such a short delay, the one-body losses should be negligible. However, $\text{Var}\,(M_2)\,/\text{Var}\,(M_1) = 1.45$ for this data set for reasons to be discussed in the next part of the manuscript.

[2] Ignoring one-body losses terms.

[3] $\text{Var}\,(M_2|M_1)\,/\sigma^2_{\text{QPN}} \approx 8.12$ dB for the data plotted.

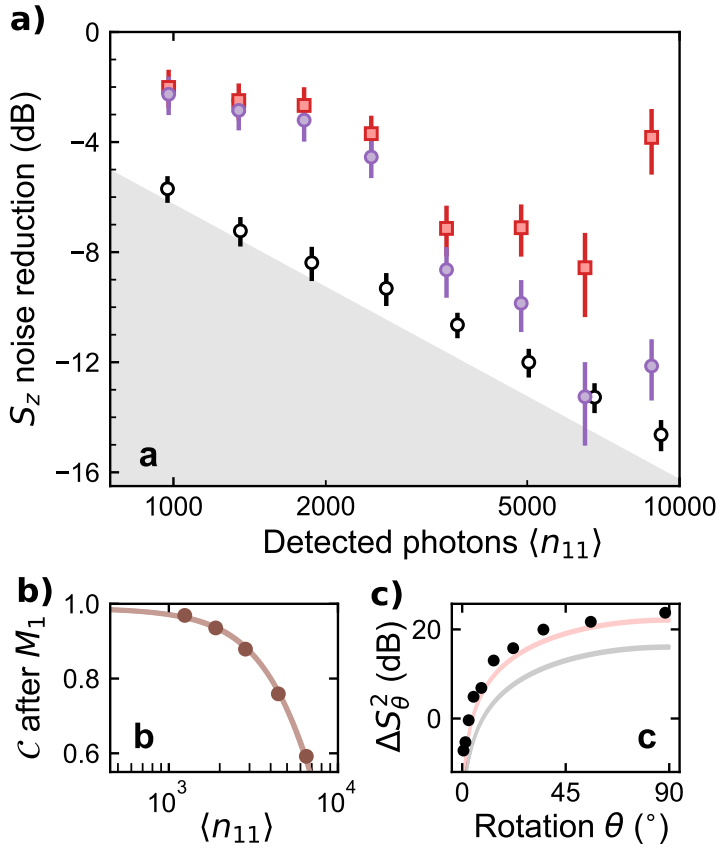

Figure 6.4: a) Conditional squeezing results for $N = 1.8(1) \times 10^4$ atoms and minimum delay ($t_d = 6\,\mathrm{ms}$) between measurements M_1 and M_2. The variance values are normalized to the SQL ($N/4$) and expressed in decibels. The cavity measurement without atoms (open circles) approaches the photon-shot-noise (PSN) limit (the boundary of the shaded zone). The number squeezing ξ_N^2 (purple circles) (Eq. 6.1) decreases to below $-12\,\mathrm{dB}$. After normalizing by the independently measured coherence (panel b)), we obtain the metrological squeezing (red squares), reaching an optimum of $8.6^{+1.8}_{-1.3}\,\mathrm{dB}$ for $13.0(2) \times 10^3$ photons. The error bars indicate 1σ confidence and are obtained with a bootstrapping method. b) The Ramsey contrast $\mathcal{C}$ as a function of the measurement strength. The curve is a fit to $\mathcal{C} = \exp[-n_s/\gamma_1 - (n_s/\gamma_2)^2]$ (See 5.3). Its thickness indicates the fit uncertainty. **c**, The spin-noise tomography at $\langle n_1\rangle = 4.5(1) \times 10^3$, measured by inserting, between M_1 and M_2, a rotation θ around $\langle \hat{\mathbf{S}}\rangle$. The grey curve represents the theoretical minimum uncertainty state, while the red curve considers the phase noise induced by the PSN of M_1. Figure retrieved from [65]

6.2.2 *Spin squeezing by QND measurement*

Noise is quantified from the variance of 200 repetitions of this sequence. First, we perform this protocol with no atoms in the cavity to determine the noise floor [Fig. 6.4(a), open black circles]. The result is close to the photon shot noise (PSN) of the detected photons, given by $\Delta M_l|_{\mathrm{PSN}} = \frac{33\gamma^2}{32 n_s}$, where $n_s = \langle n_{l1}\rangle \langle n_{l2}\rangle$ is the average number of detected photons per probe on each measurement ($l = 1, 2$). For the atom number $N = 1.8(1) \times 10^4$ used here, the PSN falls below the SQL for $n_s \gtrsim 500$ detected photons, allowing for spin-noise reduction by the cavity measurement.

With two measurements performed on the same sample with negligible delay, the spin noise of the state after M_1 can be quantified as

$$\left(\Delta S_z|_{M_1}\right)^2 = \frac{1}{\bar{\Omega}^2}\left[\mathrm{Var}\left(M_2 - \zeta M_1\right) - \left(\Delta M_2|_{\mathrm{PSN}}\right)^2\right], \tag{6.1}$$

where ζ is chosen such that it minimizes the variance[4] (and hence accounts for systematic differences between the two measurements) [100]. To assess the spin noise after M_1, it is legitimate to subtract the detection noise of the verification measurement M_2, which contains the PSN, $\left(\Delta M_2^{\mathrm{psn}}\right)^2$, plus technical noises such as cavity-lock fluctuations. In Eq. 6.1, we conservatively subtract only the PSN to obtain an upper bound for $\Delta^2 S_z$. Fig. 6.4(a) (purple circles) shows it as a function of the number of detected photons in M_1. It is normalized to the SQL to give the number squeezing $\xi_N^2 = 4\Delta^2 S_z/N$ [53].

[4] This does not look like the measure of noise we presented in the previous paragraph $\mathrm{Var}\left(M_2|M_1\right)$, but one can prove that:

$$\min_\zeta \mathrm{Var}\left(M_2 - \zeta M_1\right) = \mathrm{Var}\left(M_2|M_1\right)$$

The metrological squeezing $\xi^2 = N\Delta^2 S_z / |\langle \hat{\mathbf{S}} \rangle|^2 = \xi_N^2 / \mathcal{C}^2$, which characterizes the enhancement in angular resolution on the Bloch sphere compared to the SQL [52], additionally requires assessing the coherence, namely, the Ramsey-fringe contrast $\mathcal{C} = 2|\langle \hat{\mathbf{S}} \rangle|/N$. We do this by applying a second $\pi/2$ pulse with a variable phase after M_1 and then measuring S_z by imaging [Fig. 6.4(b)]. The resulting Wineland squeezing factor is shown as red squares in Fig. 6.4(a). We obtain a maximum metrological squeezing at optimal parameters of $8.6^{+1.8}_{-1.3}$ dB, with about $n_s = 6500$ detected probe photons. The optimum results from the competition between photon shot noise, which favours a higher photon number, and photon-induced decoherence.

Spin Tomography. To fully characterize the squeezed state, we also perform spin-noise tomography [98, 101] by inserting a pulse on the clock transition between M_1 and M_2 to rotate the noise distribution around $\langle \mathbf{S} \rangle$ [Fig. 6.4(c)]. Notice that for $S_z \neq 0$, the number of photons detected will differ by approximately $2n_0\beta\bar{\Omega}S_z$ between the first and second probe in M_1. The discrepancy on the detected number of photons translates into a phase fluctuation due to the induced lightshift by the probe[5]. The data shown in figure 6.4(c) is taken with $n_s = 4.5(1) \times 10^3$. To ensure we rotate around $\langle \mathbf{S} \rangle$, we post-select for all measurements such that $S_z = 0$ within PSN. For reference, we consider a state that saturates the uncertainty bound $\sigma_s \sigma_a = \frac{N}{4}$, (figure 6.4(c), grey curve[6]). The figure shows an excess anti-squeezing of 7.4 dB (at 90° rotation) above the minimum-uncertainty state. Once we include the PSN contribution[7] via shot-to-shot fluctuation of phase, we obtain the red curve; thus, we mostly attribute the excess atnisqueezing to the shot-to-shot phase noise caused by the PSN in M_1.

[5] More precisely $\bar{\phi} = \frac{2n_0\beta\bar{\Omega}^2}{\kappa_t \eta} S_z$ as we will show in section 7.3

[6] The noise distribution for a gaussian state with principal quadratures σ_s, σ_a rotated an angle θ around its centre is given by $\sigma(\theta) = \sqrt{\sigma_s^2 \cos^2\theta + \sigma_a^2 \sin^2\theta}$

[7] $\sqrt{\mathrm{Var}\,(S_z)}\Big|_{\bar{\phi}} \approx \frac{N\mathcal{C}}{2} \sin\left(\frac{\bar{\Omega}}{\eta\kappa_t}\sqrt{n_0}\right)$

6.2.3 *Lifetime*

The long phase-coherence time in our experiment allows us to observe the evolution of the spin-squeezed states over much longer time scales than in previous experiments. From the formula (2.18), we expect the state's squeezing to have a lifetime comparable to the lifetime of the atoms in the trap, *i.e.* 3.0(1) s. This is expected to be an upper bound since our theory did not consider other loss mechanisms apart from one-body losses.

To verify this, we perform the verification measurement M_2 after longer times T_d up to 1 s. Tracing M_2 as a function of M_1, we notice immediately that $M_2 \neq M_1$. However, we find that a strong linear correlation between the measurements persists for all measurement times, but surprisingly, its slope depends on T_d [Fig. 6.5(a)]. The slope α of a linear fit to the data increases to values up to approximately 4 for times $t_d \lesssim 300$ ms, then decays back to values close to 1 [Fig. 6.5(b)]. We included in green σ_{QPN} corresponding to the final atom number measured. Notice that M_2 exceeds QPN by many factors, which should be visible through imaging if this came from a

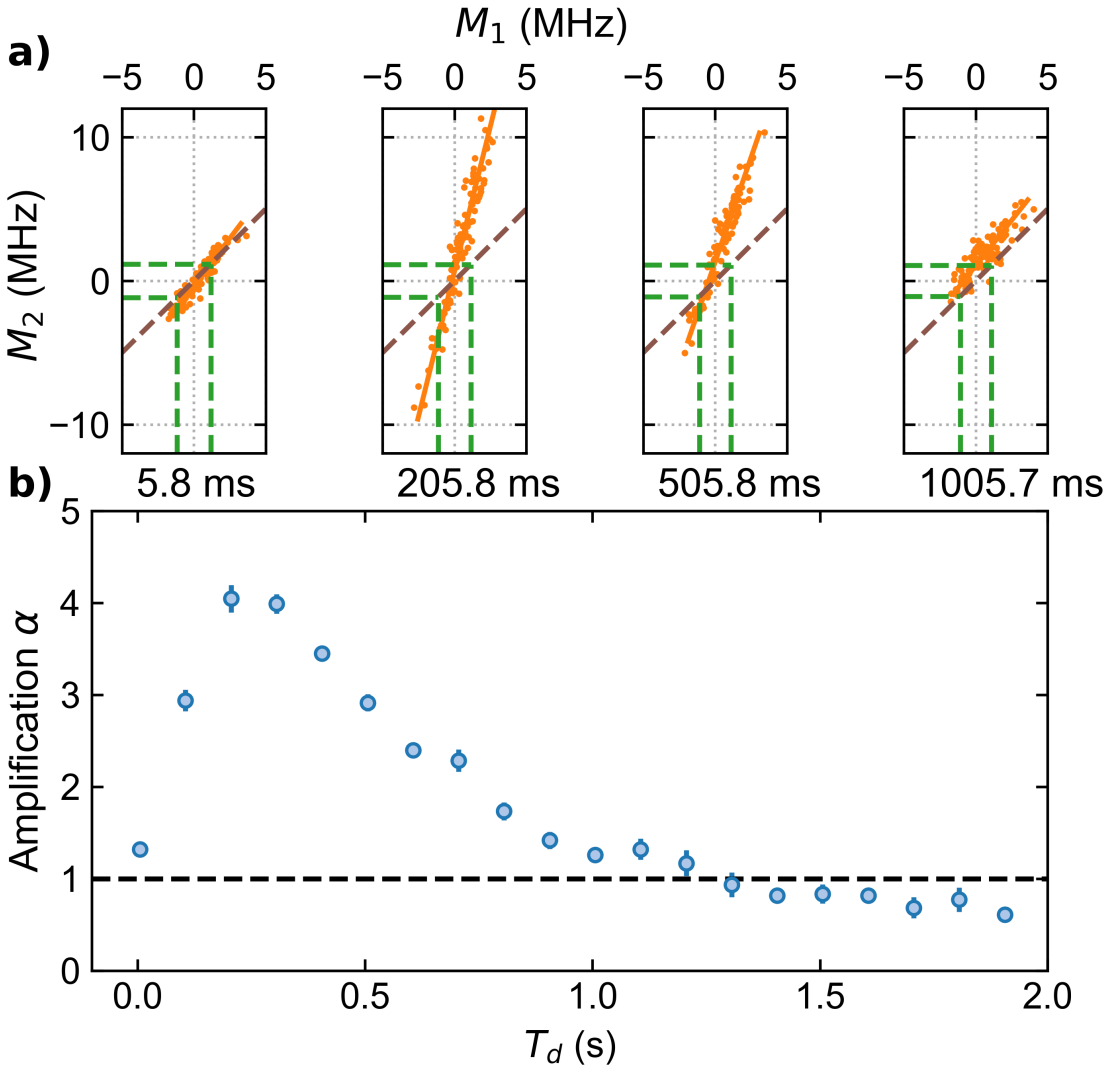

Figure 6.5: a) Same protocol as the one depicted in figure 6.2 with a larger delay t_d between M_1 and M_2. Linear dependence between the two measurements remains, while the second measurement shows an amplified cavity shift with respect to the first one as $M_2 = \alpha M_1$. Once again, σ_{QPN} is marked in green. b) The slope obtained by simple least-square for different delays. An increase is observed around 250 ms and then reduces back to 1.

correlated change in S_z.

Using absorption imaging, we confirm that S_z itself does not measurably evolve when α increases, with $\mathrm{Var}\left(\frac{N_2-N_1}{2}\right)$ remaining well within $[0.57, 1.45]\sigma^2_{\mathrm{QPN}}\mathcal{C}^2$, indicating that the amplification of M_2 is linked to the measurement rather than to the spin state itself. More precisely, as elaborated in the next chapter, the origin of the amplification is not a change in the mean spin direction but a change in the effective coupling between the cavity and the atoms due to spin-spin interactions.

7
Amplification

7.1 Experimental Observations of Amplification

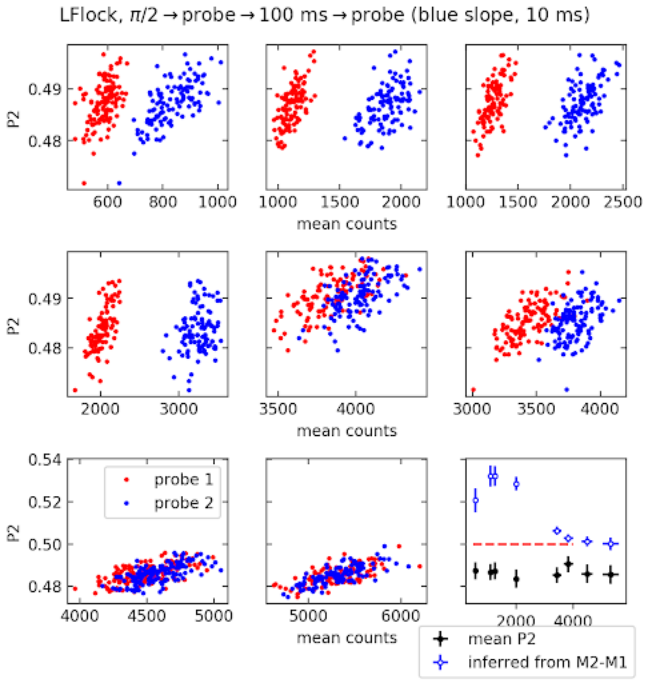

Figure 7.1: In the vertical axis, P_2 is inferred directly from camera data, while the horizontal axis shows the count of the two probes, both in the blue profile of the cavity. We notice that for some cases, the transmission almost doubles, corresponding to a shift of half a cavity width. We notice that, after some point, the difference decreases as the number of photons in the first probe increases. Today, we can understand this due to the loss of contrast induced by inhomogeneous dephasing, which hides the effect to be described in this chapter.

We first observed the measurement of amplification in TACC 2 in 2018. A first probe was sent through the atomic ensemble, followed by a $\pi/2$ pulse and a second identical measurement. For short delays, of around 10 ms both measurements remained identical within the expected photon shot noise and well below QPN from 1000. However, when the separation between probes increased, the difference between both measurements increased significantly depending on the relative detuning of the probe with respect to the cavity resonance. Further investigation showed that the cavity transmission of the second probe was amplified due to an unexpected cavity shift after the first probe.

The magnitude of the shift seemed to increase as a function of the delay after the first probe until it plateaus, sometimes after a short dip. The maximal shift increases with the number of atoms for fixed trap frequencies. A statistical ensemble was prepared, and the same

experiment was conducted instead of using a *CSS*. A shift on the cavity transmission was observed, but the dependence on time was no longer there, implying that what was being observed came from a coherent process. Finally, the spin state was checked using the camera; the shift was large enough for it to be noticeable within the resolution of the camera if S_z had changed. This implied that it was a change in the way the atoms were coupled to the cavity instead of a change in the z component of spin.

Discussions with collaborators at the time pointed to the work Piéchon et al. [102] that developed an explanation of different effects of spin segregation [103–105] and other dynamics based on mechanisms of Identical Spin Rotation Exchange (ISRE). This allowed us to develop a model in which phase inhomogeneities correlated with the state of motion of the atoms in the trap, together with spin interaction, led to the observed effect. As a result of these discussions, a model based on energy classes was presented by Huang [67] for his thesis. Here, I present a version of the model we presented in [65] that allows us to discuss how different probing schemes give us control over the amplification. We first discuss how the inhomogeneous coupling gives rise to a correlated dephasing, how the interactions transfer this dephasing into the coupling of the z component of spin and how this gives rise to the amplification.

7.2 Ingredients for amplification

7.2.1 Inhomogeneous coupling

The atom-field coupling in the cavity is a function of the atomic trajectory $\vec{r}(t)$ and is determined by the cavity geometry:

$$\Omega(\vec{r}) = \Omega_0 \cos^2(k_{780}x)\left(\frac{w_0}{w}\right)\exp\left[-2\frac{y^2+z^2}{w^2}\right], \tag{7.1}$$

where $w = w_0\sqrt{1+x^2/L_R^2}$, in which $L_R = k_{780}w_0^2/2 \approx 750\,\mu$m the Rayleigh length. The maximum shift Ω_0 can be obtained from the experimentally measured $\bar{\Omega}$ and agrees with the value obtained from a cavity quantum electrodynamic calculation. The time-integral of $\Omega(\vec{r})$ over the pulse duration τ_p yields the effective coupling $\Omega_i = \frac{1}{\tau_p}\int_0^{\tau_p} dt\Omega(\vec{r}_i)$ for the i-th atom. Assuming harmonic oscillation, the position dependence in the transverse directions reduces to a function of the motional energies $E_{y,i}$ and $E_{z,i}$:

$$\Omega_i \approx \Omega_0\left(1-\frac{x_i^2}{L_R^2}\right)e^{-\left(\frac{E_{y,i}}{\varepsilon_y}+\frac{E_{z,i}}{\varepsilon_z}\right)}I_0\left(\frac{E_{y,i}}{\varepsilon_y}\right)I_0\left(\frac{E_{z,i}}{\varepsilon_z}\right), \tag{7.2}$$

where $\varepsilon_y \equiv \frac{m\omega_y^2 w_0^2}{2}$ and $\varepsilon_z \equiv \frac{m\omega_z^2 w_0^2}{2}$. In the experiment, the averaging is imperfect along $\hat{y}$ since ω_y and ω_z are not precisely equal. $I_0(\cdot)$ is the modified Bessel function of the first kind. Note that we assume that the standing wave in $\hat{x}$ can be averaged out and that the position dependence on x is weak as the cloud size $\ll L_R$. As a result, the

atoms contribute differently to the quantum fluctuations of $\delta\omega = \bar{\Omega}S_z$.

Nevertheless, the system can be described as a uniformly coupled one with a slightly reduced effective atom number $N_{\text{eff}} = \frac{(\sum_i^N \Omega_i)^2}{\sum_i^N \Omega_i^2}$ and coupling $\Omega_{\text{eff}} = \frac{\sum_i^N \Omega_i^2}{\sum_i^N \Omega_i}$, as long as the couplings do not change over time[46]. Note that[1] as

$$N_{\text{eff}}\Omega_{\text{eff}} = N\bar{\Omega} \quad \text{and} \quad \xi^2 = 4(\Delta S_z)^2|_{M_1}/(N\mathcal{C}^2) \propto 1/N\bar{\Omega}^2,$$

the squeezing will appear higher if N_{eff} and Ω_{eff} are used. For our system, $N_{\text{eff}} \approx 0.90N$ and $\Omega_{\text{eff}} \approx 1.11\bar{\Omega}$, so that the effect on ξ^2 is within 10%. We use N (measured by imaging) and $\bar{\Omega}$ to obtain a conservative estimate of squeezing. Also, $\text{Var}(\Omega) = 0.1131\bar{\Omega}^2$

[1] The coefficients $N_{\text{eff}} \approx 0.90N$ and $\Omega_{\text{eff}} \approx 1.11\bar{\Omega}$ where obtained via Montecarlo simulation of the cloud at the corresponding temperature and atom number.

7.2.2 *Spin-Exchange Interaction*

The Identical Spin Rotation Effect (ISRE) is a phenomenon in spin-polarized systems that has manifested itself in cold atom systems. This is at the origin of spin waves, first predicted by Bashkin [106] and Lhuillier and Laloë [107]; since then, it has been reported in multiple experimental set-ups [39, 72, 104, 105, 108–113], accompanied by the development of the theory necessary to study such systems[102, 103, 114–117]. The effect can be explained from the difference of effective energy interaction between parallel and antiparallel spins[107]; this asymmetry leads to precession between the triplet and singlet states[118].

Consider two spin-$\frac{1}{2}$ particles with two-body collision interaction $\hat{H}_{int}$ described by a term proportional to $\hat{P}_{\text{singlet}}$, the projector to the singlet state. It is possible to show that $\hat{H}_{int} \propto \frac{1}{4} - \hat{s}_1 \cdot \hat{s}_2$. The energy split coming from the term $\hat{s}_1 \cdot \hat{s}_2$ gives rise to the spin rotation; this is apparent directly from the equation of motion $\partial_t \hat{s}_1 \propto -\hat{s}_1 \wedge \hat{s}_2$, which resembles an equation describing the precession of $\hat{s}_1$ around a magnetic field proportional to $\hat{s_2}$. In the case of ^{87}Rb, the scattering lengths $a_{\uparrow\uparrow}$, $a_{\downarrow\downarrow}$ and $a_{\uparrow\downarrow}$ are almost identical[2]. This shift the spin-symmetric triplet states by the same energy, but not the singlet, leading to the same spectrum as that of a fermion, allowing us to treat it as such [72, 103, 120].

[2] More precisely[119]:

$$a_{\uparrow\uparrow} = 95.47a_0,$$
$$a_{\downarrow\downarrow} = 100.44a_0,$$
$$a_{\uparrow\downarrow} = 98.09a_0.$$

A complete mean-field treatment [36, 36, 72, 102] yields a similarly intuitive picture. Considering an energy-dependent spin density $\mathbf{S}(E_x, E_y, E_z, t)$:

$$\partial_t S + \gamma_c (\mathbf{S} - \langle \mathbf{S} \rangle) \approx (\Delta_D \vec{e}_z + \omega_{\text{ex}} \langle \mathbf{S} \rangle) \wedge \mathbf{S}. \tag{7.3}$$

The term Δ_D is energy-dependent, including the Zeeman shift from the harmonic trap and the mean-field shift contribution from the density. The second term in equation (7.3), $\omega_{\text{ex}} \langle \mathbf{S} \rangle \wedge \mathbf{S}$, is the ISRE term that manifests as a rotation of the spin distribution around its average value with an exchange rate given by the forward scattering rate $\frac{\omega_{\text{ex}}}{2\pi} = \frac{2\hbar|a_{\uparrow\downarrow}|\bar{n}_{\text{at}}}{m_{\text{Rb}}}$. Additionally, we find a diffusion term proportional to the lateral collision rate $\gamma_c = \frac{32\sqrt{\pi}}{3} a_{\uparrow\downarrow}^2 \bar{n}_{\text{at}} v_T$. Notice

that, for low temperatures, the thermal velocity v_T tends to zero, suppressing the lateral collisions. In our experiment, $\frac{\omega_{ex}}{2\pi} > \gamma_c$, which allows us to see the effect of the spin exchange before damping out.

We remark that the dephasing term Δ_D is at the origin of dynamics previously reported in TACC-1 [72]: a dephasing arises due to the harmonic shape of the trap, then the forward-collision term allows for the "exchange" of the direction of dephasing, effectively rephasing the spin of the sample. In TACC-2, this term is still present, but it is not the main driver of our dynamics. In TACC-2, the inhomogeneous lightshift, correlated with the transversal energy distribution, induces dephasing. We could think of it as a term Δ_D that is present only during the probe or as the initial conditions for the evolution dominated by the exchange term after the probe.

7.2.3 *Cavity in linear-regime*

For this section, we consider a linear approximation of the cavity shape for our analytical treatments[3]. To avoid carrying a factor of 2π everywhere, we write all detuning in radians per second. For a cavity detuning of p, we introduce the raw transmission as $T_0 = T(\pm|p|)$ and expand around p:

$$\begin{aligned} T(p + \bar{\Omega}S_z) &= T_0\left(1 - \frac{1}{1+(p/\gamma)^2}\frac{2p}{\gamma^2}\bar{\Omega}S_z\right) \\ &= T_0(1 - \beta\bar{\Omega}S_z). \end{aligned}$$

Say we send a fixed-duration probe for a total amount of n_p photons.

[3] All data analysis considers the shape $T(\delta\omega) = \left(\frac{\kappa_t}{4\gamma}\right)^2 \frac{1}{1+(\delta\omega/\gamma)^2}$ to infer the cavity detuning, where $\delta\omega$ is the detuning with respect to resonance in radians per second. Due to mode matching, we note that our experiment is such that $\kappa_t \approx \gamma$

Theorem 1 (Transmitted photons in linear regime)**:**

For a photon detection efficiency η and n_p probe photons, the linear relationship between the z component of spin and the detected cavity transmission

$$n = n_0(1 - \beta\bar{\Omega}S_z) \tag{7.4}$$

$$\beta = -\frac{1}{n\Omega}\frac{\mathrm{d}n}{\mathrm{d}S_z}\bigg|_{S_z=0} = \frac{1}{1+(p/\gamma)^2}\frac{2p}{\gamma^2} \tag{7.5}$$

$$n_0 = n_p T_0 \eta$$

Notice that for a CCS prepared in the equator of the Bloch sphere, n_0 is the average of detected photons across many cycles, while n_0/η is the average number of transmitted photons

7.3 Microscopic semi-classical model of amplification

Here, we formulate a simple semiclassical model that reproduces the amplification effect. We make the following assumptions:

1. Ω_i is only determined by $E_{y,i}$ and $E_{z,i}$, which are conserved during the experiment (Eq (7.2)). The coupling of the ensemble $\bar{\Omega} = \frac{1}{N}\sum_i^N \Omega_i$ is then a constant.

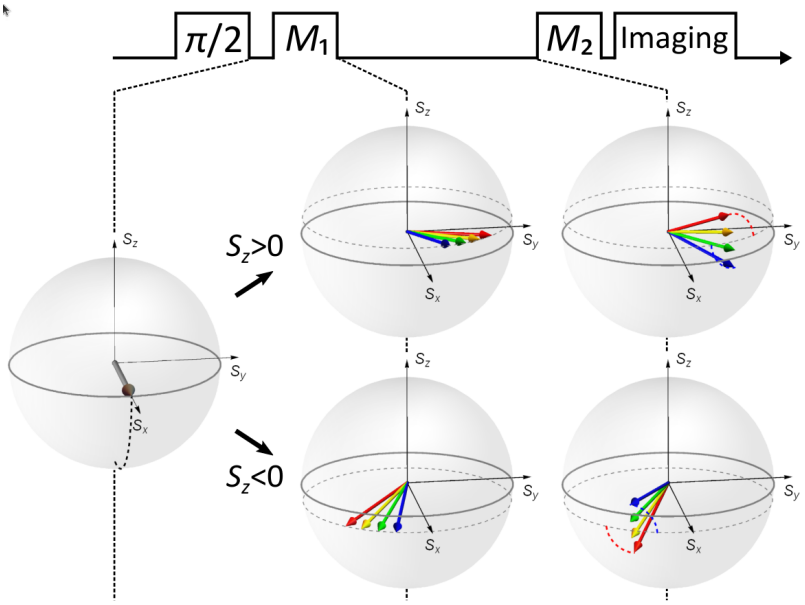

Figure 7.2: Intuitive picture of the amplification effect in the single-atom Bloch sphere. Atoms are prepared in phase by the $\pi/2$ pulse (left column). The centre column shows the situation just after the measurement M_1. Two cases are shown, one where the measurement result was $S_z > 0$ (upper row) and one where it was $S_z < 0$ (lower row). Each arrow depicts a single atom, with its colour representing the coupling Ω_i, which depends on motional energy (blue: higher energy, $\Omega_i < \bar{\Omega}$; red: lower energy, $\Omega_i > \bar{\Omega}$). Cold, well-coupled atoms (red arrows) lead when $S_z > 0$ (upper row) and lag when $S_z < 0$ (lower row). During evolution under ISRE (right column), individual spins rotate around their sum, acquiring different individual s_z components while the total S_z is conserved. For short times, well-coupled atoms rotate above (below) the average if $S_z > 0$ ($S_z < 0$). As these atoms make an above-average contribution to the cavity shift, the second measurement performed at this stage yields an amplified signal. Note that if $S_z = 0$ is measured, atoms remain in phase (thick grey arrow), and no spin dynamics occur.

2. The spin rotation is modelled as a simple rotation of each spin around the average of the ensemble with the same rate $C\omega_{ex}$, determined by the atomic coherence. We ignore other sources of dephasing, such as dephasing from the trapping potential.

3. We also assume a perfect π pulse on the clock transition for the spin echo and no spin dynamics during the composite measurement.

The general idea of the model is depicted in figure 7.2. During a given sequence, atoms are initially prepared in a CSS on the equator, say $|\frac{\pi}{2}, 0; N\rangle$. A first measurement M_1 projects the spin component close to the equator, say $S_z > 0$ for a particular sequence cycle. The fact that the number of photons in both probes of M_1 leads to an uncompensated phase shift that is correlated with the spin we just measured. For a given atom i, this phase shift also depends on its coupling Ω_i, so that we have $\phi_i \propto \Omega_i S_z$. As Ω_i, in turn, depends on the transverse motional energy of the atom, this corresponds to a spin-orbit coupling where atoms with small oscillation amplitude experience above-average phase shift. This correlation persists until collisions redistribute motional energy, i.e., for a time on the order of 3 s in our experiment.

Second, spin-exchange interaction rotates individual spins about the axis of total spin at rate ω_{ex}, thus converting the phase-shift deviation $\delta\phi_i$ of an atom from the ensemble mean into population difference $\delta s_{z,i}$. [4] While this interaction conserves total spin, it does convert the initial correlation $\delta\phi_i \propto \Omega_i$ into a correlation $\delta s_{z,i} \propto \Omega_i$, which will affect the result of a subsequent cavity measurement. In the case of our measurement scheme, the spin-rotation direction is such that for short times, atoms with above-average coupling ($\Omega_i > \bar{\Omega}$) acquire $\delta s_{z,i} > 0$ if $S_z > 0$ and vice versa: strongly coupled atoms acquire an

[4] Note, however, that the squeezed axis remains unchanged, *i.e.*, along z, because the interaction can be described by a Hamiltonian $\propto \hat{\mathbf{S}} \cdot \hat{\mathbf{S}}$ which is a constant of motion that commutes with $\hat{S}_z$ [110].

increased population difference, $\langle s_{z,i}\rangle|_{\Omega_i>\bar{\Omega}} = AS_z/N$ with $A > 1$. As these atoms make a dominant contribution to the cavity shift, a second cavity measurement is amplified with respect to M_1.

The phase shift induced by M_1 is obtained from the number of photons transmitted n_{1k} in the two probe pulses. With a linear approximation of the cavity transmission (probe detuning p_k), $n_{1k} = \frac{n_0}{\eta}(1 \mp \beta_k \bar{\Omega} S_z)$, from which $n_0 = \langle n_{1k}\rangle \eta$ is the average *detected* photon number during the M_{1k} interrogation[5]. According to our sign convention, the first probe gives $\phi_{i1} = \frac{\Omega_i}{\kappa_t}\frac{n_0}{\eta}(1 - \beta_1 \bar{\Omega} S_z)$ (note the sign of S_z, which acquires another minus sign after the spin-echo pulse). The second probe gives $\phi_{i2} = \frac{\Omega_i}{\kappa_t}\frac{n_0}{\eta}(1 + \beta_2 \bar{\Omega} S_z)$ and the total phase shift in M_1 reads

$$\phi_i = \phi_{i2} - \phi_{i1} = \frac{\Omega_i}{\kappa_t}\frac{n_0}{\eta}(\beta_2 + \beta_1)\bar{\Omega} S_z. \tag{7.6}$$

[5] We distinguish the shape parameter β_k for both first and second probe to consider different interrogation schemes, the reason for this will be elaborated in section.

For small phase deviations, the mean phase is

$$\begin{aligned}\bar{\phi} &= \arctan\left(\frac{\sum_i \sin(\phi_i)}{\sum_i \cos(\phi_i)}\right) \approx \frac{1}{N}\sum_i \phi_i \\ &= \frac{\bar{\Omega}}{\kappa_t}\frac{n_0}{\eta}\bar{\Omega}(\beta_2 + \beta_1) S_z.\end{aligned} \tag{7.7}$$

From which the phase deviation from the mean of atom i is:

$$\Delta\phi_i = \phi_i - \bar{\phi} = \frac{n_0}{\eta\kappa_t}(\beta_2 + \beta_1)\bar{\Omega}(\Omega_i - \bar{\Omega}) S_z = \chi \delta_i S_z, \tag{7.8}$$

where we introduce the *precursor factor* $\chi = \frac{n_0}{\eta\kappa_t}(\beta_2 + \beta_1)\bar{\Omega}$ of the probing scheme and the coupling discrepancy[6] $\delta_i = \Omega_i - \bar{\Omega}$. The cavity would not measure this phase distribution until the spin-exchange collisions rotate individual spins about the total spin [72, 102]. The effect of the ISRE is then to rotate individual spins about their sum. The rotation rate is determined by $\mathcal{C}\omega_{\mathrm{ex}}$. While the total S_z is conserved, the s_z values of individual atoms evolve as

$$s_{z,i}(t) = s_z^0 + \frac{\Delta\phi_i}{2}\sin \mathcal{C}\omega_{\mathrm{ex}} t. \tag{7.9}$$

[6] Note that this definition leads to $\sum_i \delta_i = 0$

The initial value is close to $s_z^0 = S_z/N$ for all atoms due to the QND measurement, and the plus sign is determined by the relevant scattering lengths in ^{87}Rb [103]. We then obtain cavity shift of M_2:

$$\begin{aligned}\delta\omega(t) &= \sum_i^N \Omega_i s_{z,i}(t) \\ &= \sum_i^N \Omega_i \left(s_z^0 + \frac{\Delta\phi_i}{2}\sin \mathcal{C}\omega_{\mathrm{ex}} t\right) \\ &= \bar{\Omega} S_z + \frac{\chi}{2} S_z \sin \mathcal{C}\omega_{\mathrm{ex}} t \sum_i^N \Omega_i \delta_i.\end{aligned} \tag{7.10}$$

The last term is simply the statistical variance[7] of the spin-cavity couplings $N(\Delta\Omega)^2$. We can then write the cavity shift as

$$\delta\omega(t) = \left(1 + \frac{1}{2}\chi N \frac{(\Delta\Omega)^2}{\bar{\Omega}}\sin \mathcal{C}\omega_{\mathrm{ex}} t\right)\bar{\Omega} S_z = \alpha(t)\bar{\Omega} S_z. \tag{7.11}$$

[7] Note that:

$$\begin{aligned}\sum_i^N \Omega_i \delta_i &= \sum_i^N \delta_i^2 + \bar{\Omega}\sum_i^N \delta_i \\ &= (N-1)\mathrm{Var}\Omega\end{aligned}$$

Considering the Bessel correction for variance. Since $N > 10^4$, we use $N_1 \approx N$ in the text. To agree with the text in [65], we use $(\Delta\Omega)^2$ for this variance.

We find that

$$\begin{aligned}\alpha(t) - 1 &= \frac{\chi N}{2}\frac{(\Delta\Omega)^2}{\bar{\Omega}}\sin\mathcal{C}\omega_{\mathrm{ex}}t \\ &= \frac{n_0(\beta_2+\beta_1)\bar{\Omega}}{2\eta\kappa_t}N\frac{(\Delta\Omega)^2}{\bar{\Omega}}\sin\mathcal{C}\omega_{\mathrm{ex}}t. \end{aligned} \tag{7.12}$$

is the time-dependent amplification factor.

We thus expect an amplification that depends on the atom number, the probe photon number, and, not on the coupling strength, but on the coupling inhomogeneity and that increases for $t \lesssim \pi/(2\mathcal{C}\omega_{\mathrm{ex}})$. While this simplified model predicts an oscillation of $\alpha(t)$, we expect it to damp out for times approaching the lateral collision time scale, as these collisions destroy the correlation between external and internal states.

7.4 Energy-Coupling Relationship

The model also predicts that a correlation should arise between the spin state and motional energy. For example, when M_1 is performed in the blue profile of the cavity, and it yields $S_z > 0$, the ISRE converts the phase shift of colder atoms into an increased probability of being in $|\uparrow\rangle$ and that of hotter atoms into an increased probability of $|\downarrow\rangle$, for times $t < \pi/(\mathcal{C}\omega_{\mathrm{ex}})$.

More quantitatively, we consider the motional energy $E_{t,i}$ of atom i in the transverse directions ($t = y, z$). Ω_i is a monotonically decreasing function of $E_{t,i}$ (see Eq. 7.2), and here we approximate it by $\delta_i \approx -\varepsilon(E_{t,i} - \bar{E}_t)$, where $\bar{E}_t = \frac{1}{N}\sum_i^N E_{t,i} = k_B T$ and ε is a positive constant[8]. It follows that $(\Delta\Omega)^2 \approx \varepsilon^2 \mathrm{Var}\,(E_t) = \varepsilon^2 (k_B T)^2$, so $\varepsilon = \Delta\Omega/k_B T$. Overall, the average energy of $|\uparrow\rangle$ can be written as $E_{t,\uparrow} \approx \frac{1}{N_\uparrow}\sum_i^N P_{\uparrow,i} E_{t,i}$, where $P_{\uparrow,i} = \frac{1}{2} - s_{z,i}$ and $N_\uparrow = \sum_i^N P_{\uparrow,i}$ and similarly for $|\downarrow\rangle$, with $P_{\downarrow,i} = \frac{1}{2} + s_{z,i}$. Note the replacement $s_z \to -s_z$ due the π pulse before in M_2.

The ISRE furthermore correlates $s_{z,i}$ with $E_{t,i}$ through Ω_i. Using Eq. 7.9, after an evolution time t,

$$\begin{aligned} E_{t,\uparrow} &\approx \frac{1}{N_\uparrow}\sum_i^N \left(\frac{1}{2} - s_{z,i}\right)\left(\bar{E}_t - \frac{\delta_i}{\varepsilon}\right) \\ &\approx \frac{\bar{E}_t}{N_\uparrow}\sum_i^N \left(\frac{1}{2} - s_{z,i}\right) + \frac{1}{N_\uparrow}\sum_i^N \left(s_{z,i} - \frac{1}{2}\right)\left(\frac{\delta_i}{\varepsilon}\right) \\ &\approx \frac{\bar{E}_t}{N_\uparrow}\left(\frac{N}{2} - S_z\right) + \frac{1}{\varepsilon N_\uparrow}\sum_i^N s_{z,i}\left(\Omega_i - \bar{\Omega}\right). \end{aligned}$$

Note that the first term in the last summation is simply the cavity shift we derived in equation (7.11) and the second term factors out another factor $\bar{\Omega}$.

$$E_{t,\uparrow} \approx \frac{\bar{E}_t}{N_\uparrow}\left(\frac{N}{2} - S_z\right) + \frac{\bar{E}_t}{\Delta\Omega N_\uparrow}\left(\alpha(t) - 1\right)\bar{\Omega} S_z.$$

The experimentally measured transverse temperature directly links to the average energy as $T_{t,\uparrow(\downarrow)} \approx E_{t,\uparrow(\downarrow)}/k_B$. Furthermore, the first

[8] Both the average value and fluctuation of the energy are derived directly from the Boltzmann distribution

$$f_t(x_t, v_t) \propto \exp\left(\frac{1}{2k_B T}m v_t^2 + \frac{1}{2k_B T}m\omega_t^2 x_t^2\right)$$

Alternatively, one could take the high-temperature limit of the heat capacity of a harmonic oscillator together with the identity $\mathrm{Var}\,(E) = K_B T^2 C$, for canonical ensemble[38].

term is $\bar{E}_t(N_\uparrow/N - 1)$ which tends toward $\bar{E}_t$ for large N as $N_\uparrow \approx N/2$. This leads to

$$T_{t,\uparrow(\downarrow)} \approx T\left(1 \pm 2\left(\frac{\alpha(t)-1}{\Delta\Omega N}\right)\bar{\Omega}S_z\right). \tag{7.13}$$

Thus, we find that the final transverse temperature should correlate with the measured S_z for $0 < t < \pi/(\mathcal{C}\omega_{ex})$. Eq. 7.13 also predicts that the fluctuation $\Delta T_{t,\uparrow(\downarrow)}$ should have a time evolution similar to that of the amplification factor (Eq. 7.12), given the quantum fluctuations $\Delta S_z = \sqrt{N}/2$ of the initial state. Specifically, ignoring other fluctuations in temperature,

$$\Delta T_{t,\uparrow(\downarrow)} \approx \pm T\left(\frac{\alpha(t)-1}{\Delta\Omega\sqrt{N}}\right)\bar{\Omega} \propto \alpha(t) - 1\,. \tag{7.14}$$

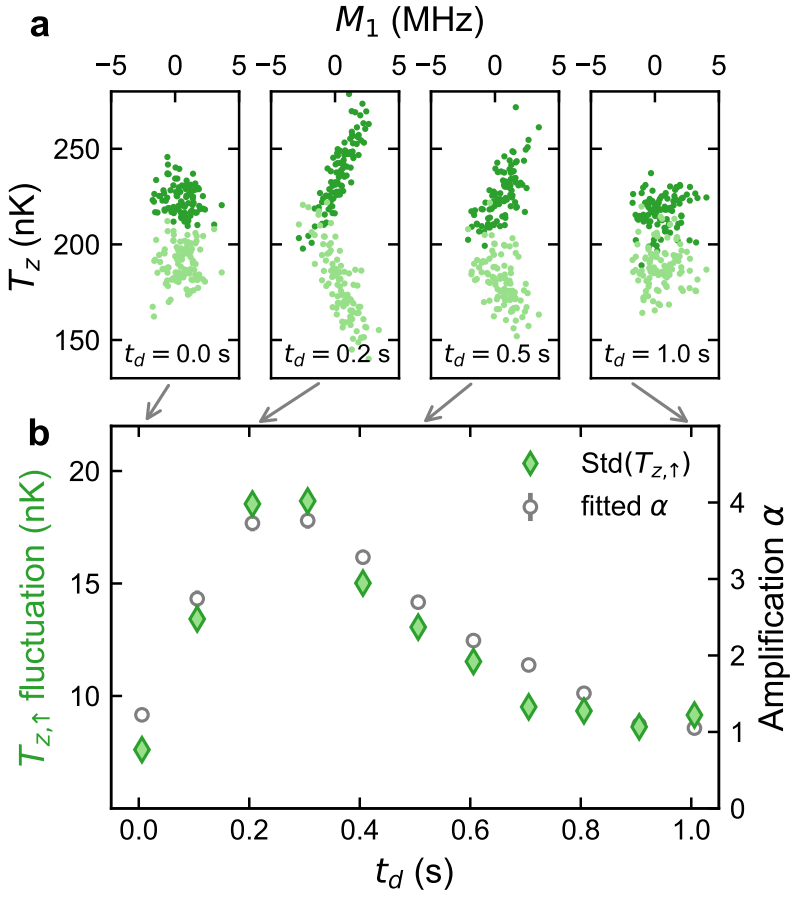

Figure 7.3: The spin-orbit correlation from temperature measurements. a) The temperatures along $\hat{z}$ of states $|\downarrow\rangle$ (light green dots) and $|\uparrow\rangle$ (dark green dots) versus M_1 from the same data set (the offset between the initial temperatures is due to the state-dependent imaging procedure). There is a clear correlation between $T_{z,\uparrow}$ and M_1 (anti-correlation for $|\downarrow\rangle$) for $t_d = 0.2\,\mathrm{s}$ and $0.5\,\mathrm{s}$, where $\alpha > 1$. b) The time evolution of the temperature fluctuations (standard deviation) of $T_{z,\uparrow}$. The evolution closely resembles that of the amplification factor α (open circles, right axis), further corroborating the amplification mechanism described in the text. Figure retrieved from [65]

The time-of-flight imaging yields state-resolved temperatures $T_\uparrow$ and $T_\downarrow$ for every shot, providing an experimental test for this mechanism. If $s_{z,i}$ is correlated with Ω_i and hence with the motional energy as outlined above, then the temperatures of the two spin components should be correlated with M_1, and the correlation should have opposite signs for the two states. Indeed, when $T_\uparrow$ and $T_\downarrow$ are plotted against M_1 [Fig. 7.3(a)], a correlation is clearly visible for times t_d where $\alpha > 1$ and has the expected sign: the higher the measured S_z

in M_1, the lower is $T_\downarrow$ (taking into account the base change (π pulse) in M_2) and the higher is $T_\uparrow$. The amount of temperature change also depends on α in the expected manner, as can be seen by plotting the shot-to-shot temperature fluctuations (standard deviation ΔT_z) as a function of t_d [Fig. 7.3(b), green diamonds]. For short times where $\alpha \sim 1$, fluctuations are very low, limited by measurement noise. As α increases, they rise up to approximately 18 nK, and their time evolution closely follows that of α for our measurement time.

A semiclassical Monte Carlo simulation where atoms move on classical trajectories and evolve under mean-field spin exchange equation reproduces the time evolution of the amplification factor quite well, as shown in figure 7.4. The simulation includes a damping rate that is estimated from the decay rate of centre-of-mass oscillations mostly induced by the cavity-locking light. The quantitative agreement is satisfactory despite the simplicity of the model and the fact that the simulations do not consider quantum correlations.

The observed temperature correlation and the simulation results thus provide strong evidence for the amplification effect resulting from the inhomogeneous measurement-induced phase shift combined with spin exchange interaction acting on the squeezed state on the long-time scales explored here for the first time. This is in contrast to the non-interacting case usually considered, where differences in atom-cavity coupling merely reduce the effective atom number [46] and a small dephasing does not affect the measurement as it remains confined to an axis that is not observed. Also note the difference with respect to "quantum phase magnification" effects [121, 122]: while in these effects, interactions modify the spin state itself, here it is the correlations between the spin and motional degrees of freedom that are modified and lead to the observed amplification.

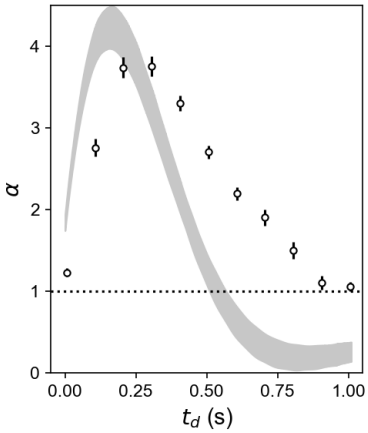

Figure 7.4: Amplification factor as a function of time with Montecarlo simulation. An additional dampening term related to the centre-of-mass residual oscillations is included.

7.5 A model for noise under amplification

From the qualitative understanding of the amplification mechanism outlined in the main text and supported by the temperature correlation with M_1 (Fig. 7.3), we can formulate a simple phenomenological model of the time evolution of the cavity measurement. We start by formulating the time evolution of S_z given a measurement M_1 as:

$$S_z(t)|_{M_1} = e^{-\gamma_{1b}t} S_z(0)|_{M_1} + \delta S_z(t)\,, \tag{7.15}$$

where $S_z(0)|_{M_1}$ follows the conditional probability distribution of S_z after M_1, i.e., approximately a normal distribution centred around $M_1/\bar{\Omega}$ with a variance given[9] by $\mathrm{Var}\left(\delta M_1^n\right)/\bar{\Omega}^2$. $\delta S_z(t)$ represents all spin noise occurring after M_1 (such as the loss-induced noise [71]); $e^{-\gamma_{1b}t}$ accounts for the reduction of the spin $\langle S_z \rangle$ due to one-body loss. The spin variance is thus given by

$$\Delta^2 S_z(t)|_{M_1} = e^{-2\gamma_{1b}t}\mathrm{Var}\left(\delta M_1^{\mathrm{n}}\right)/\bar{\Omega}^2 + \mathrm{Var}\left(\delta S_z(t)\right)\,. \tag{7.16}$$

[9] We use δM_l^{n} to represent the noise of measurement $l = 1,2$ which is much lower than atomic projection noise, and the lower bound of which is given by photon shot noise $\mathrm{Var}\left(\delta M_l^n\right) \geq (\Delta\, M_l|_{\mathrm{PSN}})^2$.

On the other hand, we expect M_2 to follow a statistical distribution given by

$$M_2(t) = \bar{\Omega}\left[\alpha(t) S_z(0)|_{M_1} + \delta S_z(t)\right] + \delta M_2^{\mathrm{n}}\,, \tag{7.17}$$

where $\alpha = \alpha' e^{-\gamma_{1b} t}$ includes both the pure amplification effect α' and the reduction of the spin $\langle S_z \rangle$ due to one-body loss. Note that the amplification mechanism acts on the phase correlation imprinted in M_1 but does not modify the cavity coupling of the spins.

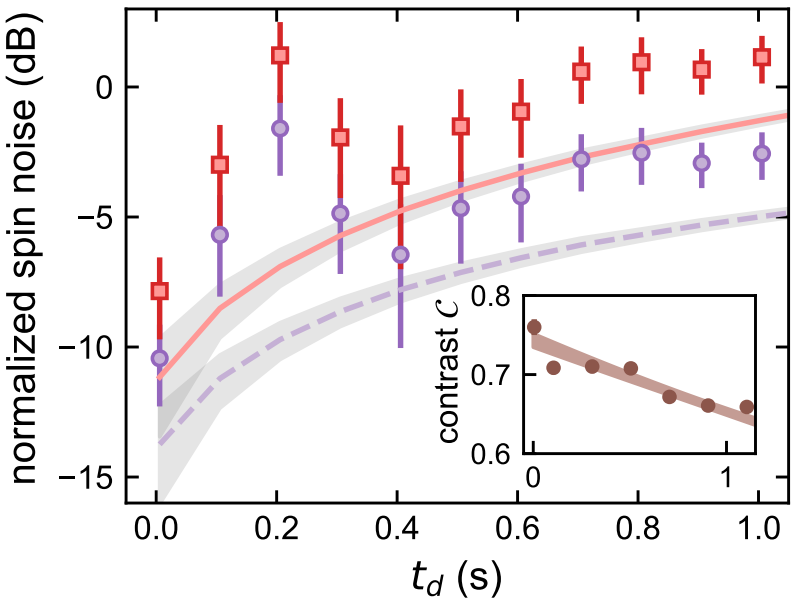

Figure 7.5: Inferred squeezing in the spin degree of freedom. The purple circles show the inferred upper limit of the number squeezing in the spin degree of freedom (Eq. 7.20). The evolution is consistent with the theoretical lower bound given by atom loss (dashed curve). The red squares show the resulting metrological squeezing, obtained as usual by dividing the number squeezing by the measured Ramsey contrast shown in the inset. For comparison, the solid curve is the theoretical limit normalized to the fit of the experimental Ramsey contrast. The inset shows the Ramsey contrast data (circles) as a function of t_d and their exponential fit (shaded curve), which yields $\tau = 7.7(6)$ s. Figure retrieved from [65].

To infer $\Delta^2 S_z(t)|_{M_1}$ from our cavity measurements M_1 and M_2, we use the minimum conditional variance as in Eq. 6.1 ($\zeta = \alpha$ minimizes the variance). Assuming the three contributions in Eq. 7.17 to be statistically independent, we have

$$\begin{aligned}\mathrm{Var}\left(M_2 - \alpha M_1\right) = \\ \alpha^2 \mathrm{Var}\left(\delta M_1^{\mathrm{n}}\right) + \bar{\Omega}^2 \mathrm{Var}\left(\delta S_z(t)\right) + \mathrm{Var}\left(\delta M_2^{\mathrm{n}}\right).\end{aligned} \tag{7.18}$$

Note that we dropped the time dependence for convenience. We find that this variance does contain information about $\mathrm{Var}\left(\delta S_z(t)\right)$ but it is affected by the noise of M_1 amplified by α (first term on the right-hand side).

Nevertheless, knowing $\alpha(t)$ from our data allows us to infer the actual spin noise $\Delta^2 S_z(t)\big|_{M_1}$ (Eq. 7.16, i.e., the correlation only in the spin degree of freedom rather than the combined spin-orbit observable seen by M_2) by comparing it with Eq. 7.18:

$$\begin{aligned}\Delta^2 S_z(t)\Big|_{M_1} = \bar{\Omega}^{-2}[\mathrm{Var}\left(M_2(t) - \alpha(t) M_1\right) \\ - (\alpha(t)^2 - e^{-2\gamma_{1b} t})\mathrm{Var}\left(\delta M_1^{\mathrm{n}}\right) - \mathrm{Var}\left(\delta M_2^{\mathrm{n}}\right)].\end{aligned} \tag{7.19}$$

Taking a conservative limit by assuming the minimum PSN from the

cavity measurements, we obtain Eq. 7.20.

$$\Delta^2 S_z(t)|_{M_1} = \Omega_e^{-2}[\mathrm{Var}\,(M_2 - \alpha M_1) - (\alpha^2 - e^{-2\gamma_{1b}t})(\Delta M_1^{\mathrm{PSN}})^2 - (\Delta M_2^{\mathrm{PSN}})^2], \tag{7.20}$$

where we drop the time dependence of α and M_2 for simplicity, and the only noise we subtract is the PSN, $\Delta^2 M_l^{\mathrm{PSN}}$. We find that the contribution from the noise of M_1 (second term in the square brackets) is also affected by the amplification mechanism (α^2), and the exponential comes from the decay of the total spin.

7.5.1 *Lower bound of conditional variance*

To get a lower bound on this quantity, we can identify the term $\delta S_z(t)$ in equation (7.16) with the uncorrelated one-body losses shown in equation (2.17) and bound δM_2^n with PSN:

$$\mathrm{Var}\,(\alpha M_1 - M_2) \geq \alpha^2(\Delta M_1^{\mathrm{PSN}})^2 + (\Delta M_2^{\mathrm{PSN}})^2 + \frac{\bar{\Omega}^2 N}{4}(1 - e^{-\gamma_{1b}t}), \tag{7.21}$$

or in terms of the inferred spin variance:

$$\Delta^2 S_z(t)|_{M_1} \geq e^{-2\gamma_{1b}t}(\Delta M_1^{\mathrm{PSN}})^2 + \frac{\bar{\Omega}^2 N}{4}(1 - e^{-\gamma_{1b}t}). \tag{7.22}$$

The upper limit we calculate from only subtracting PSN (purple circles in Fig. 7.5) approaches the lower limit due to losses (dashed line in Fig. 7.5) to within 3 dB, except in the time interval where α is significantly larger than 1. The larger difference at those times may come from fluctuation in the amplification dynamics themselves.

We also plot the metrological squeezing factor by combining these data with the independently measured coherence as a function of time (Fig. 7.5, inset). The inferred metrological squeezing remains below 0 dB up to 600 ms. This is about 2 orders of magnitude longer than in previous squeezing experiments with cold alkali atoms and compatible with the typical interrogation time for primary-standard atomic clocks.

The next steps in our experiment will be to devise more symmetric measurement pulse schemes as discussed in Sec. 9.1, and to implement the real-time feedback that allows measurement-based squeezing to be integrated into the full Ramsey-measurement cycle.

7.5.2 *Noise amplification*

Combining the effects of one-body losses and amplification, we arrive at a noise model that looks like equation (7.21), while the actual spin variance behaves as expected from (2.19). We can interpret this as the amplification restricting our ability to know the actual spin state, not due to a degradation of the spin itself but due to the change of effective coupling inside the cavity. This can be appreciated even in our squeezing measurements of section 6.2 as shown in figure 7.6.

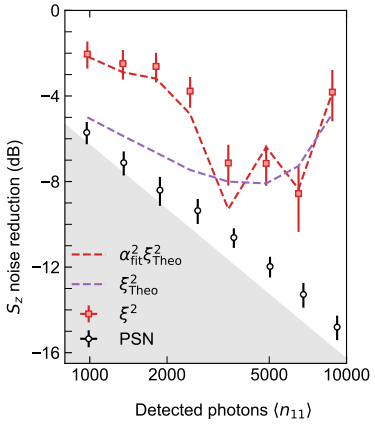

Figure 7.6: Squeezing and amplification. Same data of figure 6.4. The dash purple curve shows the theoretical curve from equation (2.19). The red dashed curve shows the same noise label scale by α^2 as derived from a simple linear regression between M_1 and M_2.

The presence of amplification reduces the squeezing we inferred by up to 3.5 dB at 1800 photons detected per probe with respect to the level expected from 1-body losses and PSN. Moreover, we notice a 1σ improvement for 6500 photons, the optimal level we measured, with respect to the theoretical curve. We notice that $\alpha \approx 0.89$ for this particular value. This means that α could both increase or decrease the conditional variance $\mathrm{Var}\,(M_2|M_1)$ depending on whether $\alpha > 1$ or $\alpha < 1$, respectively. We will study the significance of this in the final part of the manuscript.

Part IV

Clock Operation

8

Effect of Amplification on the Local Oscillator Phase Measurement

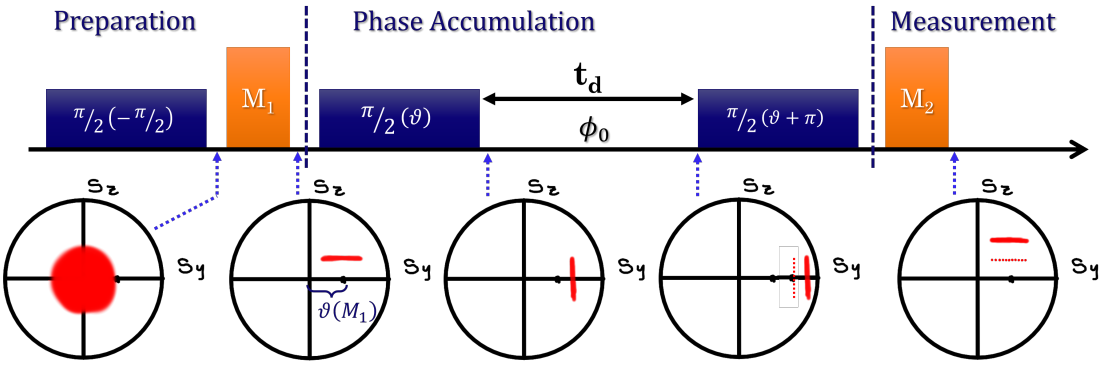

Figure 8.1: We can distinguish three main moments of a sequence cycle. First, a state preparation in which a superposition and measurement are used to generate the squeezed state. This first part would be absent in a classically operated clock. The second part corresponds to the actual interferometer in which a phase accumulation begins; a first pulse orients the state properly to the accumulated phase, and a second one brings back the state so that the accumulated phase can be detected a population difference. A third part corresponds to the state measurement, which could be both a cavity or a camera measurement.

Now that we have convinced ourselves of the presence of squeezing, we would like to use our states to measure phase accumulation in a Ramsey sequence. As described in section 1.3.2, a Ramsey interferometer is an interrogation scheme composed by a *starting* pulse to the atomic ensemble into the equator of Bloch Sphere, followed by a phase accumulation period and a *closing* pulse to transfer the accumulated phase into a population difference to be ultimately measured. In the case of a squeezed state, there are two relevant caveats to consider. The first one is that we should orient our state adequately so that the squeezed component is in the direction of the phase accumulation through a rotation of the Bloch sphere. A second point to consider is the fact that the position of our state depends on the results of the first measurement in a two-fold way. Firstly, due to the nature of conditional squeezing, the z component of the spin state is determined by M_1. Secondly, a global phase is imprinted on the state by the light shift caused by the probe. The echo protocol partially corrects for this shift; however, since the number of photons in both probe pulses forming M_1 differs by an amount proportional to S_z, this global phase itself depends on M_1.

8.1 Ramsey Sequence with Conditionally Squeezed States

We now propose the following protocol to measure a phase ϕ_0, depicted in figure 8.1:

1. We start with a preparation stage where a $\frac{\hat{\pi}}{2}(-\pi/2)$ pulse brings the state to the equator of the Bloch sphere.

2. Immediately after, a composite measurement M_1 squeezes our state. Based on the result of M_1, the phase shift on the state is estimated by $\vartheta = \phi_d(n_{1,2} - n_{1,1})$ from an independent calibration of ϕ_d as described in section 6.1.

3. After calculation, a $\frac{\hat{\pi}}{2}(\vartheta)$ pulse is applied, bringing the state to the equator and in the proper orientation to begin the phase accumulation[1].

4. The state is left to evolve during a time t_d where a phase ϕ_0 is accumulated

5. After accumulation, another pulse $\frac{\hat{\pi}}{2}(\vartheta + \pi)$ reverts the previous one. For this configuration, if $\phi_0 = 0$ our state will be at the same place it was after M_1; else, it will be shifted in S_z.

6. Finally, a second cavity measurement M_2 checks the final state and the absorption imaging follows right after for verification.

[1] Both the calculation of the global phase ϑ and the instruction for the DDS that generates the RF pulse are performed with the Teensy microprocessor described in subsection 3.4.2

How would the result of this interrogation look? We claimed that the amplification comes from the spin distribution around its mean and not from the actual value of the mean itself; thus, we expect the phase accumulation to happen "as usual". Considering equation (7.17), we can attribute the phase accumulation part of M_2 to the $\delta S_z(t)$ term.

More precisely, we pose that the cavity shift $\delta\omega_1$ before the start of the interferometer relates to the shift $\delta\omega_2$ at the end of the sequence by the expression:

$$\delta\omega_2 = \alpha\delta\omega_1 + f(\phi_0) + \epsilon_{1b}, \tag{8.1}$$

$$f(\phi_0) = \frac{\mathcal{C}N\bar{\Omega}}{2}\sin(\phi_0), \tag{8.2}$$

where ϵ_{1b} is the contribution due to uncorrelated losses and technical noise, bounded from below by one-body losses, and α is the amplification factor that would only affect the contribution coming from M_1, but not the actual displacement form the phase accumulation. In practice, for a fixed atom number, identical interrogations in the first measurement, *i.e.*, the same average photon number per probe, and the same separation between the two measurements, we expect the same amplification α to be seen as predicted by equation (7.12). For two different values of ϕ_0, repeated measurements of $\delta\omega_2$ vs $\delta\omega_1$ would be accumulated around two lines shifted by $f(\phi)$ as depicted in figure 8.2. Given a measurement (M_1, M_2) of $(\delta\omega_1, \delta\omega_2)$, the uncertainty to distinguish two values of ϕ_0 is given by the spread of an

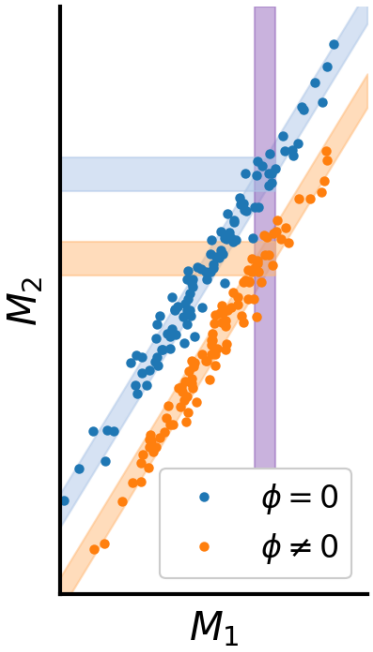

Figure 8.2: Simulated data for the phase measurement of two values of phase. The amplification factor is fixed for a fixed number of atoms at the same temperature and a fixed delay between measurements. The combination of M_1 and M_2 allows us to assign a phase value to the cycle, and our uncertainty is given by how much our data points spread around the corresponding line for a given phase value.

ensemble of measurements around the corresponding line (blue and orange shading respectively on figure 8.2), this itself is the same as the uncertainty for predicting M_2 given M_1 for fixed α and ϕ_0. The comparison between this width and the one associated with QPN is the metrological gain due to our scheme.

8.2 Phase shift inference

The inferred cavity shift can only be known up to photon shot noise. For the rest of this section, we refer to the measured cavity shift as M_1 for the first cavity measurement and M_2 for the second one. More simply:

$$M_1|\delta\omega_1 \sim \mathcal{N}(\delta\omega_1, \sigma_1^2), \qquad M_2|\delta\omega_2 \sim \mathcal{N}(\delta\omega_2, \sigma_2^2), \tag{8.3}$$

where σ_1 and σ_2 are the noise associated to photon shot noise for M_1 and M_2 and they are similar for identical[2] measurements M_1, M_2. The first measurement, if well prepared on the equator, should correspond to a random variable around zero with a spread given by the QPN

$$\delta\omega_1 \sim \mathcal{N}(0, \sigma^2_{\text{QPN}}), \tag{8.4}$$

where $\sigma^2_{\text{QPN}} = \frac{N}{4}\Omega^2$. The atom losses during the phase accumulation will affect the second measurement. As shown in section 2.3.3, for a state with initial variance $\Delta S_z(0)$ of the z-component of spin, one can describe the one-body losses of the spin state as

$$\Delta S_z^2(t) = \Delta S_z^2(0)\, e^{-2\gamma_{1b}t} + \frac{\langle N(t)\rangle}{4}\left(1 - e^{-\gamma_{1b}t}\right). \tag{8.5}$$

The exponential decay due to the reduction of the length of spin can be included in α, scaling the expression we obtained in equation (7.12) by $e^{-\gamma_{1b}t}$, while we assign the uncorrelated losses to ϵ_{1b} as:

$$\epsilon_{1-\text{b}} \sim \mathcal{N}(0, \sigma^2_{1\text{b}}), \tag{8.6}$$

$$\sigma^2_{1\text{b}} = \bar{\Omega}^2 \frac{\langle N(t)\rangle}{4}\left(1 - e^{-\gamma_{1b}t}\right). \tag{8.7}$$

We would like to answer two questions about this scheme. First, given an ensemble of measurements, what's the best calibration for α that we can get? And secondly, given a pair of measurements M_1, M_2, what is the best guess we can have on φ and the uncertainty associated to this inference? The complete model for the sampled data is then given by:

$$P(M_1, M_2, \delta\omega_1, \delta\omega_2; \alpha, f) = P(M_1, M_2|\delta\omega_1, \delta\omega_2; \alpha, f) \tag{8.8}$$

$$\times\, P(\delta\omega_2|\delta\omega_1; \alpha, f) P(\delta\omega_1). \tag{8.9}$$

Where, by construction, $P(\delta\omega_1; \alpha, f) = P(\delta\omega_1)$. It follows immediately that:

$$P(\delta\omega_1, \delta\omega_2; \alpha, f|M_1, M_2) = \frac{P(M_1, M_2|\delta\omega_1, \delta\omega_2; \alpha, f) P(\delta\omega_2|\delta\omega_1; \alpha, f) P(\delta\omega_1)}{P(M_1, M_2)}$$

$$P(\delta\omega_1, \delta\omega_2; \alpha, f|M_1, M_2) \propto P(M_1|\delta\omega_1) P(M_2|\delta\omega_2) P(\delta\omega_2|\delta\omega_1; \alpha, f) P(\delta\omega_1).$$

[2] Notice that this is not always the case. Recently, we opted for increasing the number of photons used in M_2 since after the phase accumulation, we do not care about preventing the dephasing of the spins, allowing for a stronger second measurement

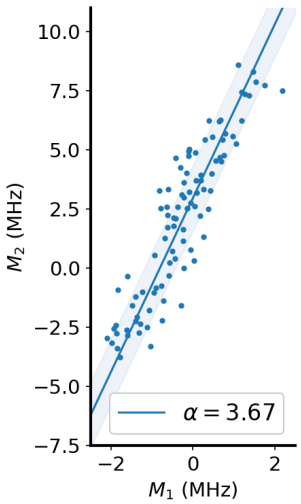

Figure 8.3: Measured data for phase measurement. The amplification factor is fixed for a fixed number of atoms at the same temperature and a fixed delay between measurements. The combination of M_1 and M_2 allows us to assign a phase value to the cycle, and our uncertainty is given by how much our data points spread around the corresponding line for a given phase value. The shading in this case shows $\pm\sqrt{\text{Var}\,(M_2|M_1)}$.

One can show (see 11.2) that the Maximum Likelihood parameters α, φ for an ensemble of N points are given by

$$f(\phi) = \langle M_2 \rangle - \frac{\alpha \langle M_1 \rangle}{1 + \frac{\sigma_1^2}{\sigma_{\mathrm{QPN}}^2}}, \tag{8.10}$$

$$\alpha = \frac{\mathrm{Cov}(M_1, M_2)}{\sigma_{\mathrm{QPN}}^2}. \tag{8.11}$$

In practice, we would use a large number of interrogation cycles to give a proper calibration of α, then, for a fixed α, the inference of $f(\phi)$ can be done using equation (8.10). The limit on the precision of this inference can be obtained from the calibration set itself as:

$$\begin{aligned} \mathrm{Var}\left(\tilde{f}(\phi_0)\right) &= \mathrm{Var}\left(M_2 - \frac{\alpha M_1}{1 + \frac{\sigma_1^2}{\sigma_{\mathrm{QPN}}^2}}\right) \\ &= \mathrm{Var}(M_2) - \frac{\mathrm{Cov}(M_1, M_2)^2}{\mathrm{Var}(M_1)} = \mathrm{Var}(M_2|M_1). \end{aligned} \tag{8.12}$$

This itself is limited by the Cramer-Rao bound [40], derived in the appendix 11.2 as well:

$$(\delta f)^2 \geq \sigma_2^2 + \sigma_{1\mathrm{b}}^2 + \alpha^2 \frac{\sigma_1^2 \sigma_{\mathrm{QPN}}^2}{\left(\sigma_{\mathrm{QPN}}^2 + \sigma_1^2\right)}. \tag{8.13}$$

Here, the first two noise contributions are from the technical noise of detecting M_2 due to one-body losses and PSN. The third term is the conditional variance from updating a prior gaussian distribution with variance σ_{QPN}^2 with a measurement of resolution σ_1, as we did in section 2.2, with the resulting noise amplified by α. Figure 8.3 shows an example of the protocol described in the previous section for an ensemble of 100 points. The straight line comes from the ML estimator, and the blue shading marks the conditional variance as defined by equation (8.12).

8.3 First Phase Measurement

We would like to verify that the phase accumulation is undisturbed by the presence of interactions giving rise to the amplification. To do so, we can scan the phase of the pulse closing the interferometer sequence detailed in figure 8.1. This is, instead of closing with a pulse $\frac{\hat{\pi}}{2}(\pi + \vartheta)$, we send a pulse $\frac{\hat{\pi}}{2}(\pi + \vartheta - \phi)$. For a small ϕ, this would simply shift the lines as in figure 8.2 corresponding to a phase $\phi_0 + \phi$. This will allow us to assign a value of phase to each of the curves that can later be used as a reference.

8.3.1 Experimental Sequence

The sequence follows the same preparation protocol as the squeezing measurements, with the same magnetic trap geometry we described

in section 6.2.1. We implement the sequence shown in figure 8.1. An ensemble of $N \sim 1.9 \times 10^4$ ^{87}Rb atoms are magnetically trapped. We start with all atoms in $|\downarrow\rangle$ and apply a $\frac{\tilde{\pi}}{2}\left(-\frac{\pi}{2}\right)$ pulse on the clock transition to prepare a CSS on the equator of the Bloch sphere. This sequence's calibration has the three $\pi/2$ pulses being 60 ms of duration, while the composite π pulses used during the composite measurements are 26.55 ms. A composite cavity measurement M_1 measures $n_{1,1}, n_{1,2}$ photons from which we infer the initial cavity detuning, squeezing the state. Immediately after, a $\frac{\tilde{\pi}}{2}(\vartheta)$ MW+RF pulse turns the squeezed quadrature of the state in the direction of phase accumulation. Here $\vartheta = \phi_d(n_{1,2} - n_{1,2})$ is the average uncompensated phase shift with ϕ_d being the phase shift induced per detected photon as calibrated from the previous section 6.1.2.

After a 5 ms delay, a third pulse $\frac{\tilde{\pi}}{2}(\vartheta + \pi - \phi)$ brings the squeezed quadrature towards the population difference direction and a second identical composite measurement is performed. Finally, $N_\uparrow$, $N_\downarrow$ is measured by absorption imaging after a 2.5 ms TOF for $|\uparrow\rangle$ and 5 ms for $|\downarrow\rangle$. After imaging, the stripline is turned on again so that the cavity lock is maintained, and two light pulses with the same power are sent on both sides of the cavity profile to use as a reference for the cavity shift as described in section 5.2.1. We tried 5 different values of phase $\phi = 0, 2, 4, 6, 8°$. We leave ϕ fixed for 100 sequence cycles before changing to the following value. The four pulses forming the two composite cavity measurements have identical average photon numbers $\langle n_{1,1}\rangle = \langle n_{1,2}\rangle = 5.1(8) \times 10^3$ having a duration of 8.85 ms each corresponding with the period of transversal oscillations in the trap. Considering the length of the $\pi/2$ pulses, the separation between the cavity measurements is 125 ms, and we thus expect the amplification to be close to the maximum, as we observed in figure 6.5.

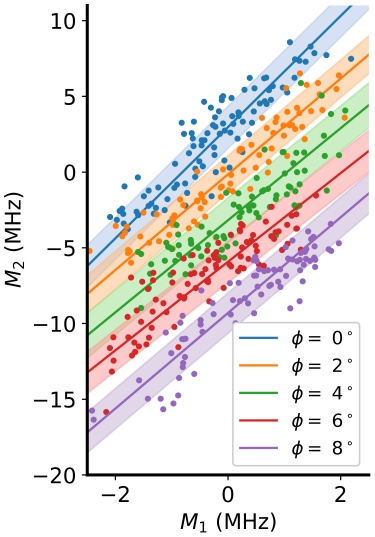

Figure 8.4: Ensemble of data for phase measurement and calibration. Each colour corresponds to a different ϕ value with a fixed number of atoms and measurement strength on the blue side of the cavity profile. The delay between composite measurements is fixed at 125 ms. The shading, in this case, shows $\pm\sqrt{\mathrm{Var}\,(M_2|M_1)}$ around the corresponding line.

8.3.2 *Amplification Stability and Phase Inference*

In figure 8.4, we can see the ensemble of measurements for the different values of ϕ; as we expected from our model, the correlation between M_1 and M_2 is maintained similarly to what we would have expected from an amplification measurement. We are left to evaluate if α is stable enough and to associate a phase value to each of the M_2-intersects. We perform a bootstrap analysis with 10^3 resamplings of the same size as the original data; the resulting average α and with error bars from statistical standard deviation are shown in figure 8.5. For $\phi > 0$, the inferred amplification factors are identical within statistical error bars. The amplification factor for $\phi = 0°$ seems to be larger than the rest. Verifying the raw experimental data, we can see that the photon number measured for $\phi = 0°$ is 2% larger than that of the rest of the sequences[3] corresponding to almost twice PSN, however, according to our model (see equation (7.12)), this is not enough to account for an increase in α. The difference falls within 1-σ of the statistical resolution corresponding to a p-value of 0.33; we

[3] This could be due to thermal fluctuations before stabilisation after some sequence cycles from both the lock or the AOM used as interrupters.

treat them as equal for all practical purposes.

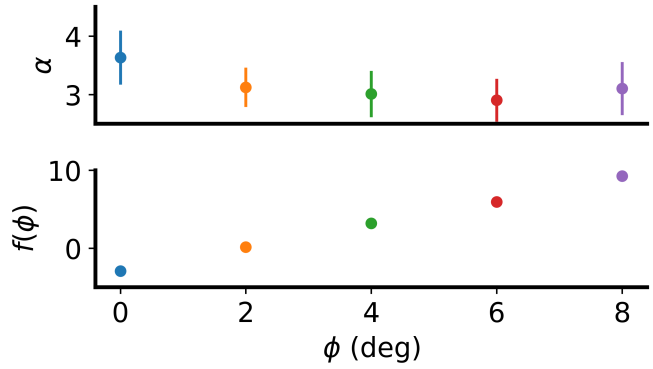

Figure 8.5: Amplification factor and intersect $f(\phi)$. Error bars obtained from bootstrapping with 1000 resampling.

Phase inference from camera. We first verify that the phase accumulation occurred as expected from the camera data so that we can ignore any amplification effect in the probe. Figure 8.6 a) shows the average z component, $S_z = \frac{1}{2}(N_\uparrow - N_\downarrow)$ along the 100 repetitions for each value of ϕ as obtained from the camera. Error bars are obtained directly from the sample standard deviation of the camera data. We observe an excess of noise from QPN, depicted in the coloured shading since this is unconditional data and the camera itself is limited in resolution close to QPN.

From the camera data we can infer the phase ϕ_0 accumulated during t_d and the applied ϕ from the closing pulse as:

$$\tilde{\phi} + \tilde{\phi}_0|_{\text{cam}} = \arcsin\left(\frac{1}{\mathcal{C}_{\text{cam}}}\frac{N_\uparrow - N_\downarrow}{N_\uparrow + N_\downarrow}\right), \tag{8.14}$$

where the contrast $\mathcal{C}_{\text{cam}}$ is obtained from the fit presented in section 5.3, considering the contrast reduction due to the total photon number detected n_1, n_2 in the two-cavity measurement preceding the imaging, *i.e.*, $\mathcal{C}_{\text{cam}} = \mathcal{C}(n_1)\mathcal{C}(n_2)$. Results are shown with squares in figure 8.6 b), a linear fit between the applied ϕ and the inferred phase is shown in the red dashed line, compatible with our idea that the amplification does not affect the direction of the overall spin.

Phase inference from cavity. Once convinced that the phase accumulation happens as expected, we can use this information to measure the phase shift from the cavity shift adequately. For a fixed α that we obtained from equation (8.11), we can deduce[4] the phase associated to a particular data point (M_1, M_2) by projecting it back to the M_2-axis via the formula

$$\tilde{f}(\phi) = M_2 - \alpha\frac{M_1}{1 + \frac{\sigma^2_{\text{PSN}}}{\sigma^2_{\text{QPN}}}}.$$

From $\tilde{f}$, we can recover the $\phi + \phi_0$ as:

$$\tilde{\phi} + \tilde{\phi}_0|_{\text{cav}} = \arcsin\left(\frac{2}{\mathcal{C}N\bar{\Omega}}\tilde{f}(\phi)\right), \tag{8.15}$$

[4] For the following, the tilde above a quantity $\tilde{X}$ marks the inference of a quantity X

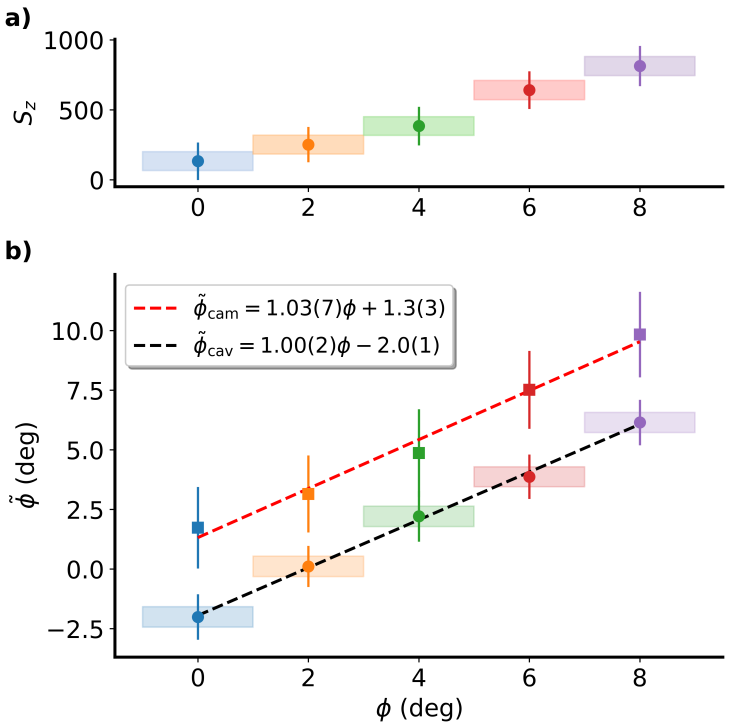

Figure 8.6: a) Average $S_z = \frac{1}{2}(N_\uparrow - N_\downarrow)$ component as calculated from the camera data for each value of ϕ applied. Error bars are the standard deviation, and shading shown is the QPN from the camera as $\sqrt{N}/2$. b) Comparison between the inferred phase $\tilde{\phi}$ and the phase ϕ applied to the closing pulse of the interferometer. Coloured dots and error bars correspond to data acquired from the cavity detection with an adjusted contrast of $\mathcal{C} = 0.575(1)$. Error bars marked the conditional standard deviation $\sqrt{\mathrm{Var}(M_2|M_1)}$ from bootstrapping. Shading marks the $\pm\frac{1}{\sqrt{N}}$ as the limit of QPN for phase. The dashed black line is a simple linear fit between the inference $\tilde{\phi}_0$ from the cavity and the applied ϕ. The coloured squared is inferred from the absorption imaging. The red dashed line is a simple linear fit between the inference $\tilde{\phi}_0$ from the camera and the applied ϕ.

where $\mathcal{C} = 0.575(1)$ is obtained from a least-square fit on the model described by equation (8.15) and the applied ϕ to the closing pulse, figure 8.6 shows the results of such treatment, we have used our $\bar{\Omega} = 16.3$ kHz as in our previous calibrations, and N is obtained from the camera. We notice that the accumulation does follow a direct relation as $\tilde{\phi}_{cav} = 1.00(2)\phi - 2.0(1)^\circ$. This tells us that we can use this scheme to measure a phase with the appropriate calibration of the contrast.

Effect of amplification on noise. Knowing the average phase is not enough to justify the scheme's use. In figure 8.6 b), we have included the shading corresponding to QPN, *i.e.*, $\pm\frac{1}{\sqrt{N}}$. The uncertainty on ϕ exceeds QPN by a factor of at least 4.1 in variance for the best case. We obtained an improvement with respect to the camera measurements, but the limit on the resolution of the absorption imaging itself could account for this. A reason for this excess was discussed in section 7.5 and can be seen directly from the Cramer-Rao bound in equation (8.13). The amplification we observe does not affect how the atomic state accumulates the phase. However, it does amplify the noise associated with the first measurement. Consider figure 8.4: the uncertainty on the phase measurement is directly related to our ability to distinguish between the different lines accounting for different values of ϕ. This distinguishability comes from the spread of the points around the corresponding line. As α increases, the line is stretched vertically, increasing the spread and thus reducing the distinguishability between the lines.

9
Amplification Control

We concluded chapter 8 with the claim that the effect of the amplification factor was not on phase accumulation by the atomic state but on its noise distribution. We also claimed that, as our measurement M_2 is amplified, we lose the ability to distinguish different values of phase. In this chapter we study two approches to control and reduce the amplification effect: modifying the detuning of the probe pulse with respect to the cvity resonance and reducing the number of atoms.

The first three sections of this chapter describe the effect of changing the detuning of the the probe beam with respect to the cavity resonance. First we tried using a red-detuned probe to invert the relationship between the measured S_z and the inhomogeneous lightshift induced by the probe. We then study the effect of combining both red and blue detuned probes in effort to eliminated the effect completely. In section 9.4, we reduced the number of atoms in the cavity to decrease both the rate of collisions and some of the statistical terms that appear in equation (7.12). Finally, in section 9.5 we combine both approaches in a phase-measurement procotol, as descrebed in chapter 8 and show some preliminary results on phase measurements below QPN.

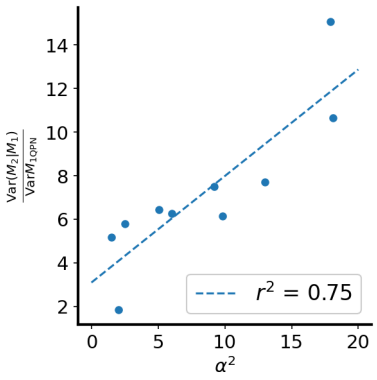

Figure 9.1: Comparison between the conditional variance with respect to PSN as a function of α^2 for the first 900 ms for the sequence shown in figure 6.5. A strong correlation can be seen between the measured noise and the amplification factor α ($r^2 = 0.75$)

9.1 Influence of Probing Scheme in Amplification

To connvince uouselves that the amplification of our measurement streches the noise distriution contidion on M_1, we refer back to the data we presented at the end of chapter 6. In figure 9.1, we plotted the conditional variance, *i.e.*, the vertical extension as a function of α^2 for the data[1] in figure 6.5. This indicates that for us to be able to use the squeezing generated via QND, we need to reduce or eliminate the amplification. This is the objective of this chapter.

We have seen in section 7.3 that the composite measurement M_1 imprints a global phase $\bar{\phi}$ due to the probe light shift as given by equation 7.7. This lightshift can be corrected by an adequate choice of phase of the following pulses as we have done in chapter 8. However, there is also a residual phase shift distribution due to the inho-

[1] We only included the first 900 ms to neglect any effect due to lateral collisions

mogeneous coupling given by

$$\Delta\phi_i = \chi\delta_i S_z, \tag{9.1}$$

where the $\delta_i = \Omega_i - \bar{\Omega}$ is the deviation of the atom's coupling to the cavity with respect to the average of the ensemble and $\chi = \frac{n_0}{\eta\kappa_t}(\beta_2 + \beta_1)\bar{\Omega}$. This inhomogeneous shift, in our model, gives rise to the amplification factor as:

$$\alpha(t) = (1 + \chi f(t))\, e^{-\gamma_{1b}t}, \tag{9.2}$$

with the additional exponential dampening included to account for the reduction of the spin size due to 1-body losses[2]. So far, $\chi > 0$ since we have been probing the blue side of the cavity profile, such that $\beta > 0$. If we were to probe the red side of the cavity profile, we would be able to revert the sign of β and thus the sign of χ, leading to a *de-amplification*; we refer to this as *Red Probing*. Moreover, if the two probe pulses used in M_1 were to be applied on opposite sides of the cavity profile, the average number of photons in both would be the same within PSN, leading not only to a better compensation of the global shift $\bar{\phi}$, but also a reduction of on the left inhomogeneous phase shift. We now test both hypotheses.

[2] One could also include an additional dampening term to account for the lateral collisions and other effects as the dampening of the centre-of-mass oscillations as mentioned in [65], but this is not necessary for the discussion in this section.

9.2 Red probing

Consider a protocol like the one we followed in section 6.2.1. An ensemble of $N \sim 1.8(2) \times 10^4$ ^{87}Rb atoms is magnetically trapped. We start with all atoms in $|\downarrow\rangle$ and apply a $\pi/2$ pulse on the clock transition to prepare a CSS on the equator of the Bloch sphere. A composite cavity measurement M_1 measures the cavity detuning to determine S_z. This time, the two probe pulses are red-detuned by 20 MHz with respect to the cavity resonance having $\langle n_{11}\rangle = \langle n_{12}\rangle = 6.4(1) \times 10^3$ photons. The cavity shift $\delta\omega_1$ is deduced from the cavity shifts $\delta\omega_\pm$ of the two probe pulses as $\delta\omega_1 \equiv (\delta\omega_+ - \delta\omega_-)/2$. Then, after a delay t_d, a second identical measurement M_2 verifies the cavity shift.

The first panel of figure 9.2a) shows the same behaviour as the blue probing for short delays. The conditional noise from M_2 given M_1 (red shading) is less than QPN, as expected from a squeezed state. As we allow time to pass between measurements, the linear relationship remains, but it decreases until it becomes negative, however maintaining a conditional noise that remains below QPN. In figure 9.2b) we can see that the evolution of the factor α follows a similar behaviour to the blue probing, but in the opposite direction in accordance with our expectation from equation (9.2). The "excess" or "deficit" $\alpha - 1$ only differs by the sign, which can be explained from our model in equation (7.12): For a fixed trap geometry and temperature the inhomogeneity of the coupling $(\Delta\Omega)$ would be the same, giving the same "excess" $\alpha - 1$ for both cases, except for the sign of $\beta_1 + \beta_2$. The minimum value of amplification is achieved roughly at

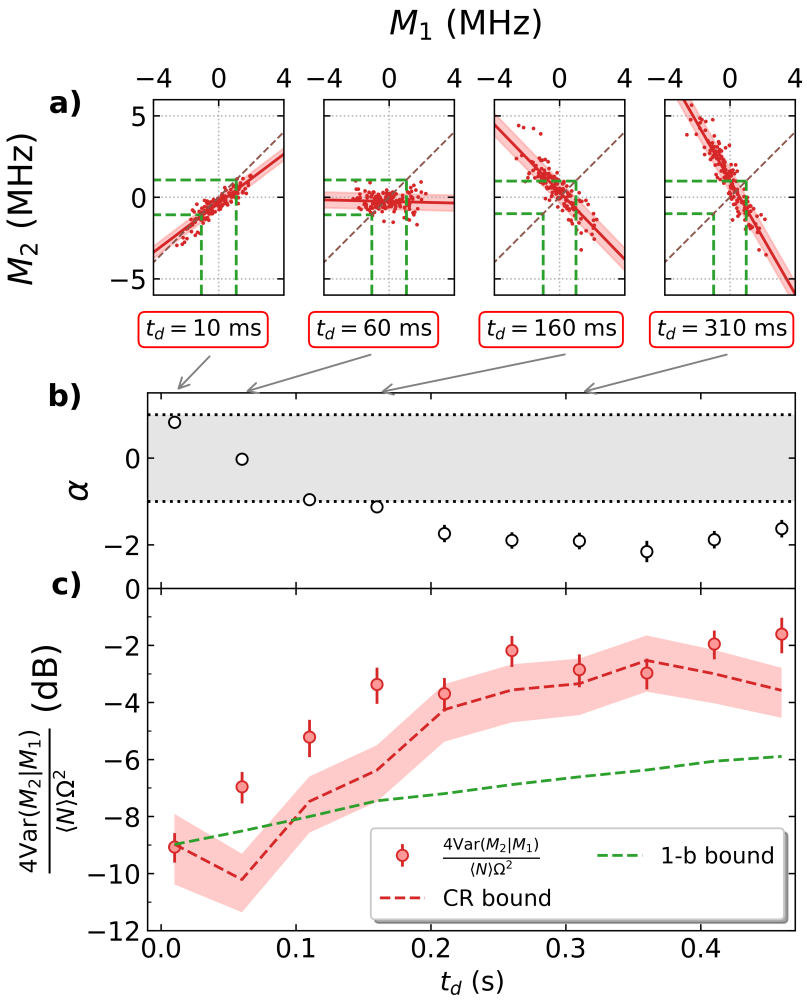

Figure 9.2: a) Squeezing measurement using a Red probe. The linear dependence between the two measurements remains. We include the linear fit from MLE and the conditional noise from Var $(M_2|M_1)$ shown around it in red shading.. Green dashed lines show the estimated QPN for the corresponding atom number. b) The amplification factor as inferred by equation (8.11); the error bars are obtained from bootstrapping with 1000 samplings. The second measurement shows a slope that decreases gradually and turns negative in accordance with our model in equation (9.2). As we observed with the blue probing scheme, there seems to be a dampening effect on the evolution. c) Condition variance compared to QPN calculated from final average atom number, error bars from bootstrapping. The red dashed line shows the Cramer-Rao lower bound from equation (8.12), with shading showing the error given PSN.

the same time as the maximum for the blue probing scheme, between 200 and 300 ms. This can be explained as well by the fact that the dynamics is mostly determined by ω_{ex} and γ_c, which are the same in both cases since we kept density and temperature the same.

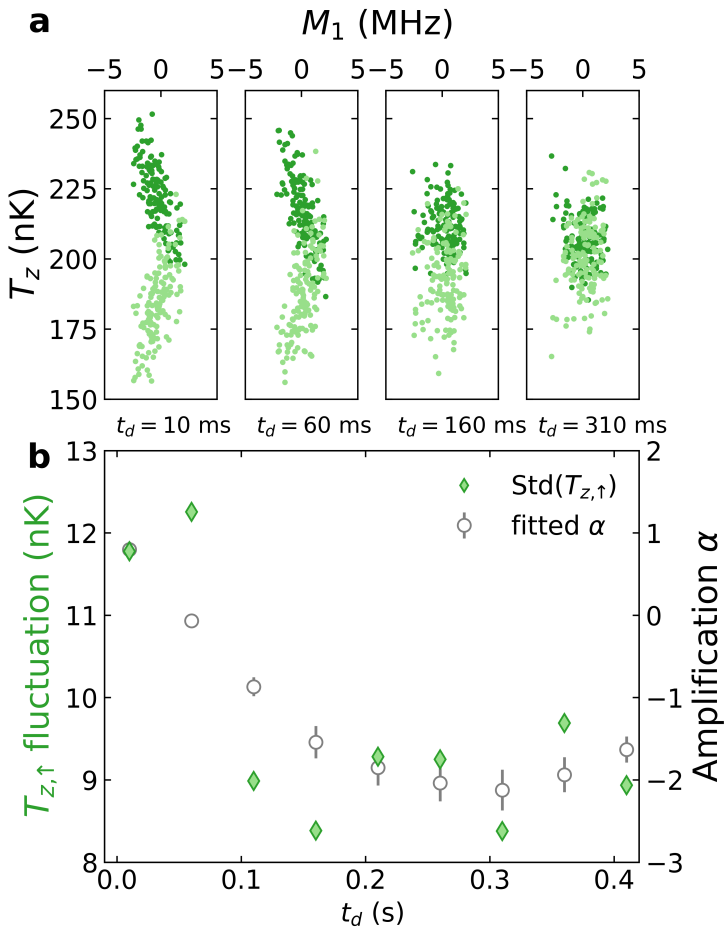

Figure 9.3: The spin-orbit correlation from temperature measurements. a) The temperatures along $\hat{z}$ of states $|\downarrow\rangle$ (light green dots) and $|\uparrow\rangle$ (dark green dots) versus M_1 from the same data set (the offset between the initial temperatures is due to the state-dependent imaging procedure). There is a clear correlation between $T_{z,\uparrow}$ and M_1 (anti-correlation for $|\downarrow\rangle$). b) The time evolution of the temperature fluctuations (standard deviation) of $T_{z,\uparrow}$. The evolution resembles that of the amplification factor α (open circles, right axis) but partially departs for larger delays.

With respect to the noise estimation, we show in figure 9.2c) the conditional variance $\mathrm{Var}\,(M_2|M_1)$ along 150 repetitions for each delay with respect to QPN. As before, we have a gradual degradation of the gain, in particular when compared with the one-body losses bound (shown in the green dashed line). However, this degradation is less drastic than the one we observed in the case of blue probing, and we do not see the large peak at short delays that we had when α increased. The loss of squeezing can be attributed to the amplification itself since. This can be seen in the CR bound we derived in equation (8.12) where the α^2 terms tell us that, as long $|\alpha| > 1$, we would reduce our ability to predict M_2 given M_1, degrading at the same time our ability to measure a phase. It is important to note that this is not the whole story since, $|\alpha| < 1$, we expect some gain on the noise distribution, but this is not apparent in our experimental results.

For completeness, we include an analysis of the correlation between the amplification and the temperature distribution of both the $|\uparrow\rangle$ and $|\downarrow\rangle$ clouds. As before, temperatures $T_\uparrow$ and $T_\downarrow$ are obtained

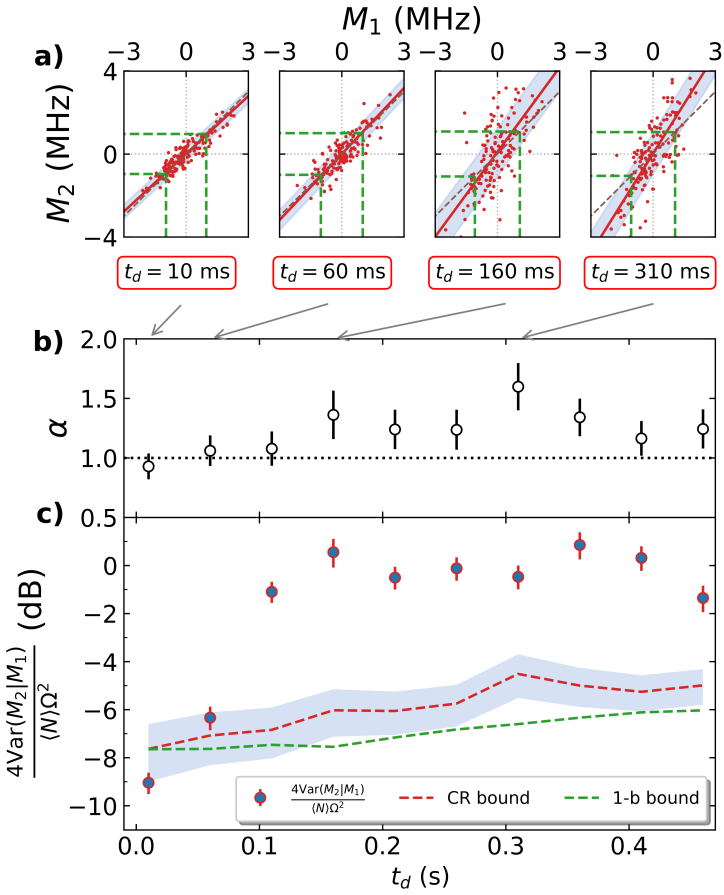

Figure 9.4: a) Squeezing measurement using a Bichromatic scheme. The linear dependence between the two measurements remains but degrades much faster than in the other cases. We include the linear fit from MLE and the conditional noise from Var $(M_2|M_1)$ shown around it in blue shading. Green dashed lines show the estimated QPN for the corresponding atom number b) Amplification factor as inferred by equation (8.11); error bars from bootstrapping with 1000 samplings. There is an increase in the slope that remains close to one as opposed to what we expected. c) Condition variance compared to QPN calculated from final average atom number, error bars from bootstrapping. The red dashed line shows the Cramer-Rao lower bound from equation (8.12), with blue shading showing the error given PSN. We see that the noise level increases significantly in a much shorter time scale.

from the time-of-flight imaging for every shot, providing an experimental test for this mechanism. Similarly to the red probing, a correlation between $T_\downarrow$ and M_1 [Fig. 9.3(a)], is clearly visible. However, in this case, the correlation degrades much faster. The amount of temperature change also depends on α in the expected manner, as can be seen by plotting the shot-to-shot temperature fluctuations (standard deviation ΔT_z) as a function of t_d [Fig. 9.3(b), green diamonds]. As α decreases, the fluctuations are reduced, limited by measurement noise.

9.3 Bichromatic probing

Consider a protocol like the one we followed in section 6.2.1. An ensemble of $N \sim 1.7(2) \times 10^4$ ^{87}Rb atoms is magnetically trapped. We start with all atoms in $|\downarrow\rangle$ and apply a $\pi/2$ pulse on the clock transition to prepare a CSS on the equator of the Bloch sphere. A composite cavity measurement M_1 measures the cavity detuning to determine S_z. This time, the first pulse is blue-detuned by 20 MHz with respect to the cavity resonance, while the second one is red-detuned by the same amount having $\langle n_{11}\rangle = \langle n_{12}\rangle = 6.3(3) \times 10^3$ photons. The cavity shift $\delta\omega_1$ is deduced from the cavity shifts $\delta\omega_\pm$ of the two probe pulses as $\delta\omega_1 \equiv (\delta\omega_+ - \delta\omega_-)/2$. Then, after a delay t_d, a second identical measurement M_2 verifies the cavity shift.

The first panel of figure 9.4a) shows the same behaviour as the blue probing for short delays. The conditional noise from M_2 given M_1 (blue shading) is less than QPN, as expected from a squeezed state. As we allow time to pass between measurements, the linear relationship remains, but the correlation decreases rapidly, exceeding QPN in less than 200 ms. In figure 9.4b) we can see that there is some residual amplification $\alpha > 1$. Moreover, there seems to be an increase in the amplification factor. This could be due to an imperfect compensation of the inhomogeneous dephasing. Indeed, as discussed before, the red profile of our cavity is close to a higher order mode, possibly bringing a different transversal profile to the red side of the probing; this would not allow for a complete compensation of the phase inhomogeneity. This leads to reduced amplification. Besides, one should consider that the atoms have been moving during the time of the echo pulse, with a duration of 26.55 ms; this is a multiple of the oscillation period in the transversal direction, but we would still expect the atoms not to see exactly the same light profile in both probe pulse.

Concerning the noise estimation, we show in figure 9.4c) the conditional variance $\mathrm{Var}\,(M_2|M_1)$ along 150 repetitions for each delay with respect to QPN. We have a quick degradation of the gain, even considering the CR bound (shown in the red dashed line). It is not clear to us the origin of this quick degradation of the squeezing. Still, it may be attributed to more complex spin dynamics due to the different transversal intensity profiles of the two probes. We manage to get rid of the "linear" term of the amplification process, but this is not enough to preserve a useful state.

9.4 Lower Atom Number

In our model, the atom number has two main contributions to the amplification effect. In equation (7.12), we see that a factor of N accompanies the inhomogeneity term $(\Delta\Omega)^2$ due to the scaling of the sum in equation (7.10). This could be understood simply as more atoms being involved in the effect "pulling" the cavity resonance in the amplified direction. From this observation, we would expect that the discrepancy $\alpha - 1$ will be reduced proportionally to a reduction in the atom number N. The second effect comes from the dependence of the spin-exchange rate ω_{ex} and lateral-collisional γ_c. These rates govern the amplification dynamics and are proportional to the atomic density. A reduction in atom number should slow down the dynamics, giving a larger time before an $|\alpha| > 1$ is reached.

Experimental protocol. To verify our claims, we followed the protocol in the previous section identically (see section 9.1), shown in figure 6.2. An ensemble of $N = 1.0(1) \times 10^4$ ^{87}Rb atoms is magnetically trapped. We start with all atoms in $|\downarrow\rangle$ and apply a $\pi/2$ pulse on the clock transition to prepare a CSS on the equator of the Bloch sphere. A composite cavity measurement M_1 measures the cavity detuning

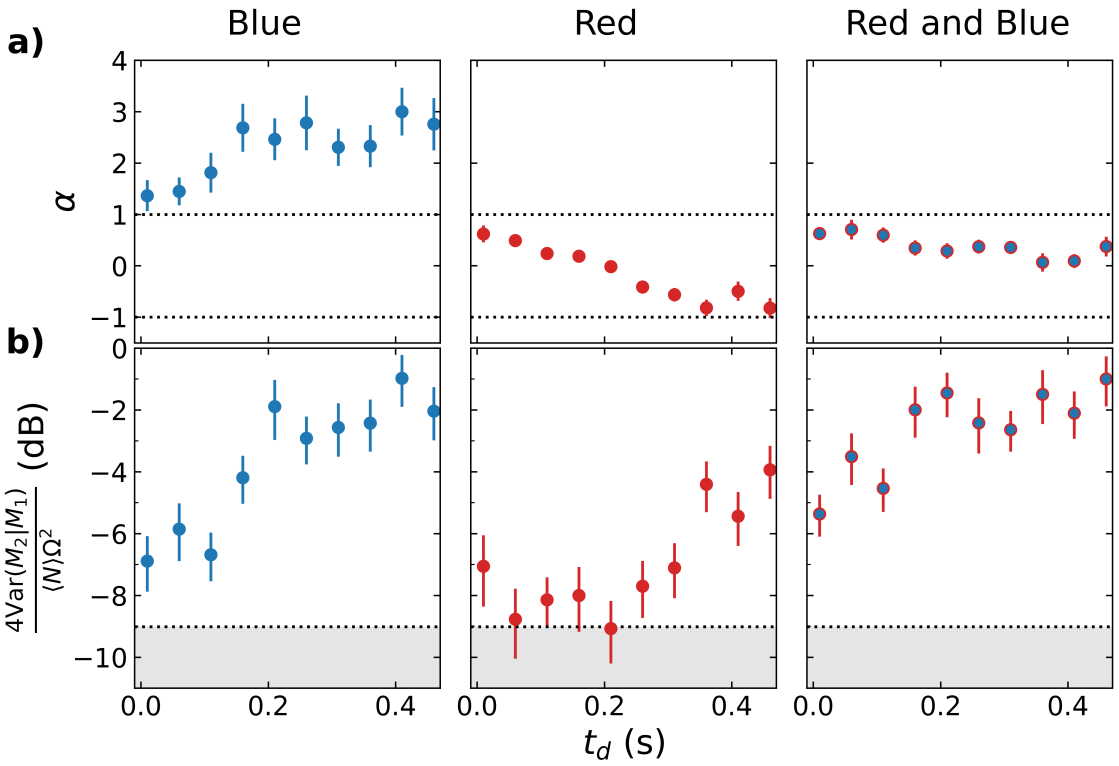

Figure 9.5: Amplification for $N = 1.0(1) \times 10^4$ atoms. a) The amplification factor inferred by equation (8.11) for each of the three probing schemes; error bars from bootstrapping with 1000 samplings. A slower evolution can be observed when reducing the atom number. Moreover, the excess $\alpha - 1$ roughly halves as the atom number is reduced by half with respect to the previous analysis. b) The conditional variance compared to QPN calculated from the final average atom number. The error bars are obtained from bootstrapping with 1000 samples. We include the PSN threshold in grey shading.

to determine S_z. We perform 50 repetitions for each delay using each of the 3 probing schemes: Blue interrogation, meaning both probes are blue-detuned by 20 MHz with respect to the cavity resonance. Red interrogation, when both probes are red-detuned by 20 MHz with respect to the cavity resonance. Finally, we tried a red and blue interrogation, where the first pulse of the composite measurement is red-detuned, while the second one is blue-detuned. The cavity shift $\delta\omega_1$ is deduced from the cavity shifts $\delta\omega_\pm$ of the two probe pulses as $\delta\omega_1 \equiv (\delta\omega_+ - \delta\omega_-)/2$. Then, after a delay t_d, a second identical measurement M_2 verifies the cavity shift.

Effect on α The overall results are shown in figure 9.5. If we compare the first panel of 9.5 a) with figure 6.5 b), we can see a reduction on the discrepancy $\alpha - 1$: When we used 1.8×10^4, this discrepancy reaches a maximum value of 3 in about 200 ms before decreasing. Here, a reduction of 40% in the atom number brings down the excess close to 1.8 within the statistical resolution[3], consistent with equation (7.12). Moreover, there is no evident reduction in the amplification factor as observed for larger atom numbers after 300 ms. This is as predicted from the ω_{ex} reduction, which should slow down the dynamics.

For the red probing case, we can compare the second panel of figure 9.5 a) with figure 9.2 b). Once again, for higher atom numbers, the discrepancy $|\alpha - 1|$ reaches a maximum in between 200 and 300 ms with a maximum value of around 3. When we reduce the atom number by 40% of the previous sequence, the maximum discrepancy

[3] All other things being equal, the larger error bars on α for the blue probing might come from a larger fluctuation in the atom number compared to the other probing schemes due to the temperature regulation problems in the room that we had at the time of taking the blue probe measurements.

is reduced to $|\alpha - 1| \approx 2$. Moreover, this maximum is reached at a later time, with not a clear trend of decrease afterwards. Interestingly, this allows us to keep the amplification factor within $|\alpha| < 1$, which, we have already established, prevents a degradation on the phase inference protocol of chapter 8.

Finally, for the bi-chromatic probing, we can compare figure 9.4 b) with the third and last panel of figure 9.5 a). We first point out that, contrary to the analysis in section 9.3, the first probe pulse is red-detuned in this case. As before, residual amplification seems to occur in the sense direction. This is consistent with the idea that a first probe triggers the amplification mechanism and that the second probe compensates for this partially but does not get rid of the phenomenon due to differences in the transversal profile of the light in the cavity and the movement of the atoms in the trap. In the case of a low atom number, the evolution seems to have fewer fluctuations, but the maximum discrepancy $|\alpha - 1|$ seems larger than in a higher atom number. In neither of both cases, we have a clear time dependence of the amplification itself.

Effect on the Conditional Variance. We now evaluate the effect on the conditional variance $\mathrm{Var}\,(M_2|M_1)$ with respect to QPN. As we have discussed in chapter 8, this is directly related to our ability to distinguish two different values of the accumulated phase by our state[4]. The ensemble of results for the three different probing schemes are shown in figure 9.5 b). Comparing the red and blue probing schemes, we observe that both begin with roughly the same squeezing, around -7 dB. However, for the blue interrogation, the conditional variance degrades as $|\alpha|$ increases, while the red probing seems to have a momentary reduction in its conditional variance as α approaches zero. This is consistent with equation (8.13), where, for $\alpha = 0$, the only expected contributions to noise are those related to one-body losses and detection. We have included the PSN contribution of a single measurement normalised to QPN in grey shading for comparison. Then, the conditional variance increases again as α turns negative.

[4] As a reminder, $\sqrt{\mathrm{Var}\,(M_2|M_1)}$ measures the vertical spread of M_2 around the line $M_2 = \alpha M_1 + f(\phi_0)$ and we have claimed in equation (8.12) that this is the noise figure for $f(\phi)$.

For the case of red and blue probing, the last panel of figure 9.5 b), a trend consistent with our model, is harder to distinguish. We still observe degradation of the conditional noise as with the case of a higher atom number we observed in figure 9.4 c). However, this loss seems to be slower and less drastic since, as opposed to the high-N case, the noise distribution remains under QPN.

Use in Phase Measurements. There is a strong case for the use of low atom numbers due to the decrease and slow down of dynamics we observe. This may be the best approach if the objective is to observe the phase measurement below QPN. Nevertheless, in practice, the metrological gain obtained by reducing amplification should be evaluated against the metrological loss due to the reduction of the atom number itself. For example, in our base case, for $t_d = 200$ ms in red probing, the low atom number shows -9 dB of conditional vari-

ance, compared with the -4 dB in the case of a high atom number, but the QPN itself is shifted by 5 dB in terms of phase uncertainty when reducing the atom number by 40% as we did.

As for the bi-chromatic probing, these results may not seem particularly encouraging, but one must still consider the effect of the global phase shift imprinted on the atoms. We have implemented a correction on the phase of our pulses in the protocol described in the previous chapter 8. This correction is, however, limited by PSN itself and may introduce additional noise to our measurement of phase ϕ. Choosing $\vartheta = \phi_d(n_{1,2} - n_{1,1})$ with an erroneous calibration will not, on average, bias our result on inferring ϕ, but would introduce additional noise and may transfer part of the anti-squeezed quadrature into our measurement. For a bi-chromatic scheme, the global shift imprinted by the probe is null, at least within PSN. This may reduce the effect of noise introduced by the phase correction. Therefore, we should not immediately discard this probing scheme.

9.5 Phase Measurements in Other Probing Schemes

We have established different probing schemes to control the amplification. Now, we can study using these probing schemes to measure a phase. For this effect, we will proceed with the same experimental protocol we followed to test the blue probing in section 8.3. We will try these schemes in the "low atom number" case. More precisely, we use $\langle N_{\mathrm{Red}} \rangle = 1.1(1) \times 10^4$ atoms at time of detection for red probing and $\langle N_{\mathrm{Bi}} \rangle = 1.0(1) \times 10^4$ atoms at time of detection for the bichromatic probing[5].

[5] In this protocol, bi-chromatic was study using an initial blue probe, followed by a red one for M_1.

9.5.1 *Experimental Sequence*

As a reminder, in this protocol, we prepare a coherent state in the equator of the Bloch sphere. A first composite measurement M_1 squeezes the state, conditioned on the detected number of photons $n_{1,1}, n_{1,2}$. Immediately after, a $\frac{\tilde{\pi}}{2}(\vartheta)$ MW+RF pulse[6] turns the squeezed quadrature of the state in the direction of phase accumulation. Here $\vartheta = \phi_d(n_{1,2} - n_{1,2})$ is the average uncompensated phase shift with ϕ_d being the phase shift induced per detected photon as calibrated from the previous section 6.1.2.

[6] Both the calculations and programming of the phase pulse into the DDS that generates the RF component of the pulse are performed in a Teensy microprocessor on every sequence shot.

After a 11 ms delay, a third pulse $\frac{\tilde{\pi}}{2}(\vartheta + \pi - \phi)$ brings the squeezed quadrature towards the population difference direction and a second identical composite measurement is performed. Finally, $N_\uparrow$, $N_\downarrow$ is measured by absorption imaging after a 2.5 ms TOF for $|\downarrow\rangle$ and 5 ms for $|\downarrow\rangle$. After imaging, the stripline is turned on again so that the cavity lock is maintained, and two light pulses with the same power are sent on both sides of the cavity profile to use as a reference for the cavity shift as described in section 5.2.1. We tried 5 different values of phase $\phi = 0, 2, 4, 6, 8°$. We leave ϕ fixed for 100 sequence cycles before changing to the following value. The pulses forming the composite cavity measurements have identical average

photon numbers: $\langle n_{1,1}\rangle = \langle n_{1,2}\rangle = 6.1(1) \times 10^3$ for the blue probing scheme and $\langle n_{1,1}\rangle = \langle n_{1,2}\rangle = 6.1(3) \times 10^3$ for the bi-chromatic scheme. In both schemes, the probe pulses have a duration of 8.85 ms, corresponding with the period of transversal oscillations in the trap.

The total duration of a composite measurement is 45 ms, including a short time gap between the probes and the composite π pulse. The duration of the $\pi/2$ pulses that open and close the interferometer is 60 ms. This implies that the two composite measurements, M_1, M_2, are separated by 131 ms. A composite measurement has passed when measuring the atom number via absorption imaging, together with the two $\pi/2$ pulses and the phase accumulation time. This 176 ms is corrected from the measured atom number to infer the initial atom number.

9.5.2 *Amplification Stability and Phase Inference*

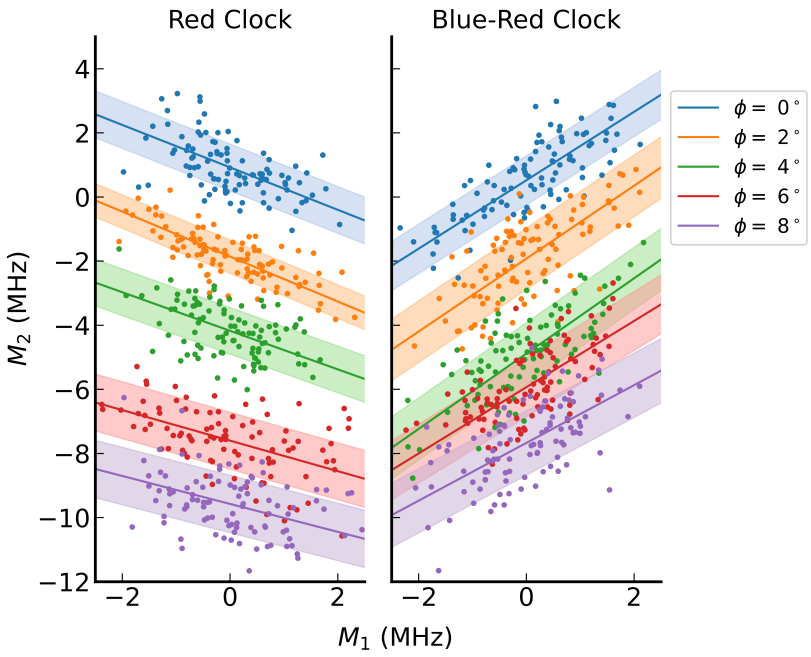

Figure 9.6: Ensemble of data for phase measurement and calibration. Each colour corresponds to a different ϕ value with a fixed number of atoms and measurement strength on the blue side of the cavity profile. The delay between composite measurements is fixed at 125 ms. The shading, in this case, shows $\pm\sqrt{\mathrm{Var}\,(M_2|M_1)}$ around the corresponding fitted line.

In figure 9.6, we can see the ensemble of measurements for the different values of ϕ for each of the probing schemes; as we expected from our model, the correlation between M_1 and M_2 is maintained similarly to what we would have expected from an amplification measurement. We are left to evaluate if α is stable enough and to associate a phase value to each M_2-intersects. We perform a bootstrap analysis with 10^3 resamplings of the same size as the original data; the resulting average α and with error bars from statistical standard deviation are shown in figure 9.7. For the red probing scheme, the amplification factor α is consistent with the results in figure 9.5 a) considering a slight increase of 10% in both the atom number and the number of photons per probe. The inferred amplification factors

are identical within statistical error bars. Similarly, for the bichromatic probing, we again observe a marginal increase in α due to the initial dephasing imparted by the blue probe. We remark larger error bars associated with the bichromatic probing; these could be due to an asymmetry between the transversal intensity profile on both sides of the cavity due to the higher order mode. Unfortunately, we are unable to assess this hypothesis at this time. We refer now to the

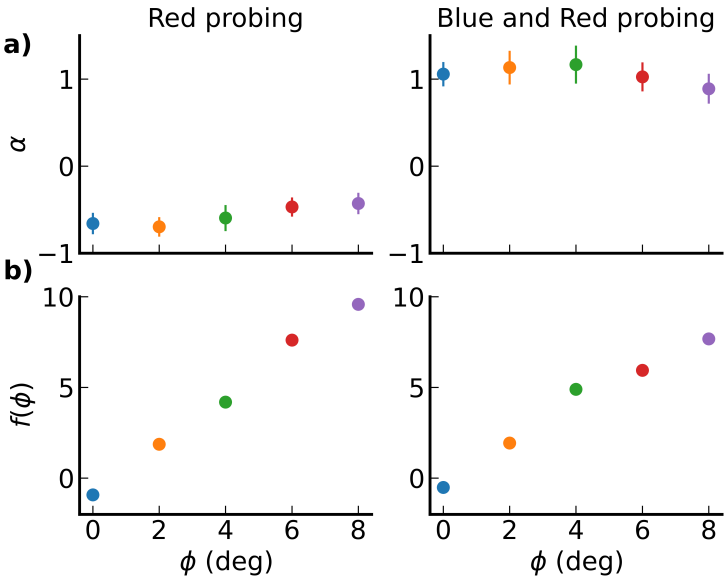

Figure 9.7: Amplification factor α and intersect $f(\phi)$ for the model proposed in section 8.2 for both probing schemes. Error bars obtained from bootstrapping with 1000 resamplings.

intersect $f(\phi)$ in figure 9.7 b). For the red probing scheme, the accumulation seems to follow a regular behaviour as expected for small phases ϕ. However, for the bichromatic probing, there appears to be a lower average shift for $\phi = 6°$ and $\phi = 8°$ compared to smaller values of ϕ. This can be explained by a drop of 10% in the atom number during the experimental cycle due to temperature fluctuations in the room.

9.5.3 *Phase Inference and Noise Figures*

To obtain the accumulated phase by the atomic state, we proceed in the same way we did in section 8.3.2. First, we obtain an α from equation (8.11) equation. For a fixed α, we can deduce by projecting it back to the M_2-axis via the formula

$$\tilde{f}(\phi) = M_2 - \alpha \frac{M_1}{1 + \frac{\sigma^2_{\text{PSN}}}{\sigma^2_{\text{QPN}}}}.$$

From $\tilde{f}$, we can recover the $\phi + \phi_0$ using equation (8.15). Again, the contrast is obtained from a least-square fit on the model described by equation (8.15). For the red probing, we obtain $\mathcal{C}_{\text{Red}} = 0.797(1)$, while $\mathcal{C}_{\text{Bichrom}} = 0.720(4)$ for the bichromatic probing[7]. As expected, the accumulation does follow a direct relation between the applied phase ϕ and the inferred one $\tilde{\phi}$ for both probing schemes.

As for the noise, the bichromatic probing exceeds QPN as marked by the coloured shading in figure 9.8 in a similar way that we saw

[7] Note that this degradation of the contrast of the bichromatic could be accounted by the reduction on the atom number we observed for $\phi = 6°$.

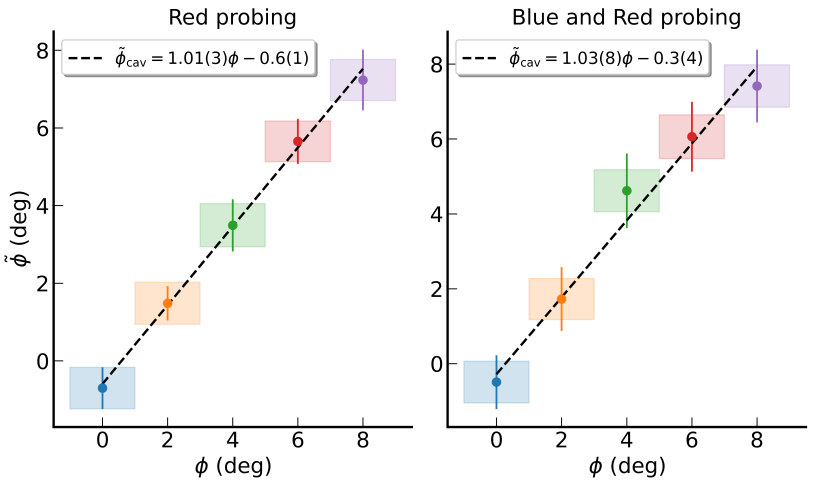

Figure 9.8: Comparison between the inferred phase $\tilde{\phi}$ and the phase ϕ applied to the closing pulse of the interferometer for both probing schemes. The coloured dots and error bars correspond to data acquired from the cavity detection with an adjusted contrast of $\mathcal{C} = 0.575(1)$. The error bars marked the conditional standard deviation $\sqrt{\mathrm{Var}\,(M_2|M_1)}$ from bootstrapping. The shading marks the $\pm\frac{1}{\sqrt{N}}$ as the limit of QPN for phase. The dashed black line is a simple linear fit between the inference $\tilde{\phi}_0$ and the applied ϕ. The red dots are inferred from saturated absorption.

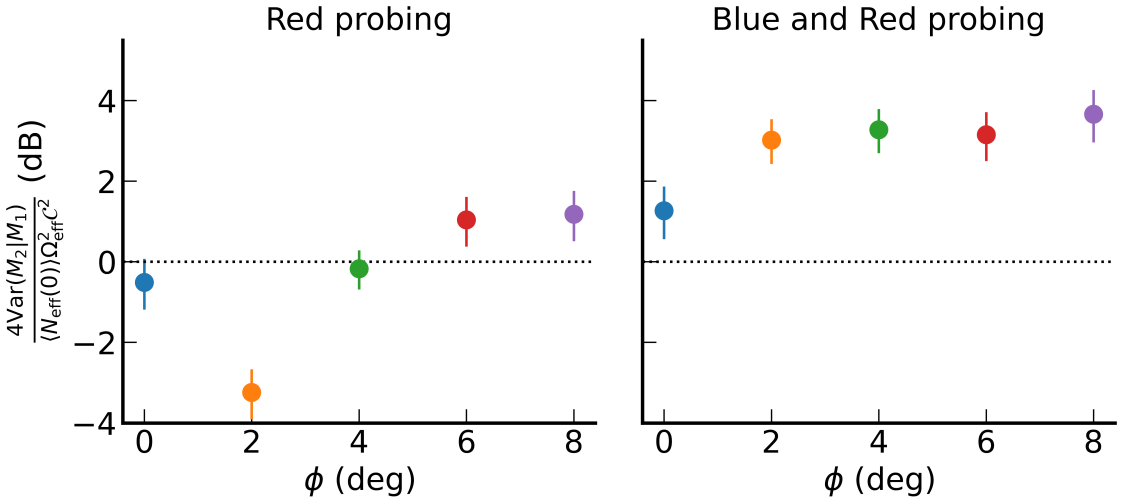

Figure 9.9: Metrological gain for both probing schemes. In analogy with the Wineland parameter, we compare the conditional variance $\mathrm{Var}\,(M_2|M_1)$ with respect to $\frac{N_{\mathrm{eff}}\Omega_{\mathrm{eff}}^2\mathcal{C}^2}{4}$.

for the blue probing in figure 8.6. However, for red probing, the situation seems to be better. To be more precise, we compare the conditional variance in units of spin $\mathrm{Var}\,(M_2|M_1)\,/\Omega^2$ in analogy with the Wineland parameter as

$$\xi^2_{\mathrm{Amp}} = N_{\mathrm{eff}}\frac{\mathrm{Var}\,(M_2|M_1)}{\Omega^2\left|\left\langle\vec{S}\right\rangle\right|^2} = \frac{4\mathrm{Var}\,(M_2|M_1)}{N_{\mathrm{eff}}\Omega^2_{\mathrm{eff}}\mathcal{C}^2}; \tag{9.3}$$

results are shown in figure 9.9. We seem to have at least three phase values for which the phase measurement is below QPN for the red probing scheme. Is this consistent with our expectations? There is a clear degradation of the noise level with respect to what we showed in figure 9.5 b). The inclusion of the contrast term could account for this in the following way: The PSN level for this measurement is about $\xi^2_{N,\mathrm{PSN}} = -9.5$ dB in variance normalised to $\frac{N\Omega^2}{4}$. If we consider this as the limit for the conditional squeezing in our model presented in 8.2, equation (8.12) tells us that the best figure of noise we could expect is given by

$$\xi^2_{\mathrm{Amp}} \geq \mathcal{C}^{-2}\left((1+\alpha^2)\xi^2_{N,\mathrm{PSN}} + e^{-\gamma_{1b}t}(1-e^{-\gamma_{1b}t}\right) \tag{9.4}$$

For this set of measurements, this is approximately -4.9 dB. This is at least 2 dB better than our best set, but it clearly degrades for the other values of phase. We hypothesise that this additional degradation comes from an imperfect calibration of the phase correction applied. More recent measurements have shown a discrepancy in ϕ_d when measured on different sides of the cavity profile, being systematically larger for the red profile compared to the blue. This discrepancy is probably due to a difference in the transversal intensity profile of the probe on both sides of the profile due to the parasitic higher-order mode.

10
Conclusion and Outlook

Moi seul, je sais ce que j'aurais pu faire...
Pour les autres, je ne suis tout au plus qu'un peut-être.
Le Rouge et le Noir, Stendhal

In this thesis, we have continued the work following the design[75] and set-up[67] of TACC-2. After the open questions left by Huang [67], we have improved our understanding of the interplay between the squeezed states and the spin dynamics brought about by ISRE. In Chapter 6, we have presented and extended some of the results that were published this year in [65], where we have presented a metrological squeezing of 8.6 dB. In Chapter 7, we extended our model for the amplification mechanism and used it to infer information on the spin states that we are able to produce. We showed that our state remains squeezed even after 0.6 s, making it comparable to interrogation times used in applications.

In Chapter 8, we showed a first-phase measurement using squeezed states in the presence of amplification. To this effect, we proposed an experimental protocol for calibration and introduced a statistical analysis based on MLE for the treatment of the data coming from such an approach. Once convinced that our model is capable of explaining the phenomena we observe, we proceed in Chapter 9 to study different approaches to control these spin dynamics. After some exploration, we concluded Chapter 9 with a phase measurement below QPN using a reduced number of atoms ($N \approx 10^4$) in a red probing scheme. Although these results are preliminary, they remain encouraging.

One could reasonably believe that we are studying some pathological or esoteric phenomena, a side effect of our apparatus; I want to say a few words about this claim. The phenomenon of spin waves and spin interactions has been largely studied through the years. Originally, this was a subject that concerned condensates and Fermi gases. Both TACC and TACC-2, with their long coherence lifetime and ease of control, open the doors to study new regimes in the interplay between internal and external degrees of freedom. Conversely, more detailed and rigorous treatments of such interaction would help to understand the effect of this interaction in the entanglement of the spin degree of freedom.

From a more *pragmatic* point of view, we expect these interactions to be ubiquitous in other trapped atom experiments using squeezed states. Previous squeezing experiments with alkali atoms have been limited to timescales of a few milliseconds (e.g. 5 ms in [123], 2 ms in [101], 1 ms in [124], 8 ms in [125]), while interrogation times in real clocks and sensors are typically ten to hundred times longer [126–128]. We expect that, as coherence and interrogation times get longer, the question won't be whether such effects are present but instead how they affect the functioning of the device and how to circumvent it or benefit from it.

With respect to the future, we are confident that our understanding is sufficient to reduce the task of having an operating clock with squeezed states to a simple exploration on a reduced space of parameters.

The first step is to take care of the problems mentioned in some of the notes at the margins: Replace the 2D MOT bench to improve the atom number stability shot-to-shot, fix the temperature regulation of the room, characterise some of the components that have degraded over time, etc. Other steps are more complex but reachable in the immediate future. These include characterising the influence of the phase calibration mentioned in section 6.1.2, studying the effect of the parasitic mode in the red side of the cavity profile and implementing a way to measure the atom number at the beginning of the sequence via a QND measurement.

Part V

Appendices and Calculations

11
Inference

11.1 Cavity Shift Inference Calculations

As described in 5.2.1, the number of photons detected at the photon counter when probing the red and blue profiles of the empty cavity can be written as

$$n_b = \frac{I}{1+\left(\frac{p-\omega_0}{\gamma}\right)^2} \qquad n_r = \frac{I}{1+\left(\frac{p+\omega_0}{\gamma}\right)^2}. \tag{11.1}$$

Introducing $\chi = n_b/n_r$

$$\chi - 1 = \frac{1+\left(\frac{p+\omega_0}{\gamma}\right)^2}{1+\left(\frac{p-\omega_0}{\gamma}\right)^2} - 1 = \frac{\left(\frac{p+\omega_0}{\gamma}\right)^2 - \left(\frac{p-\omega_0}{\gamma}\right)^2}{1+\left(\frac{p-\omega_0}{\gamma}\right)^2} = \frac{4pc}{\gamma^2+p^2+\omega_0^2-2p\omega_0}$$

$$\omega_0^2 - 2p\frac{\chi+1}{\chi-1}\omega_0 + \gamma^2 + p^2 = 0.$$

Note that $\omega_0 > 0$ if $\chi > 1$ and $\omega_0 < 0$ if $\chi < 1$ for small shifts. Then, we conclude that the correct expression for the cavity shift is as follows:

$$\tilde{\omega}_0 = \begin{cases} p\left(\frac{\chi+1}{\chi-1} - \sqrt{\left(\frac{\chi+1}{\chi-1}\right)^2 - 1 - \left(\frac{\gamma}{p}\right)^2}\right) & \text{if } \chi < 1 \\ 0 & \text{if } \chi = 1 \\ p\left(\frac{\chi+1}{\chi-1} + \sqrt{\left(\frac{\chi+1}{\chi-1}\right)^2 - 1 - \left(\frac{\gamma}{p}\right)^2}\right) & \text{if } \chi > 1 \end{cases}$$

plugin back the photon number[1]:

[1] We use $\frac{\chi+1}{\chi-1} = \frac{n_b+n_r}{n_b-n_r}$

$$\tilde{\omega}_0 = \begin{cases} p\left(\frac{n_b+n_r}{n_b-n_r} - \sqrt{\left(\frac{n_b+n_r}{n_b-n_r}\right)^2 - 1 - \left(\frac{\gamma}{p}\right)^2}\right) & \text{if } n_b < n_r \\ 0 & \text{if } n_b = n_r \\ p\left(\frac{n_b+n_r}{n_b-n_r} + \sqrt{\left(\frac{n_b+n_r}{n_b-n_r}\right)^2 - 1 - \left(\frac{\gamma}{p}\right)^2}\right) & \text{if } n_b > n_r \end{cases}$$

and we can solve for I:

$$\tilde{I} = \frac{n_b}{2}\left(1+\left(\frac{p-\tilde{\omega}_0}{\gamma}\right)^2\right) + \frac{n_r}{2}\left(1+\left(\frac{p+\tilde{\omega}_0}{\gamma}\right)^2\right)$$

Once the atoms are in the cavity, the centre shifts to ω_0'. Assuming that the cavity maximal transmission is not affected by this, we can infer the new cavity centre ω_0'. Assume the cavity is probed at ps with $s = \pm 1$ for the blue or red probing

$$n = \frac{I}{1 + \left(\frac{ps - \omega_0'}{\gamma}\right)^2} \Rightarrow \left(\frac{ps - \omega_0'}{\gamma}\right)^2 = \frac{I}{n} - 1.$$

Note that, since $|p| \sim \gamma > |\omega_0|$ in general, the sign of $ps - \omega_0'$ is determined by s leading to the cavity shift:

$$\delta\tilde{\omega}_c = \tilde{\omega_0'} - \tilde{\omega}_0 = ps - s\gamma\sqrt{\frac{\tilde{I}}{n} - 1} - \tilde{\omega}_0.$$

11.1.1 *Photon Shot Noise*

To infer the photon shot noise contribution to the cavity inference we will consider the limit[2] when $\langle n_b \rangle = \langle n_r \rangle = n$, or $\chi = 1$, which leads to

$$\partial_{n_b}\tilde{\omega}_0\big|_{n_b=n_r} = \frac{p^2+\gamma^2}{4np} \qquad \partial_{n_r}\tilde{\omega}_0\big|_{n_b=n_r} = -\frac{p^2+\gamma^2}{4np}.$$

[2] In this limits:

$$\lim_{\chi\to 1}\partial_\chi\tilde{\omega}_0 = \frac{p^2+\gamma^2}{4p},$$
$$\partial_{n_b}\chi = \frac{\chi}{n_b},$$
$$\partial_{n_r}\chi = -\frac{\chi}{n_r}$$

While for $\tilde{I}$:

$$\partial_{n_b}\tilde{I} = \frac{1}{2}\left(1 + \left(\frac{p-\tilde{\omega}_0}{\gamma}\right)^2\right) - n_b\left(\left(\frac{p-\tilde{\omega}_0}{\gamma^2}\right)\left(\partial_{n_b}\tilde{\omega}_0\right)\right),$$
$$\partial_{n_b}\tilde{I}\big|_{n_b=n_r} = \frac{1}{4}\left(1 + \left(\frac{p}{\gamma}\right)^2\right), \quad \partial_{n_r}\tilde{I}\big|_{n_b=n_r} = \frac{1}{4}\left(1 + \left(\frac{p}{\gamma}\right)^2\right).$$

Thus, the Jacobian of the transformation is:

$$\frac{\partial(I,\omega_0)}{\partial(n_b,n_r)}\bigg|_{\tilde{\omega}_0=0} = \begin{pmatrix}\partial_{n_b}I & \partial_{n_r}I\\ \partial_{n_b}\omega_0 & \partial_{n_r}\omega_0\end{pmatrix}\bigg|_{\tilde{\omega}_0=0} = \frac{p^2+\gamma^2}{4}\begin{pmatrix}\frac{1}{\gamma^2} & \frac{1}{\gamma^2}\\ \frac{1}{np} & -\frac{1}{np}\end{pmatrix}.$$

Using error propagation:

$$\sigma_{\omega_0} \approx \sqrt{\left|\partial_{n_b}\omega_0\right|^2\sigma_{n_b}^2 + \left|\partial_{n_r}\omega_0\right|^2\sigma_{n_r}^2} = \sqrt{2n\left(\frac{p^2+\gamma^2}{4np}\right)^2}$$
$$= \frac{p^2+\gamma^2}{\sqrt{8n}p} = \frac{\gamma^2}{\sqrt{8n}p}\left(1 + \frac{p^2}{\gamma^2}\right),$$
$$\sigma_I \approx \sqrt{\left|\partial_{n_b}I\right|^2\sigma_{n_b}^2 + \left|\partial_{n_r}I\right|^2\sigma_{n_r}^2} = \sqrt{2n\left(\frac{p^2+\gamma^2}{4\gamma^2}\right)^2}$$
$$= \frac{\sqrt{2n}}{4}\left(1 + \frac{p^2}{\gamma^2}\right).$$

When atoms are present in the cavity, we measure n_s photons on the s side of the cavity shifting the cavity according to

$$\delta\tilde{\omega}_c = \tilde{\omega_0'} - \tilde{\omega}_0 = ps - s\gamma\sqrt{\frac{\tilde{I}}{n} - 1} - \tilde{\omega}_0.$$

As before $\omega_0 \approx 0$ and also $\omega_0' \approx 0$, with $\partial_{\omega_0}\delta\omega_c|_{\omega_0=0,\omega_0'=0} = -1$. Using that $\gamma\sqrt{\frac{I}{n_s}-1} = p - s\omega_0'$ we have:

$$\partial_I \delta\omega_c|_{\omega_0=0,\omega_0'=0} = -\frac{s\gamma^2}{2(p-s\omega_0')n_s}\bigg|_{\omega_0'=0} = -\frac{s\gamma^2}{2pn_s},$$

$$\partial_{n_s}\delta\omega_c|_{\omega_0=0,\omega_0'=0} = \frac{s\gamma}{2\sqrt{\frac{I}{n_s}-1}}\frac{I}{n_s^2}\bigg|_{\omega_0=0,\omega_0'=0} = \frac{s\gamma^2}{2pn_s}\left(1+\frac{p^2}{\gamma^2}\right).$$

From error propagation and $\sigma_{n_s}^2 = n_s$:

$$\begin{aligned}\sigma_{\delta\omega_c} &= \sqrt{|\partial_{\omega_0}\delta\omega_c|^2\sigma_c^2 + |\partial_I\delta\omega_c|^2\sigma_I^2 + |\partial_{n_s}\delta\omega_c|^2\sigma_{n_s}^2} \\ &= \frac{\gamma^2}{p}\left(1+\frac{p^2}{\gamma^2}\right)\sqrt{\frac{1}{8n}+\frac{n}{32n_s^2}+\frac{1}{4n_s}}.\end{aligned}$$

If we introduce the factor $r_p = \frac{n_s}{n}$

$$\begin{aligned}\sigma_{\delta\omega_c} &= \frac{\gamma^2}{p}\left(1+\frac{p^2}{\gamma^2}\right)\sqrt{\frac{1}{8n}+\frac{1}{32r_p^2 n}+\frac{1}{4r_p n}} \\ &= \frac{\gamma^2}{2p\sqrt{n}}\left(1+\frac{p^2}{\gamma^2}\right)\sqrt{\frac{1}{2}+\frac{1}{r_p}+\frac{1}{8r_p^2}}.\end{aligned}$$

11.2 Maximum Likelihood Calculations for Linear Regression

To simplify notation, we identify $M_1 \to X$, and $M_2 \to Y$. As it was described in section 8.2 The reduced model for the sampled data is then given by:

$$\begin{aligned}P(\delta\omega_1, \delta\omega_2; \alpha, \varphi|X, Y) &\propto P(X|\delta\omega_1)P(Y|\delta\omega_2) \\ &\quad \times P(\delta\omega_2|\delta\omega_1;\alpha,\varphi)P(\delta\omega_1). \qquad (11.2)\end{aligned}$$

11.2.1 *Marginalisation*

We can then marginalise with respect to $\delta\omega_2$:

$$\begin{aligned}\int \mathrm{d}\delta\omega_2\; P(Y|\delta\omega_2)P(\delta\omega_2|\delta\omega_1;\alpha,\varphi) &\propto \int \mathrm{d}\delta\omega_2\; e^{-\frac{(Y-\delta\omega_2)^2}{2\sigma_y^2} - \frac{(\delta\omega_2-\delta\hat{\omega}_2)^2}{2\sigma_{1b}^2}} \\ &\propto \exp\left\{-\frac{(Y-\delta\hat{\omega}_2)^2}{2(\sigma_{1b}^2+\sigma_y^2)}\right\},\end{aligned}$$

from which

$$P(\delta\omega_1;\alpha,\varphi|X,Y) \propto P(X|\delta\omega_1)P(\delta\omega_1)\exp\left\{-\frac{(Y-\delta\hat{\omega}_2)^2}{2\sigma_Y^2}\right\}, \quad (11.3)$$

where we have introduced $\sigma_Y^2 = \sigma_{1b}^2 + \sigma_y^2$ to simplify notation and also $\delta\hat{\omega}_2 = \alpha\delta\omega_1 + f(\varphi)$. Finally we can marginalise with respect to $\delta\omega_1$, introducing[3] $\sigma_T^2 = \left(\frac{1}{\sigma_x^2} + \frac{1}{\sigma_{\mathrm{QPN}}^2} + \frac{\alpha^2}{\sigma_Y^2}\right)^{-1}$:

[3] We will make use of the identity $\partial_\alpha\sigma_T^2 = -2\alpha\frac{\sigma_T^4}{\sigma_Y^2}$ later.

$$P(\alpha,\varphi|X,Y) \propto \int \mathrm{d}\delta\omega_1 \ \exp\left\{-\frac{(X-\delta\omega_1)^2}{2\sigma_x^2}-\frac{\delta\omega_1^2}{2\sigma_{\mathrm{QPN}}^2}\right\}\exp\left\{-\frac{(Y-\delta\hat{\omega}_2)^2}{2\sigma_Y^2}\right\}$$
$$\propto \sigma_T \exp\left\{-\frac{\left(\alpha^2+\frac{\sigma_Y^2}{\sigma_{\mathrm{QPN}}^2}\right)X^2+\left(1+\frac{\sigma_x^2}{\sigma_{\mathrm{QPN}}^2}\right)(Y-f(\varphi))^2-2\alpha X(Y-f(\varphi))}{2\sigma_x^2\sigma_Y^2/\sigma_T^2}\right\}. \tag{11.4}$$

11.2.2 *Maximum Likelihood*

In practice, we would measure n points (X_i, Y_i) with the same experimental conditions to infer α as a calibration parameter. Whenever we refer to statistical averages of such ensemble we write $\langle . \rangle$. We can simply proceed using a MLE to infer α and $f(\varphi)$. The log-likelihood is given:

$$L(\alpha,f) = \frac{n}{2}\ln\sigma_T^2 - \sum_i \frac{\left(\alpha^2+\frac{\sigma_Y^2}{\sigma_{\mathrm{QPN}}^2}\right)X_i^2+\left(1+\frac{\sigma_x^2}{\sigma_{\mathrm{QPN}}^2}\right)(Y_i-f)^2-2\alpha X_i(Y_i-f)}{2\sigma_x^2\sigma_Y^2/\sigma_T^2},$$
$$\frac{L(\alpha,f)}{n} = \frac{1}{2}\ln\sigma_T^2 - \frac{\left(\alpha^2+\frac{\sigma_Y^2}{\sigma_{\mathrm{QPN}}^2}\right)\langle X_i^2\rangle+\left(1+\frac{\sigma_x^2}{\sigma_{\mathrm{QPN}}^2}\right)\langle (Y_i-f)^2\rangle-2\alpha\langle X_iY_i\rangle+2\alpha\langle X_i\rangle f}{2\sigma_x^2\sigma_Y^2/\sigma_T^2}.$$

We proceed to obtain the gradients with respect to the parameter to find the adequate maxima:

$$\frac{\partial_f L(\alpha,f)}{n} = \sigma_T^2\frac{\left(1+\frac{\sigma_x^2}{\sigma_{\mathrm{QPN}}^2}\right)(\langle Y_i\rangle - f)-\alpha\langle X_i\rangle}{\sigma_x^2\sigma_Y^2}.$$

Now, with respect to α:

$$\frac{\partial_\alpha L(\alpha,f)}{n} = \frac{\alpha\sigma_T^4}{\sigma_x^2\sigma_Y^2}\left[-\frac{\langle X_i^2\rangle}{\sigma_x^2}+\left(1+\frac{\sigma_x^2}{\sigma_{\mathrm{QPN}}^2}\right)\frac{\langle (Y_i-f)^2\rangle}{\sigma_Y^2}+\left(\frac{1}{\sigma_T^2}-\frac{2\alpha^2}{\sigma_Y^2}\right)\frac{(\langle X_iY_i\rangle-\langle X_i\rangle f)}{\alpha}\right].$$

For later use, we also calculate the second derivative with respect to $f(\varphi)$:

$$\partial_f^2 L(\alpha,f) = -\sigma_T^2 n\frac{\left(1+\frac{\sigma_x^2}{\sigma_{\mathrm{QPN}}^2}\right)}{\sigma_x^2\sigma_Y^2} = -\frac{n\left(1+\frac{\sigma_x^2}{\sigma_{\mathrm{QPN}}^2}\right)}{\sigma_Y^2\left(1+\frac{\sigma_x^2}{\sigma_{\mathrm{QPN}}^2}+\alpha^2\frac{\sigma_x^2}{\sigma_Y^2}\right)}.$$

The resulting condition is:

$$\alpha\langle X\rangle = \left(1+\frac{\sigma_x^2}{\sigma_{\mathrm{QPN}}^2}\right)(\langle Y_i\rangle - f(\varphi))$$
$$0 = \alpha^2\frac{\sigma_x^2}{\sigma_Y^2}\mathrm{Cov}(X,Y)+\alpha\left[\mathrm{Var}(X)-\mathrm{Var}(Y)\frac{\sigma_x^2}{\sigma_Y^2}\left(1+\frac{\sigma_x^2}{\sigma_{\mathrm{QPN}}^2}\right)\right]-\mathrm{Cov}(X,Y)\left(1+\frac{\sigma_x^2}{\sigma_{\mathrm{QPN}}^2}\right).$$

Note that when $\sigma_x = 0$, as expected, we recover the usual linear regression

$$f(\varphi) = \langle Y_i\rangle - \alpha\langle X_i\rangle,$$
$$\alpha = \frac{\mathrm{Cov}(X_i,Y_i)}{\mathrm{Var}(X_i)}.$$

In practice, we may infer σ_x and σ_y from the PSN bound we derived in section 5.3, σ_{QPN} can be measured from $\sigma^2_{\text{QPN}} = \text{Var}(X) - \sigma^2_x$. Finally, notice that

$$\begin{aligned}\sigma_{1b} &= \bar{\Omega}\frac{\sqrt{N(t)}}{2}(1 - e^{-\gamma_{1b}t}) \\ &= \bar{\Omega}\frac{\sqrt{N(0)}}{2}(1 - e^{-\gamma_{1b}t})e^{-\frac{\gamma_{1b}}{2}t} = \sigma_{\text{QPN}}(1 - e^{-\gamma_{1b}t})e^{-\frac{\gamma_{1b}}{2}t}.\end{aligned}$$

We can approximate $\text{Var}(Y_i) \approx \alpha^2\sigma^2_{\text{QPN}} + \sigma^2_Y$ which simplifies to:

$$f(\varphi) = \langle Y_i \rangle - \frac{\alpha \langle X_i \rangle}{1 + \frac{\sigma^2_x}{\sigma^2_{\text{QPN}}}}, \tag{11.5}$$

$$\alpha = \frac{\text{Cov}(X_i, Y_i)}{\sigma^2_{\text{QPN}}}. \tag{11.6}$$

For a fixed α, this inference is limited by the Cramer-Rao bound:

$$\begin{aligned}(\delta f)^2 \geq -\frac{1}{\partial^2_f L(\alpha, \varphi)} &= \frac{\sigma^2_Y\left(1 + \frac{\sigma^2_x}{\sigma^2_{\text{QPN}}} + \alpha^2\frac{\sigma^2_x}{\sigma^2_Y}\right)}{n\left(1 + \frac{\sigma^2_x}{\sigma^2_{\text{QPN}}}\right)}, \\ &= \frac{\sigma^2_Y}{n} - \frac{\alpha^2\sigma^2_x\sigma^2_{\text{QPN}}}{n\left(\sigma^2_{\text{QPN}} + \sigma^2_x\right)}.\end{aligned} \tag{11.7}$$

We can know the α with arbitrary precision since the uncertainty of the inference will decrease as $\frac{1}{\sqrt{n}}$. In practice, one would gather a large number of samples to calibrate α with high precision. Figure 11.1 shows a fit for two $f(\phi)$ values with the same α for typical values of QPN and PSN. Montecarlo's estimates show that $\frac{\Delta\alpha}{\alpha}$ may vary by up to 15% independently of its actual value [4], but Δf remains within 10% of the CR bound, being more exact for values closer to 1.

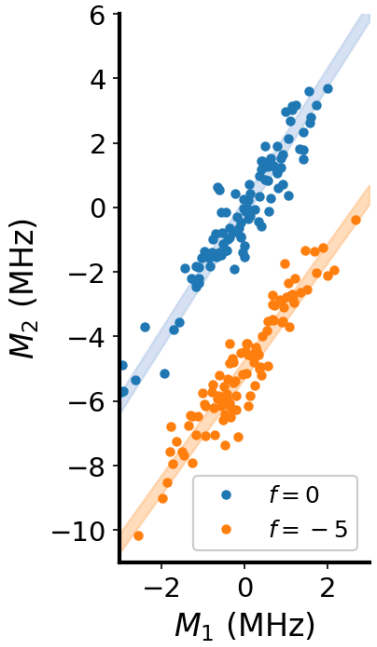

Figure 11.1: Simulation of the inference ($\sigma_{\text{PSN}} = 0.3$, $\sigma_{\text{QPN}} = 1.0$, $\sigma_{1b} = 0$ and $\alpha = 2$). 100 points were sampled to simulate the cavity shift of the two measurements in blue. From those, 100 "measured" points were sampled, in orange (in blue) for $f(\phi) = -5$ ($f(\phi) = -0$). The infrared line is shown in green.

[4] Fluctuactions of α coming from statistical analysis depend mainly on the magnitude of σ_x, σ_Y and σ_{QPN}. The exact value is limited by CR, but the resulting expression is not particularly elucidating.

12
Geometric Calculations

12.1 Bi-Variate Gaussian Distribution

Consider an ellipse described by $\vec{r}(\alpha) = (a\cos\alpha, b\sin\alpha)$. For a point (s,t) in this curve, the corresponding tangent vector is given by $\vec{r}'(\alpha) = (-a\sin\alpha, b\cos\alpha)$. The slope of the corresponding line would thus be $m = -\frac{b}{a}\cot\alpha$. If an angle of β has rotated the ellipse and we care about the resulting y extension, this is the same as measuring the distance to the origin of a tangent line to the ellipse with a slope of $m = -\tan\beta$.

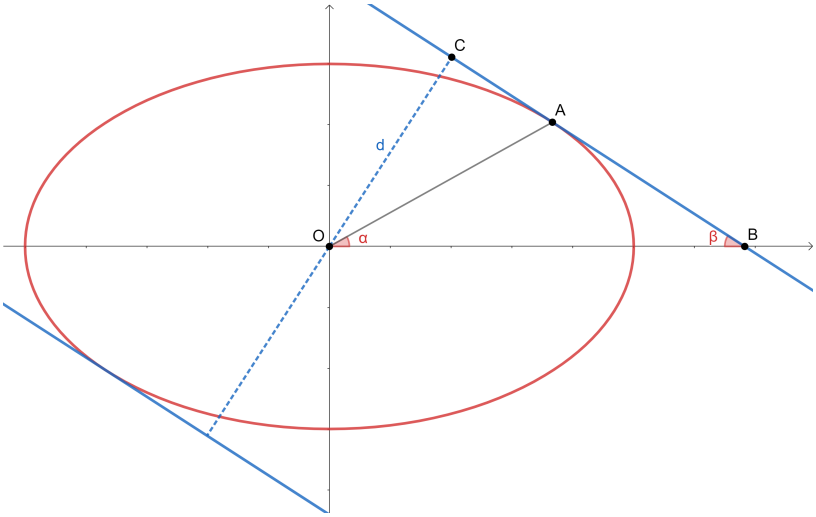

Figure 12.1: Level curve of a Gaussian distribution; it has the shape of an ellipse, the blue lines are tangents to the curve, and the distance of such tangents to the origin is the extension of the marginalised distribution once the distribution has been rotated by an angle β.

Now, consider the equation of the corresponding line $y - t = m(x - s)$ or, equivalently $y - mx + ms - t = 0$. The distance of this line to the origin is given by:

$$d = \frac{|ms - t|}{\sqrt{1 + m^2}} = |s\sin\beta + t\cos\beta|.$$

But we know that $\tan\alpha = \frac{b}{a}\cot\beta$. Then

$$d = \left| a \sin\beta \cos \arctan\left(\frac{b}{a}\cot\beta\right) + b\cos\beta \sin\arctan\left(\frac{b}{a}\cot\beta\right)\right|$$
$$d = \left|\frac{a^2\sin\beta + b^2\cos\beta\cot\beta}{\sqrt{a^2+b^2\cot^2\beta}}\right| = \left|\frac{a^2\sin^2\beta + b^2\cos^2\beta}{\sqrt{a^2\sin^2\beta+b^2\cos^2\beta}}\right|$$
$$d = \sqrt{a^2\sin^2\beta + b^2\cos^2\beta}.$$

Thus, for a bivariate Gaussian distribution for uncorrelated variables x, y with variances σ_x^2, σ_y^2, if we marginalised along a rotated axis, the resulting distribution will have a variance of $\sigma_\beta^2 = \sigma_x^2\sin^2\beta + \sigma_y^2\cos^2\beta$

12.2 Moments Calculation in Presence of One-Body Losses

We derive a simple expression for the one-body loss contribution to noise. For a more complete derivation, refer to [49]. We assume that both modes have the same one-body loss rate γ_{1b}. Using the jump operators $\sqrt{\gamma_{1b}}a$, $\sqrt{\gamma_{1b}}b$, the master equation in the interaction picture is:

$$\frac{\mathrm{d}\rho}{\mathrm{d}t} = \gamma_{1b}\left(a\rho a^\dagger - \frac{1}{2}\{a^\dagger a, \rho\} + b\rho b^\dagger - \frac{1}{2}\{b^\dagger b, \rho\}\right).$$

Using $\langle\hat{\mathcal{O}}\rangle = \mathrm{Tr}\left\{\rho\hat{\mathcal{O}}\right\}$ and the master equation, we can calculate the evolution of the moments

12.2.1 *Some examples*

Notice that $[N_i, a] = -a\delta_{i,a}, [N_i, b] = -b\delta_{i,b}$, where $N_a = a^\dagger a, N_b = b^\dagger b$. Then

$$\begin{aligned}\frac{\mathrm{d}}{\mathrm{d}t}\langle N_i\rangle =& \frac{\mathrm{d}}{\mathrm{d}t}\mathrm{Tr}\left\{\rho N_i\right\} = \mathrm{Tr}\left\{N_i\frac{\mathrm{d}\rho}{\mathrm{d}t}\right\}\\ =&\gamma_{1b}\mathrm{Tr}\left\{N_i\left(a\rho a^\dagger - \frac{1}{2}\{N_a,\rho\} + b\rho b^\dagger - \frac{1}{2}\{N_b,\rho\}\right)\right\}\\ =&\gamma_{1b}\mathrm{Tr}\left\{a^\dagger N_i a\rho - N_i N_a\rho + b^\dagger N_i b\rho - N_i N_b\rho\right\},\end{aligned}$$

where we use the cyclic property of the trace and commutation relationships[1]. We focus now on $i = a$, the other case is analogous:

[1] $[N_i, N_j] = 0$

$$\begin{aligned}\frac{\mathrm{d}}{\mathrm{d}t}\langle N_a\rangle =&\gamma_{1b}\mathrm{Tr}\left\{a^\dagger N_a a\rho - N_a N_a\rho + b^\dagger N_a b\rho - N_a N_b,\rho\right\}\\ =&\gamma_{1b}\mathrm{Tr}\left\{a^\dagger(aN_a - a)\rho - N_a N_a\rho + N_a b^\dagger b\rho - N_a N_b,\rho\right\}\\ =&-\gamma_{1b}\mathrm{Tr}\left\{a^\dagger a\rho\right\} = -\gamma_{1b}\langle N_a\rangle.\end{aligned}$$

Similarly $\frac{\mathrm{d}}{\mathrm{d}t}\langle N_b\rangle = -\gamma_{1b}\langle N_b\rangle$. The rest of the first and second moments are calculated in a similar manner, for completeness, we list them below, but for brevity, we omit the steps of the calculations.

First moments

$$\frac{\mathrm{d}}{\mathrm{d}t}\left\langle a^\dagger b\right\rangle = -\gamma_{1b}\left\langle a^\dagger b\right\rangle \qquad \frac{\mathrm{d}}{\mathrm{d}t}\left\langle N\right\rangle = -\gamma_{1b}\left\langle N\right\rangle,$$
$$\frac{\mathrm{d}}{\mathrm{d}t}\left\langle b^\dagger a\right\rangle = -\gamma_{1b}\left\langle b^\dagger a\right\rangle \qquad \frac{\mathrm{d}}{\mathrm{d}t}\left\langle S_i\right\rangle = -\gamma_{1b}\left\langle S_i\right\rangle,$$
$$\frac{\mathrm{d}}{\mathrm{d}t}\left\langle N_i\right\rangle = -\gamma_{1b}\left\langle N_i\right\rangle.$$

Second moments

$$\frac{\mathrm{d}}{\mathrm{d}t}\left\langle N_i^2\right\rangle = -2\gamma_{1b}\left\langle N_i^2\right\rangle + \gamma_{1b}\left\langle N_i\right\rangle \qquad \frac{\mathrm{d}}{\mathrm{d}t}\left\langle N_aN_b\right\rangle = -2\gamma_{1b}\left\langle N_aN_b\right\rangle,$$
$$\frac{\mathrm{d}}{\mathrm{d}t}\left\langle a^\dagger a^\dagger bb\right\rangle = -2\gamma_{1b}\left\langle a^\dagger a^\dagger bb\right\rangle \qquad \frac{\mathrm{d}}{\mathrm{d}t}\left\langle aab^\dagger b^\dagger\right\rangle = -2\gamma_{1b}\left\langle aab^\dagger b^\dagger\right\rangle.$$

From which the spin second moments are

$$\begin{aligned}
\frac{\mathrm{d}}{\mathrm{d}t}\left\langle S_z^2\right\rangle =& \frac{1}{4}\frac{\mathrm{d}}{\mathrm{d}t}\left\langle N_a^2 + N_b^2 - 2N_aN_b\right\rangle \\
=& -\frac{1}{2}\gamma_{1b}\left\langle N_a^2 + N_b^2 - 2N_aN_b\right\rangle + \frac{1}{4}\gamma_{1b}\left\langle N_a + N_b\right\rangle \\
=& -2\gamma_{1b}\left\langle S_z^2\right\rangle + \gamma_{1b}\frac{\langle N\rangle}{4}, \\
\frac{\mathrm{d}}{\mathrm{d}t}\left\langle S_x^2\right\rangle =& \frac{1}{4}\frac{\mathrm{d}}{\mathrm{d}t}\left\langle a^\dagger a^\dagger bb + aab^\dagger b^\dagger + N_abb^\dagger + N_baa^\dagger\right\rangle \\
=& \frac{1}{4}\frac{\mathrm{d}}{\mathrm{d}t}\left\langle a^\dagger a^\dagger bb + aab^\dagger b^\dagger + 2N_aN_b + N\right\rangle \\
=& -\frac{\gamma_{1b}}{2}\left\langle a^\dagger a^\dagger bb + aab^\dagger b^\dagger + 2N_aN_b\right\rangle - \frac{\gamma_{1b}}{4}\left\langle N\right\rangle \\
=& -2\gamma_{1b}\left\langle S_x^2\right\rangle + \gamma_{1b}\frac{\langle N\rangle}{4}.
\end{aligned}$$

Time-Evolution It's clear from the above equations that $\langle N\rangle = N_0e^{-\gamma_{1b}t}$ and $\langle S_i\rangle = \langle S_i(0)\rangle\, e^{-\gamma_{1b}t}$, where we introduce $N_0 = \langle N(0)\rangle$. We then have:

$$\frac{\mathrm{d}}{\mathrm{d}t}\left\langle S_z^2\right\rangle + 2\gamma_{1b}\left\langle S_z^2\right\rangle = \frac{\gamma_{1b}N_0}{4}e^{-\gamma_{1b}t}.$$

This has as solution:

$$\begin{aligned}
\left\langle S_z^2(t)\right\rangle =& e^{-2\gamma_{1b}t}\left(\left\langle S_z^2(0)\right\rangle + \frac{N_0}{4}(e^{\gamma_{1b}t} - 1)\right) \\
\mathrm{Var}\left(S_z(t)\right) =& e^{-2\gamma_{1b}t}\left(\mathrm{Var}\left(S_z(0)\right) + \frac{N_0}{4}(e^{\gamma_{1b}t} - 1)\right).
\end{aligned}$$

This leads us to an expression for the variance in terms of the current atom number:

$$\mathrm{Var}\left(S_z(t)\right) = \mathrm{Var}\left(S_z(0)\right)e^{-2\gamma_{1b}t} + \frac{\langle N\rangle}{4} - \frac{\langle N\rangle}{4}e^{-\gamma_{1b}t}. \tag{12.1}$$

Notice that this can be written in terms of the number squeezing $\xi_N^2 = \frac{4}{\langle N(t)\rangle}\mathrm{Var}\left(S_z(t)\right)$ as

$$\xi_N^2(t) - 1 = (\xi_N^2(0) - 1)e^{-\gamma_{1b}t}. \tag{12.2}$$

List of Figures

Bibliography

[1] Daniel A. Steck. Rubidium 87 D Line Data. Technical report, 2015. URL http://steck.us/alkalidata.

[2] I. I. Rabi. Space Quantization in a Gyrating Magnetic Field. *Physical Review*, 51(8):652–654, April 1937. doi: 10.1103/PhysRev.51.652. URL https://link.aps.org/doi/10.1103/PhysRev.51.652. Publisher: American Physical Society.

[3] I. I. Rabi, J. R. Zacharias, S. Millman, and P. Kusch. A New Method of Measuring Nuclear Magnetic Moment. *Physical Review*, 53(4):318–318, February 1938. doi: 10.1103/PhysRev.53.318. URL https://link.aps.org/doi/10.1103/PhysRev.53.318. Publisher: American Physical Society.

[4] Lyons Harold and Benjamin F. Husten. Atomic clock, January 1955. URL https://patents.google.com/patent/US2699503A/en.

[5] Norman F. Ramsey. A Molecular Beam Resonance Method with Separated Oscillating Fields. *Physical Review*, 78(6):695–699, June 1950. doi: 10.1103/PhysRev.78.695. URL https://link.aps.org/doi/10.1103/PhysRev.78.695. Publisher: American Physical Society.

[6] D. B. Sullivan. Time and frequency measurement at NIST: The first 100 years. 2001.

[7] SI unit of time (second). working_paper, 1967. URL https://www.bipm.org/en/-/resolution-cgpm-13-1.

[8] C. Salomon, J. Dalibard, W. D. Phillips, A. Clairon, and S. Guellati. Laser Cooling of Cesium Atoms Below 3 K. *Europhysics Letters*, 12(8):683, August 1990. ISSN 0295-5075. doi: 10.1209/0295-5075/12/8/003. URL https://dx.doi.org/10.1209/0295-5075/12/8/003.

[9] A. Clairon, P. Laurent, G. Santarelli, S. Ghezali, S.N. Lea, and M. Bahoura. A cesium fountain frequency standard: preliminary results. *IEEE Transactions on Instrumentation and Measurement*, 44(2):128–131, April 1995. ISSN 1557-9662. doi: 10.1109/19.377790. Conference Name: IEEE Transactions on Instrumentation and Measurement.

[10] W. F. McGrew, X. Zhang, R. J. Fasano, S. A. Schäffer, K. Beloy, D. Nicolodi, R. C. Brown, N. Hinkley, G. Milani, M. Schioppo, T. H. Yoon, and A. D. Ludlow. Atomic clock performance enabling geodesy below the centimetre level. *Nature*, 564(7734):87–90, December 2018. ISSN 1476-4687. doi: 10.1038/s41586-018-0738-2. URL https://www.nature.com/articles/s41586-018-0738-2. Number: 7734 Publisher: Nature Publishing Group.

[11] B. J. Bloom, T. L. Nicholson, J. R. Williams, S. L. Campbell, M. Bishof, X. Zhang, W. Zhang, S. L. Bromley, and J. Ye. An optical lattice clock with accuracy and stability at the 10e-18 level. *Nature*, 506(7486):71–75, February 2014. ISSN 1476-4687. doi: 10.1038/nature12941. URL https://www.nature.com/articles/nature12941. Number: 7486 Publisher: Nature Publishing Group.

[12] S. M. Brewer, J.-S. Chen, A. M. Hankin, E. R. Clements, C. W. Chou, D. J. Wineland, D. B. Hume, and D. R. Leibrandt. $^{27}{\mathrm{Al}}^{+}$ Quantum-Logic Clock with a Systematic Uncertainty below ${10}^{\ensuremath{-}18}$. *Physical Review Letters*, 123(3):033201, July 2019. doi: 10.1103/PhysRevLett.123.033201. URL https://link.aps.org/doi/10.1103/PhysRevLett.123.033201. Publisher: American Physical Society.

[13] M. S. Safronova, D. Budker, D. DeMille, Derek F. Jackson Kimball, A. Derevianko, and Charles W. Clark. Search for new physics with atoms and molecules. *Reviews of Modern Physics*, 90(2): 025008, June 2018. doi: 10.1103/RevModPhys.90.025008. URL https://link.aps.org/doi/10.1103/RevModPhys.90.025008. Publisher: American Physical Society.

[14] S. Kang, M. Gharavipour, C. Affolderbach, F. Gruet, and G. Mileti. Demonstration of a high-performance pulsed optically pumped Rb clock based on a compact magnetron-type microwave cavity. *Journal of Applied Physics*, 117(10):104510, March 2015. ISSN 0021-8979, 1089-7550. doi: 10.1063/1.4914493. URL https://pubs.aip.org/jap/article/117/10/104510/382418/Demonstration-of-a-high-performance-pulsed.

[15] Stella Torres Müller, Daniel Varela Magalhães, Renato Ferracini Alves, and Vanderlei Salvador Bagnato. Compact frequency standard based on an intracavity sample of cold cesium atoms. *JOSA B*, 28(11):2592–2596, November 2011. ISSN 1520-8540. doi: 10.1364/JOSAB.28.002592. URL https://opg.optica.org/josab/abstract.cfm?uri=josab-28-11-2592. Publisher: Optica Publishing Group.

[16] F. X. Esnault, N. Rossetto, D. Holleville, J. Delporte, and N. Dimarcq. HORACE: A compact cold atom clock for Galileo. *Advances in Space Research*, 47(5):854–858, March 2011. ISSN 0273-1177. doi: 10.1016/j.asr.2010.12.012. URL https://www.sciencedirect.com/science/article/pii/S0273117710008124.

[17] S. Micalizio, C. E. Calosso, A. Godone, and F. Levi. Metrological characterization of the pulsed Rb clock with optical detection. *Metrologia*, 49(4):425, May 2012. ISSN 0026-1394. doi: 10.1088/0026-1394/49/4/425. URL https://dx.doi.org/10.1088/0026-1394/49/4/425. Publisher: IOP Publishing.

[18] Thejesh Bandi, Christoph Affolderbach, Camillo Stefanucci, Francesco Merli, Anja K. Skrivervik, and Gaetano Mileti. Compact high-performance continuous-wave double-resonance rubidium standard with 1.4 × 10e-13 -1/2 stability. *IEEE Transactions on Ultrasonics, Ferroelectrics, and Frequency Control*, 61(11):1769–1778, November 2014. ISSN 1525-8955. doi: 10.1109/TUFFC.2013.005955. Conference Name: IEEE Transactions on Ultrasonics, Ferroelectrics, and Frequency Control.

[19] Ch.J. Bordé. Atomic interferometry with internal state labelling. *Physics Letters A*, 140(1-2):10–12, September 1989. ISSN 03759601. doi: 10.1016/0375-9601(89)90537-9. URL https://linkinghub.elsevier.com/retrieve/pii/0375960189905379.

[20] J. Robert, Ch Miniatura, S. Le Boiteux, J. Reinhardt, V. Bocvarski, and J. Baudon. Atomic Interferometry with Metastable Hydrogen Atoms. *Europhysics Letters*, 16(1):29, September 1991. ISSN 0295-5075. doi: 10.1209/0295-5075/16/1/006. URL https://dx.doi.org/10.1209/0295-5075/16/1/006.

[21] O. Carnal and J. Mlynek. Young's double-slit experiment with atoms: A simple atom interferometer. *Physical Review Letters*, 66(21):2689–2692, May 1991. doi: 10.1103/PhysRevLett.66.2689. URL https://link.aps.org/doi/10.1103/PhysRevLett.66.2689. Publisher: American Physical Society.

[22] David W. Keith, Christopher R. Ekstrom, Quentin A. Turchette, and David E. Pritchard. An interferometer for atoms. *Physical Review Letters*, 66(21):2693–2696, May 1991. doi: 10.1103/PhysRevLett.

66.2693. URL https://link.aps.org/doi/10.1103/PhysRevLett.66.2693. Publisher: American Physical Society.

[23] F. Riehle, Th. Kisters, A. Witte, J. Helmcke, and Ch. J. Bordé. Optical Ramsey spectroscopy in a rotating frame: Sagnac effect in a matter-wave interferometer. *Physical Review Letters*, 67(2):177–180, July 1991. doi: 10.1103/PhysRevLett.67.177. URL https://link.aps.org/doi/10.1103/PhysRevLett.67.177. Publisher: American Physical Society.

[24] Mark Kasevich and Steven Chu. Atomic interferometry using stimulated Raman transitions. *Physical Review Letters*, 67(2):181–184, July 1991. doi: 10.1103/PhysRevLett.67.181. URL https://link.aps.org/doi/10.1103/PhysRevLett.67.181. Publisher: American Physical Society.

[25] Remi Geiger, Arnaud Landragin, Sébastien Merlet, and Franck Pereira Dos Santos. High-accuracy inertial measurements with cold-atom sensors. *AVS Quantum Science*, 2(2):024702, June 2020. ISSN 2639-0213. doi: 10.1116/5.0009093. URL https://pubs.aip.org/aqs/article/2/2/024702/997275/High-accuracy-inertial-measurements-with-cold-atom.

[26] Alexander D. Cronin, Jörg Schmiedmayer, and David E. Pritchard. Optics and interferometry with atoms and molecules. *Reviews of Modern Physics*, 81(3):1051–1129, July 2009. doi: 10.1103/RevModPhys.81.1051. URL https://link.aps.org/doi/10.1103/RevModPhys.81.1051. Publisher: American Physical Society.

[27] Kai Bongs, Michael Holynski, Jamie Vovrosh, Philippe Bouyer, Gabriel Condon, Ernst Rasel, Christian Schubert, Wolfgang P. Schleich, and Albert Roura. Taking atom interferometric quantum sensors from the laboratory to real-world applications. *Nature Reviews Physics*, 1(12):731–739, December 2019. ISSN 2522-5820. doi: 10.1038/s42254-019-0117-4. URL https://www.nature.com/articles/s42254-019-0117-4. Number: 12 Publisher: Nature Publishing Group.

[28] Jakob Reichel and Vladan Vuletić, editors. *Atom Chips*. Wiley, 1 edition, February 2011. ISBN 978-3-527-40755-2 978-3-527-63335-7. doi: 10.1002/9783527633357. URL https://onlinelibrary.wiley.com/doi/book/10.1002/9783527633357.

[29] Friedemann Reinhard. Design and construction of an atomic clock on an atom chip. 2008.

[30] Mark Keil, Omer Amit, Shuyu Zhou, David Groswasser, Yonathan Japha, and Ron Folman. Fifteen years of cold matter on the atom chip: promise, realizations, and prospects. *Journal of Modern Optics*, 63(18):1840–1885, October 2016. ISSN 0950-0340, 1362-3044. doi: 10.1080/09500340.2016.1178820. URL https://www.tandfonline.com/doi/full/10.1080/09500340.2016.1178820.

[31] H. Ott, J. Fortagh, G. Schlotterbeck, A. Grossmann, and C. Zimmermann. Bose-Einstein condensation in a surface microtrap. *Physical Review Letters*, 87(23):230401, December 2001. ISSN 0031-9007. doi: 10.1103/PhysRevLett.87.230401.

[32] W. Hänsel, P. Hommelhoff, T. W. Hänsch, and J. Reichel. Bose-Einstein condensation on a microelectronic chip. *Nature*, 413(6855):498–501, October 2001. ISSN 0028-0836. doi: 10.1038/35097032.

[33] J. J. P. van Es. *Bose-Einstein condensates in radio-frequency-dressed potentials on an atom chip*. Amsterdam, 2009. ISBN 978-90-5776-186-7. URL https://dare.uva.nl/search?identifier=71bdae34-effb-4e07-a652-a5653559d1ff.

[34] Peter Krüger, Albrecht Haase, Ron Folman, and Jörg Schmiedmayer. Quantum Information Processing with Neutral Atoms on Atom Chips. In *Quantum Information Processing*, pages 257–265. John Wiley & Sons, Ltd, 2003. ISBN 978-3-527-60354-1. doi: 10.1002/3527603549.ch21. URL https://onlinelibrary.wiley.com/doi/abs/10.1002/3527603549.ch21. Section: 21 _eprint: https://onlinelibrary.wiley.com/doi/pdf/10.1002/3527603549.ch21.

[35] Carlos L. Garrido Alzar. Compact chip-scale guided cold atom gyrometers for inertial navigation: Enabling technologies and design study. *AVS Quantum Science*, 1(1):014702, December 2019. ISSN 2639-0213. doi: 10.1116/1.5120348. URL https://pubs.aip.org/aqs/article/1/1/014702/997236/Compact-chip-scale-guided-cold-atom-gyrometers-for.

[36] Christian Deutsch. *Trapped atom clock on a chip : identical spin rotation effects in an ultracold trapped atomic clock*. These de doctorat, Paris 6, January 2011. URL https://www.theses.fr/2011PA066742.

[37] P. Rosenbusch. Magnetically trapped atoms for compact atomic clocks. *Applied Physics B*, 95(2): 227–235, May 2009. ISSN 1432-0649. doi: 10.1007/s00340-009-3451-x. URL https://doi.org/10.1007/s00340-009-3451-x.

[38] Gregory H. Wannier. *Statistical physics*. Dover books on physics and chemistry. Dover Publications, New York, 1987. ISBN 978-0-486-65401-0.

[39] D. M. Harber, H. J. Lewandowski, J. M. McGuirk, and E. A. Cornell. Effect of cold collisions on spin coherence and resonance shifts in a magnetically trapped ultracold gas. *Physical Review A*, 66 (5):053616, November 2002. doi: 10.1103/PhysRevA.66.053616. URL https://link.aps.org/doi/10.1103/PhysRevA.66.053616. Publisher: American Physical Society.

[40] H. M. Wiseman and G. J. Milburn. *Quantum measurement and control*. Cambridge University Press, Cambridge, UK ; New York, 2010. ISBN 978-0-521-80442-4. OCLC: ocn434744599.

[41] Luca Pezzè, Augusto Smerzi, Markus K. Oberthaler, Roman Schmied, and Philipp Treutlein. Quantum metrology with nonclassical states of atomic ensembles. *Reviews of Modern Physics*, 90(3):035005, September 2018. doi: 10.1103/RevModPhys.90.035005. URL https://link.aps.org/doi/10.1103/RevModPhys.90.035005. Publisher: American Physical Society.

[42] Vittorio Giovannetti, Seth Lloyd, and Lorenzo Maccone. Quantum Metrology. *Physical Review Letters*, 96(1):010401, January 2006. doi: 10.1103/PhysRevLett.96.010401. URL https://link.aps.org/doi/10.1103/PhysRevLett.96.010401. Publisher: American Physical Society.

[43] G. Santarelli, Ph. Laurent, P. Lemonde, A. Clairon, A. G. Mann, S. Chang, A. N. Luiten, and C. Salomon. Quantum Projection Noise in an Atomic Fountain: A High Stability Cesium Frequency Standard. *Physical Review Letters*, 82(23):4619–4622, June 1999. doi: 10.1103/PhysRevLett.82.4619. URL https://link.aps.org/doi/10.1103/PhysRevLett.82.4619. Publisher: American Physical Society.

[44] Luca Pezzé and Augusto Smerzi. Entanglement, Nonlinear Dynamics, and the Heisenberg Limit. *Physical Review Letters*, 102(10):100401, March 2009. doi: 10.1103/PhysRevLett.102.100401. URL https://link.aps.org/doi/10.1103/PhysRevLett.102.100401. Publisher: American Physical Society.

[45] Jun J. Sakurai and Jim Napolitano. *Modern quantum mechanics*. Always learning. Pearson, Harlow, 2. ed., new internat. ed edition, 2014. ISBN 978-1-292-02410-3.

[46] Jiazhong Hu, Wenlan Chen, Zachary Vendeiro, Hao Zhang, and Vladan Vuletić. Entangled collective-spin states of atomic ensembles under nonuniform atom-light interaction. *Physical Review A*, 92(6):063816, December 2015. doi: 10.1103/PhysRevA.92.063816. URL https://link.aps.org/doi/10.1103/PhysRevA.92.063816. Publisher: American Physical Society.

[47] Jonathan P. Dowling, G. S. Agarwal, and Wolfgang P. Schleich. Wigner distribution of a general angular-momentum state: Applications to a collection of two-level atoms. *Physical Review A*, 49(5): 4101–4109, May 1994. doi: 10.1103/PhysRevA.49.4101. URL https://link.aps.org/doi/10.1103/PhysRevA.49.4101. Publisher: American Physical Society.

[48] L.-M. Duan, J. I. Cirac, and P. Zoller. Quantum entanglement in spinor Bose-Einstein condensates. *Physical Review A*, 65(3):033619, February 2002. doi: 10.1103/PhysRevA.65.033619. URL https://link.aps.org/doi/10.1103/PhysRevA.65.033619. Publisher: American Physical Society.

[49] Yun Li, Y. Castin, and A. Sinatra. Optimum Spin Squeezing in Bose-Einstein Condensates with Particle Losses. *Physical Review Letters*, 100(21):210401, May 2008. doi: 10.1103/PhysRevLett.100.210401. URL https://link.aps.org/doi/10.1103/PhysRevLett.100.210401. Publisher: American Physical Society.

[50] Manuel H. Muñoz-Arias, Ivan H. Deutsch, and Pablo M. Poggi. Phase-Space Geometry and Optimal State Preparation in Quantum Metrology with Collective Spins. *PRX Quantum*, 4(2):020314, April 2023. ISSN 2691-3399. doi: 10.1103/PRXQuantum.4.020314. URL https://link.aps.org/doi/10.1103/PRXQuantum.4.020314.

[51] D. J. Wineland, J. J. Bollinger, W. M. Itano, F. L. Moore, and D. J. Heinzen. Spin squeezing and reduced quantum noise in spectroscopy. *Physical Review A*, 46(11):R6797–R6800, December 1992. doi: 10.1103/PhysRevA.46.R6797. URL https://link.aps.org/doi/10.1103/PhysRevA.46.R6797. Publisher: American Physical Society.

[52] D. J. Wineland, J. J. Bollinger, W. M. Itano, and D. J. Heinzen. Squeezed atomic states and projection noise in spectroscopy. *Physical Review A*, 50(1):67–88, July 1994. doi: 10.1103/PhysRevA.50.67. URL https://link.aps.org/doi/10.1103/PhysRevA.50.67. Publisher: American Physical Society.

[53] Masahiro Kitagawa and Masahito Ueda. Squeezed spin states. *Physical Review A*, 47(6):5138–5143, June 1993. doi: 10.1103/PhysRevA.47.5138. URL https://link.aps.org/doi/10.1103/PhysRevA.47.5138. Publisher: American Physical Society.

[54] Roman Schmied, Jean-Daniel Bancal, Baptiste Allard, Matteo Fadel, Valerio Scarani, Philipp Treutlein, and Nicolas Sangouard. Bell correlations in a Bose-Einstein condensate. *Science*, 352(6284):441–444, April 2016. doi: 10.1126/science.aad8665. URL https://www.science.org/doi/10.1126/science.aad8665. Publisher: American Association for the Advancement of Science.

[55] W. Muessel, H. Strobel, D. Linnemann, D. B. Hume, and M. K. Oberthaler. Scalable Spin Squeezing for Quantum-Enhanced Magnetometry with Bose-Einstein Condensates. *Physical Review Letters*, 113(10):103004, September 2014. doi: 10.1103/PhysRevLett.113.103004. URL https://link.aps.org/doi/10.1103/PhysRevLett.113.103004. Publisher: American Physical Society.

[56] Caspar F. Ockeloen, Roman Schmied, Max F. Riedel, and Philipp Treutlein. Quantum Metrology with a Scanning Probe Atom Interferometer. *Physical Review Letters*, 111(14):143001, October 2013. doi: 10.1103/PhysRevLett.111.143001. URL https://link.aps.org/doi/10.1103/PhysRevLett.111.143001. Publisher: American Physical Society.

[57] A. Sørensen, L.-M. Duan, J. I. Cirac, and P. Zoller. Many-particle entanglement with Bose–Einstein condensates. *Nature*, 409(6816):63–66, January 2001. ISSN 1476-4687. doi: 10.1038/35051038. URL https://www.nature.com/articles/35051038. Number: 6816 Publisher: Nature Publishing Group.

[58] C. Gross, T. Zibold, E. Nicklas, J. Estève, and M. K. Oberthaler. Nonlinear atom interferometer surpasses classical precision limit. *Nature*, 464(7292):1165–1169, April 2010. ISSN 1476-4687. doi: 10.1038/nature08919. URL https://www.nature.com/articles/nature08919. Number: 7292 Publisher: Nature Publishing Group.

[59] Max F. Riedel, Pascal Böhi, Yun Li, Theodor W. Hänsch, Alice Sinatra, and Philipp Treutlein. Atom-chip-based generation of entanglement for quantum metrology. *Nature*, 464(7292):1170–1173, April 2010. ISSN 1476-4687. doi: 10.1038/nature08988. URL https://www.nature.com/articles/nature08988. Number: 7292 Publisher: Nature Publishing Group.

[60] W. Muessel, H. Strobel, D. Linnemann, T. Zibold, B. Julia-Díaz, and M. K. Oberthaler. Twist-and-turn spin squeezing in Bose-Einstein condensates. *Physical Review A*, 92(2):023603, August 2015. doi: 10.1103/PhysRevA.92.023603. URL https://link.aps.org/doi/10.1103/PhysRevA.92.023603. Publisher: American Physical Society.

[61] Zeyang Li, Boris Braverman, Simone Colombo, Chi Shu, Akio Kawasaki, Albert F. Adiyatullin, Edwin Pedrozo-Peñafiel, Enrique Mendez, and Vladan Vuletić. Collective Spin-Light and Light-Mediated Spin-Spin Interactions in an Optical Cavity. *PRX Quantum*, 3(2):020308, April 2022. ISSN 2691-3399. doi: 10.1103/PRXQuantum.3.020308. URL https://link.aps.org/doi/10.1103/PRXQuantum.3.020308.

[62] Krzysztof Pawłowski, Jérôme Estève, Jakob Reichel, and Alice Sinatra. Limits of atomic entanglement by cavity feedback: From weak to strong coupling. *Europhysics Letters*, 113(3):34005, February 2016. ISSN 0295-5075. doi: 10.1209/0295-5075/113/34005. URL https://dx.doi.org/10.1209/0295-5075/113/34005. Publisher: EDP Sciences, IOP Publishing and Società Italiana di Fisica.

[63] D. F. Walls and G. J. Milburn. *Quantum optics*. Springer-Verlag, Berlin ; New York, springer study ed edition, 1995. ISBN 978-3-540-58831-3.

[64] Mingxia Zhan, Fang Jia, Jiali Huang, Huan Zhang, and Liyun Hu. Representation of the coherent state for a beam splitter operator and its applications. *Communications in Theoretical Physics*, 74 (3):035101, March 2022. ISSN 0253-6102, 1572-9494. doi: 10.1088/1572-9494/ac5244. URL https://iopscience.iop.org/article/10.1088/1572-9494/ac5244.

[65] Meng-Zi Huang, Jose Alberto de la Paz, Tommaso Mazzoni, Konstantin Ott, Peter Rosenbusch, Alice Sinatra, Carlos L. Garrido Alzar, and Jakob Reichel. Observing Spin-Squeezed States under Spin-Exchange Collisions for a Second. *PRX Quantum*, 4(2):020322, May 2023. doi: 10.1103/PRXQuantum.4.020322. URL https://link.aps.org/doi/10.1103/PRXQuantum.4.020322. Publisher: American Physical Society.

[66] Boris Braverman, Akio Kawasaki, Edwin Pedrozo-Peñafiel, Simone Colombo, Chi Shu, Zeyang Li, Enrique Mendez, Megan Yamoah, Leonardo Salvi, Daisuke Akamatsu, Yanhong Xiao, and Vladan Vuletić. Near-Unitary Spin Squeezing in $^{171}\mathrm{Yb}$. *Physical Review Letters*, 122(22): 223203, June 2019. doi: 10.1103/PhysRevLett.122.223203. URL https://link.aps.org/doi/10.1103/PhysRevLett.122.223203. Publisher: American Physical Society.

[67] Meng-Zi Huang. *Spin squeezing and spin dynamics in a trapped-atom clock*. phdthesis, Sorbonne Université, September 2019. URL https://theses.hal.science/tel-02356949.

[68] Boris Braverman, Akio Kawasaki, and Vladan Vuletić. Impact of non-unitary spin squeezing on atomic clock performance. *New Journal of Physics*, 20(10):103019, October 2018. ISSN 1367-2630. doi: 10.1088/1367-2630/aae563. URL https://iopscience.iop.org/article/10.1088/1367-2630/aae563.

[69] Xiaoguang Wang and Barry C. Sanders. Relations between bosonic quadrature squeezing and atomic spin squeezing. *Physical Review A*, 68(3):033821, September 2003. ISSN 1050-2947, 1094-1622. doi: 10.1103/PhysRevA.68.033821. URL https://link.aps.org/doi/10.1103/PhysRevA.68.033821.

[70] Lars Bojer Madsen and Klaus Mølmer. Spin squeezing and precision probing with light and samples of atoms in the Gaussian description. *Physical Review A*, 70(5):052324, November 2004. ISSN 1050-2947, 1094-1622. doi: 10.1103/PhysRevA.70.052324. URL https://link.aps.org/doi/10.1103/PhysRevA.70.052324.

[71] Yun Li, P. Treutlein, J. Reichel, and A. Sinatra. Spin squeezing in a bimodal condensate: spatial dynamics and particle losses. *The European Physical Journal B*, 68(3):365–381, April 2009. ISSN 1434-6028, 1434-6036. doi: 10.1140/epjb/e2008-00472-6. URL http://link.springer.com/10.1140/epjb/e2008-00472-6.

[72] C. Deutsch, F. Ramirez-Martinez, C. Lacroûte, F. Reinhard, T. Schneider, J. N. Fuchs, F. Piéchon, F. Laloë, J. Reichel, and P. Rosenbusch. Spin Self-Rephasing and Very Long Coherence Times in a Trapped Atomic Ensemble. *Physical Review Letters*, 105(2):020401, July 2010. doi: 10.1103/PhysRevLett.105.020401. URL https://link.aps.org/doi/10.1103/PhysRevLett.105.020401. Publisher: American Physical Society.

[73] R. Szmuk, V. Dugrain, W. Maineult, J. Reichel, and P. Rosenbusch. Stability of a trapped-atom clock on a chip. *Physical Review A*, 92(1):012106, July 2015. doi: 10.1103/PhysRevA.92.012106. URL https://link.aps.org/doi/10.1103/PhysRevA.92.012106. Publisher: American Physical Society.

[74] Konstantin Ott, Sebastien Garcia, Ralf Kohlhaas, Klemens Schüppert, Peter Rosenbusch, Romain Long, and Jakob Reichel. Millimeter-long fiber Fabry-Perot cavities. *Optics Express*, 24(9):9839–9853, May 2016. ISSN 1094-4087. doi: 10.1364/OE.24.009839. URL https://opg.optica.org/oe/abstract.cfm?uri=oe-24-9-9839. Publisher: Optica Publishing Group.

[75] Konstantin Ott. *Towards a squeezing-enhanced atomic clock on a chip*. phdthesis, Université Pierre et Marie Curie - Paris VI, September 2016. URL https://theses.hal.science/tel-01452767.

[76] Sung Jong Park, Jiho Noh, and Jongchul Mun. Cold atomic beam from a two-dimensional magneto-optical trap with two-color pushing laser beams. *Optics Communications*, 285(19):3950–3954, September 2012. ISSN 0030-4018. doi: 10.1016/j.optcom.2012.05.041. URL https://www.sciencedirect.com/science/article/pii/S0030401812004737.

[77] G. Reinaudi, T. Lahaye, Z. Wang, and D. Guéry-Odelin. Strong saturation absorption imaging of dense clouds of ultracold atoms. *Optics Letters*, 32(21):3143–3145, November 2007. ISSN 1539-4794. doi: 10.1364/OL.32.003143. URL https://opg.optica.org/ol/abstract.cfm?uri=ol-32-21-3143. Publisher: Optica Publishing Group.

[78] Théo Laudat. *Étude du phénomène de compression de spin dans un condensat de Bose-Einstein piégé sur microcircuit*. phdthesis, Université Paris sciences et lettres, October 2017. URL https://theses.hal.science/tel-01688752.

[79] Fernando Ramirez-Martinez, Michel Lours, Peter Rosenbusch, Friedemann Reinhard, and Jakob Reichel. Low-phase-noise frequency synthesizer for the trapped atom clock on a chip. *IEEE Transactions on Ultrasonics, Ferroelectrics, and Frequency Control*, 57(1):88–93, January 2010. ISSN 1525-8955. doi: 10.1109/TUFFC.2010.1383. Conference Name: IEEE Transactions on Ultrasonics, Ferroelectrics, and Frequency Control.

[80] Paul Stoffregen. CoreMark - CPU Performance Benchmark, September 2023. URL https://github.com/PaulStoffregen/CoreMark. original-date: 2019-08-05T09:41:29Z.

[81] Paul Stoffregen. FreqCount, September 2023. URL https://github.com/PaulStoffregen/FreqCount. original-date: 2014-06-05T16:57:50Z.

[82] E. Brion, L. H. Pedersen, and K. Mølmer. Adiabatic elimination in a lambda system. *Journal of Physics A: Mathematical and Theoretical*, 40(5):1033, January 2007. ISSN 1751-8121. doi: 10.1088/1751-8113/40/5/011. URL https://dx.doi.org/10.1088/1751-8113/40/5/011.

[83] L. M. K. Vandersypen and I. L. Chuang. NMR techniques for quantum control and computation. *Reviews of Modern Physics*, 76(4):1037–1069, January 2005. doi: 10.1103/RevModPhys.76.1037. URL https://link.aps.org/doi/10.1103/RevModPhys.76.1037. Publisher: American Physical Society.

[84] Hai-Ning Wu, Cheng Zhang, Jie Song, Yan Xia, and Zhi-Cheng Shi. Composite pulses for optimal robust control in two-level systems. *Physical Review A*, 107(2):023103, February 2023. doi: 10.1103/PhysRevA.107.023103. URL https://link.aps.org/doi/10.1103/PhysRevA.107.023103. Publisher: American Physical Society.

[85] X. Baillard, A. Gauguet, S. Bize, P. Lemonde, Ph. Laurent, A. Clairon, and P. Rosenbusch. Interference-filter-stabilized external-cavity diode lasers. *Optics Communications*, 266(2):609–613, October 2006. ISSN 0030-4018. doi: 10.1016/j.optcom.2006.05.011. URL https://www.sciencedirect.com/science/article/pii/S0030401806004561.

[86] Clément Lacroûte. *Développement d'une horloge atomique sur puce à atomes : optimisation de la durée de cohérence et caractérisation préliminaire.* phdthesis, Université Pierre et Marie Curie - Paris VI, January 2010. URL https://theses.hal.science/tel-00528925.

[87] Serge Haroche and Francis Hartmann. Theory of Saturated-Absorption Line Shapes. *Physical Review A*, 6(4):1280–1300, October 1972. doi: 10.1103/PhysRevA.6.1280. URL https://link.aps.org/doi/10.1103/PhysRevA.6.1280. Publisher: American Physical Society.

[88] D. J. McCarron, S. A. King, and S. L. Cornish. Modulation transfer spectroscopy in atomic rubidium. *Measurement Science and Technology*, 19(10):105601, August 2008. ISSN 0957-0233. doi: 10.1088/0957-0233/19/10/105601. URL https://dx.doi.org/10.1088/0957-0233/19/10/105601.

[89] Jon H. Shirley. Modulation transfer processes in optical heterodyne saturation spectroscopy. *Optics Letters*, 7(11):537–539, November 1982. ISSN 1539-4794. doi: 10.1364/OL.7.000537. URL https://opg.optica.org/ol/abstract.cfm?uri=ol-7-11-537. Publisher: Optica Publishing Group.

[90] Sébastien Garcia. *Interfaces fibrées entre atomes uniques et photons uniques*. phdthesis, Ecole normale supérieure - ENS PARIS, September 2015. URL https://theses.hal.science/tel-01382230.

[91] Gurpreet Kaur Gulati, Hiroki Takahashi, Nina Podoliak, Peter Horak, and Matthias Keller. Fiber cavities with integrated mode matching optics. *Scientific Reports*, 7(1):5556, July 2017. ISSN 2045-2322. doi: 10.1038/s41598-017-05729-8. URL https://www.nature.com/articles/s41598-017-05729-8. Number: 1 Publisher: Nature Publishing Group.

[92] Norman S. Nise. *Control systems engineering*. John Wiley & Sons, Inc., Hoboken, NJ, seventh edition edition, 2015. ISBN 978-1-118-80082-9. OCLC: 890971763.

[93] John G. Proakis and Dimitris G. Manolakis. *Digital signal processing*. Pearson Prentice Hall, Upper Saddle River, N.J, 4th ed edition, 2007. ISBN 978-0-13-187374-2. OCLC: ocm62804704.

[94] L. Neuhaus, R. Metzdorff, S. Chua, T. Jacqmin, T. Briant, A. Heidmann, P.-F. Cohadon, and S. Deléglise. PyRPL (Python Red Pitaya Lockbox) — An open-source software package for FPGA-controlled quantum optics experiments. In *2017 Conference on Lasers and Electro-Optics Europe & European Quantum Electronics Conference (CLEO/Europe-EQEC)*, pages 1–1, June 2017. doi: 10.1109/CLEOE-EQEC.2017.8087380.

[95] L. Neuhaus. Red Pitaya DAC performance, February 2016. URL https://ln1985blog.wordpress.com/2016/02/07/red-pitaya-dac-performance/.

[96] L. Neuhaus. Adding voltage regulators for the RedPitaya output stage, February 2016. URL https://ln1985blog.wordpress.com/2016/02/07/adding-voltage-regulators-for-the-redpitaya-output-stage/.

[97] H.H. Ku. Notes on the use of propagation of error formulas. *Journal of Research of the National Bureau of Standards, Section C: Engineering and Instrumentation*, 70C(4):263, October 1966. ISSN 0022-4316. doi: 10.6028/jres.070C.025. URL https://nvlpubs.nist.gov/nistpubs/jres/70C/jresv70Cn4p263_A1b.pdf.

[98] Monika H. Schleier-Smith, Ian D. Leroux, and Vladan Vuletić. States of an Ensemble of Two-Level Atoms with Reduced Quantum Uncertainty. *Physical Review Letters*, 104(7):073604, February 2010. doi: 10.1103/PhysRevLett.104.073604. URL https://link.aps.org/doi/10.1103/PhysRevLett.104.073604. Publisher: American Physical Society.

[99] J. G. Bohnet, K. C. Cox, M. A. Norcia, J. M. Weiner, Z. Chen, and J. K. Thompson. Reduced spin measurement back-action for a phase sensitivity ten times beyond the standard quantum limit. *Nature Photonics*, 8(9):731–736, September 2014. ISSN 1749-4893. doi: 10.1038/nphoton.2014.151. URL https://www.nature.com/articles/nphoton.2014.151. Number: 9 Publisher: Nature Publishing Group.

[100] J. Appel, P. J. Windpassinger, D. Oblak, U. B. Hoff, N. Kjærgaard, and E. S. Polzik. Mesoscopic atomic entanglement for precision measurements beyond the standard quantum limit. *Proceedings of the National Academy of Sciences*, 106(27):10960–10965, July 2009. doi: 10.1073/pnas.0901550106. URL https://www.pnas.org/doi/full/10.1073/pnas.0901550106. Publisher: Proceedings of the National Academy of Sciences.

[101] Kevin C. Cox, Graham P. Greve, Joshua M. Weiner, and James K. Thompson. Deterministic Squeezed States with Collective Measurements and Feedback. *Physical Review Letters*, 116(9):093602, March 2016. doi: 10.1103/PhysRevLett.116.093602. URL https://link.aps.org/doi/10.1103/PhysRevLett.116.093602. Publisher: American Physical Society.

[102] F. Piéchon, J. N. Fuchs, and F. Laloë. Cumulative Identical Spin Rotation Effects in Collisionless Trapped Atomic Gases. *Physical Review Letters*, 102(21):215301, May 2009. doi: 10.1103/PhysRevLett.102.215301. URL https://link.aps.org/doi/10.1103/PhysRevLett.102.215301. Publisher: American Physical Society.

[103] J. N. Fuchs, D. M. Gangardt, and F. Laloë. Internal State Conversion in Ultracold Gases. *Physical Review Letters*, 88(23):230404, May 2002. doi: 10.1103/PhysRevLett.88.230404. URL https://link.aps.org/doi/10.1103/PhysRevLett.88.230404. Publisher: American Physical Society.

[104] H. J. Lewandowski, D. M. Harber, D. L. Whitaker, and E. A. Cornell. Observation of Anomalous Spin-State Segregation in a Trapped Ultracold Vapor. *Physical Review Letters*, 88(7):070403, January 2002. doi: 10.1103/PhysRevLett.88.070403. URL https://link.aps.org/doi/10.1103/PhysRevLett.88.070403. Publisher: American Physical Society.

[105] X. Du, L. Luo, B. Clancy, and J. E. Thomas. Observation of Anomalous Spin Segregation in a Trapped Fermi Gas. *Physical Review Letters*, 101(15):150401, October 2008. doi: 10.1103/PhysRevLett.101.150401. URL https://link.aps.org/doi/10.1103/PhysRevLett.101.150401. Publisher: American Physical Society.

[106] E. P. Bashkin. Spin waves in polarized paramagnetic gases. *ZhETF Pisma Redaktsiiu*, 33:11, January 1981. URL https://ui.adsabs.harvard.edu/abs/1981ZhPmR..33...11B. ADS Bibcode: 1981ZhPmR..33...11B.

[107] C. Lhuillier and F. Laloë. Transport properties in a spin polarized gas, I. *Journal de Physique*, 43(2):197–224, February 1982. ISSN 0302-0738, 2777-3396. doi: 10.1051/jphys:01982004302019700. URL http://dx.doi.org/10.1051/jphys:01982004302019700. Publisher: Société Française de Physique.

[108] J. M. McGuirk, H. J. Lewandowski, D. M. Harber, T. Nikuni, J. E. Williams, and E. A. Cornell. Spatial Resolution of Spin Waves in an Ultracold Gas. *Physical Review Letters*, 89(9):090402, August 2002. ISSN 0031-9007, 1079-7114. doi: 10.1103/PhysRevLett.89.090402. URL https://link.aps.org/doi/10.1103/PhysRevLett.89.090402.

[109] L. Parisi, G. E. Astrakharchik, and S. Giorgini. Spin Dynamics and Andreev-Bashkin Effect in Mixtures of One-Dimensional Bose Gases. *Physical Review Letters*, 121(2):025302, July 2018. doi: 10.1103/PhysRevLett.121.025302. URL https://link.aps.org/doi/10.1103/PhysRevLett.121.025302. Publisher: American Physical Society.

[110] M. J. Martin, M. Bishof, M. D. Swallows, X. Zhang, C. Benko, J. von Stecher, A. V. Gorshkov, A. M. Rey, and Jun Ye. A Quantum Many-Body Spin System in an Optical Lattice Clock. *Science*, 341 (6146):632–636, August 2013. doi: 10.1126/science.1236929. URL https://www.science.org/doi/10.1126/science.1236929. Publisher: American Association for the Advancement of Science.

[111] A. D. Ludlow, N. D. Lemke, J. A. Sherman, C. W. Oates, G. Quéméner, J. von Stecher, and A. M. Rey. Cold-collision-shift cancellation and inelastic scattering in a Yb optical lattice clock. *Physical Review A*, 84(5):052724, November 2011. doi: 10.1103/PhysRevA.84.052724. URL https://link.aps.org/doi/10.1103/PhysRevA.84.052724. Publisher: American Physical Society.

[112] G. K. Campbell, M. M. Boyd, J. W. Thomsen, M. J. Martin, S. Blatt, M. D. Swallows, T. L. Nicholson, T. Fortier, C. W. Oates, S. A. Diddams, N. D. Lemke, P. Naidon, P. Julienne, Jun Ye, and A. D. Ludlow. Probing Interactions Between Ultracold Fermions. *Science*, 324(5925):360–363, April 2009. doi: 10.1126/science.1169724. URL https://www.science.org/doi/10.1126/science.1169724. Publisher: American Association for the Advancement of Science.

[113] N. D. Lemke, J. von Stecher, J. A. Sherman, A. M. Rey, C. W. Oates, and A. D. Ludlow. p-Wave Cold Collisions in an Optical Lattice Clock. *Physical Review Letters*, 107(10):103902, August 2011. doi: 10.1103/PhysRevLett.107.103902. URL https://link.aps.org/doi/10.1103/PhysRevLett.107.103902. Publisher: American Physical Society.

[114] J. E. Williams, T. Nikuni, and Charles W. Clark. Longitudinal Spin Waves in a Dilute Bose Gas. *Physical Review Letters*, 88(23):230405, May 2002. ISSN 0031-9007, 1079-7114. doi: 10.1103/PhysRevLett.88.230405. URL https://link.aps.org/doi/10.1103/PhysRevLett.88.230405.

[115] M. Ö. Oktel and L. S. Levitov. Internal Waves and Synchronized Precession in a Cold Vapor. *Physical Review Letters*, 88(23):230403, May 2002. ISSN 0031-9007, 1079-7114. doi: 10.1103/PhysRevLett.88.230403. URL https://link.aps.org/doi/10.1103/PhysRevLett.88.230403.

[116] M. Ö. Oktel and L. S. Levitov. Collective dynamics of internal states in a Bose-Einstein gas. *Physical Review A*, 65(6):063604, May 2002. ISSN 1050-2947, 1094-1622. doi: 10.1103/PhysRevA.65.063604. URL https://link.aps.org/doi/10.1103/PhysRevA.65.063604.

[117] A. M. Rey, A. V. Gorshkov, C. V. Kraus, M. J. Martin, M. Bishof, M. D. Swallows, X. Zhang, C. Benko, J. Ye, N. D. Lemke, and A. D. Ludlow. Probing many-body interactions in an optical lattice clock. *Annals of Physics*, 340(1):311–351, January 2014. ISSN 0003-4916. doi: 10.1016/j.aop.2013.11.002. URL https://www.sciencedirect.com/science/article/pii/S0003491613002546.

[118] Kurt Gibble. Keeping atoms synchronized for better timekeeping. *Physics*, 3:55, July 2010. doi: 10.1103/PhysRevLett.105.020401. URL https://physics.aps.org/articles/v3/55. Publisher: American Physical Society.

[119] E. G. M. van Kempen, S. J. J. M. F. Kokkelmans, D. J. Heinzen, and B. J. Verhaar. Interisotope Determination of Ultracold Rubidium Interactions from Three High-Precision Experiments. *Physical*

Review Letters, 88(9):093201, February 2002. doi: 10.1103/PhysRevLett.88.093201. URL https://link.aps.org/doi/10.1103/PhysRevLett.88.093201. Publisher: American Physical Society.

[120] Kurt Gibble. Decoherence and Collisional Frequency Shifts of Trapped Bosons and Fermions. *Physical Review Letters*, 103(11):113202, September 2009. doi: 10.1103/PhysRevLett.103.113202. URL https://link.aps.org/doi/10.1103/PhysRevLett.103.113202. Publisher: American Physical Society.

[121] Emily Davis, Gregory Bentsen, and Monika Schleier-Smith. Approaching the Heisenberg Limit without Single-Particle Detection. *Physical Review Letters*, 116(5):053601, February 2016. doi: 10.1103/PhysRevLett.116.053601. URL https://link.aps.org/doi/10.1103/PhysRevLett.116.053601. Publisher: American Physical Society.

[122] O. Hosten, R. Krishnakumar, N. J. Engelsen, and M. A. Kasevich. Quantum phase magnification. *Science*, 352(6293):1552–1555, June 2016. doi: 10.1126/science.aaf3397. URL https://www.science.org/doi/10.1126/science.aaf3397. Publisher: American Association for the Advancement of Science.

[123] Ian D. Leroux, Monika H. Schleier-Smith, and Vladan Vuletić. Orientation-Dependent Entanglement Lifetime in a Squeezed Atomic Clock. *Physical Review Letters*, 104(25):250801, June 2010. doi: 10.1103/PhysRevLett.104.250801. URL https://link.aps.org/doi/10.1103/PhysRevLett.104.250801. Publisher: American Physical Society.

[124] Onur Hosten, Nils J. Engelsen, Rajiv Krishnakumar, and Mark A. Kasevich. Measurement noise 100 times lower than the quantum-projection limit using entangled atoms. *Nature*, 529(7587):505–508, January 2016. ISSN 1476-4687. doi: 10.1038/nature16176. URL https://www.nature.com/articles/nature16176. Number: 7587 Publisher: Nature Publishing Group.

[125] Benjamin K. Malia, Julián Martínez-Rincón, Yunfan Wu, Onur Hosten, and Mark A. Kasevich. Free Space Ramsey Spectroscopy in Rubidium with Noise below the Quantum Projection Limit. *Physical Review Letters*, 125(4):043202, July 2020. doi: 10.1103/PhysRevLett.125.043202. URL https://link.aps.org/doi/10.1103/PhysRevLett.125.043202. Publisher: American Physical Society.

[126] Jocelyne Guena, Michel Abgrall, Daniele Rovera, Philippe Laurent, Baptiste Chupin, Michel Lours, Giorgio Santarelli, Peter Rosenbusch, Michael E. Tobar, Ruoxin Li, Kurt Gibble, Andre Clairon, and Sebastien Bize. Progress in atomic fountains at LNE-SYRTE. *IEEE Transactions on Ultrasonics, Ferroelectrics, and Frequency Control*, 59(3):391–409, March 2012. ISSN 1525-8955. doi: 10.1109/TUFFC.2012.2208. Conference Name: IEEE Transactions on Ultrasonics, Ferroelectrics, and Frequency Control.

[127] Andrew D. Ludlow, Martin M. Boyd, Jun Ye, E. Peik, and P. O. Schmidt. Optical atomic clocks. *Reviews of Modern Physics*, 87(2):637–701, June 2015. doi: 10.1103/RevModPhys.87.637. URL https://link.aps.org/doi/10.1103/RevModPhys.87.637. Publisher: American Physical Society.

[128] B. Barrett, A. Bertoldi, and P. Bouyer. Inertial quantum sensors using light and matter. *Physica Scripta*, 91(5):053006, April 2016. ISSN 1402-4896. doi: 10.1088/0031-8949/91/5/053006. URL https://dx.doi.org/10.1088/0031-8949/91/5/053006. Publisher: IOP Publishing.

Jose Alberto de la Paz Espinosa **27 octobre 2023**

Sujet : Amelioration de un horloge Atomique sur Puce avec des états du spin comprimés

Résumé : Les capteurs atomiques sont des dispositifs très sensibles utilisés dans les étalons de temps et de fréquence, la détection inertielle et les mesures de précision des champs électromagnétiques. Aujourd'hui, ils sont développés au point d'être limités par leur nature quantique, c'est-à-dire la limite quantique standard (SQL). Cette limite découle du comportement individuel et non corrélé des atomes utilisés. Toutefois, il a été démontré que l'on peut surmonter cette limite en générant des corrélations quantiques et un enchevêtrement entre les atomes. La preuve de principe de la génération d'intrication peut être accomplie via différents protocoles, mais cela a très rarement été fait dans des dispositifs de qualité métrologique. Dans cette thèse, nous utilisons une plateforme d'électrodynamique quantique en cavité (cQED) pour créer un type d'état corrélé quantique dit état comprimé de spin. Nous utilisons comme plateforme une horloge à atomes piégés sur puce (TACC) pour générer ces états intriqués. Ce dispositif de qualité métrologique nous permet d'étudier la dynamique due aux interactions de spin sur une longue échelle de temps, de l'ordre de la seconde. La stabilité de l'appareil est confirmée par une déviation fractionnelle de la fréquence d'Allan de 6×10^{-13} à 1 s, une performance battant les horloges à atomes compactes disponibles dans le commerce.

Mots clés : Metrologie quantique, Puce à atomes, Intrication, Horloge Atomique, États Comprimés de Spin, Electrodynamique Quantique en Cavité

Subject : Improving an Atomic Clock on a Chip via Spin-squeezing

Abstract: Atom sensors are highly sensitive devices used in time and frequency standards, inertial sensing and precision measurements of electromagnetic fields. Nowadays, they are developed to the extent that they can be limited by their quantum nature, i.e., the standard quantum limit (SQL). This limit arises from the individual and uncorrelated behaviour of the used atoms. However, it has been demonstrated that one can overcome this limit via the generation of quantum correlations and entanglement between the atoms. Proof of principle entanglement generation can be accomplished via different protocols, but this has very seldom been done in metrology-grade devices. In this thesis, we use a cavity quantum electrodynamics (cQED) platform to create a type of quantum correlated state named spin squeezed. We use as a platform a trapped-atom clock on a chip (TACC) to generate these entangled states. This metrology-grade device allows us to study the dynamics due to spin interactions in the long time scale, on the order of a second. The stability of the apparatus is confirmed by a fractional frequency Allan deviation of 6×10^{-13} at 1 s, a performance beating commercially available compact atom clocks.

Keywords: Quantum Metrology, Atom Chip, Entanglement, Atomic Clock, Spin-squeezed States, Cavity Quantum Electrodynamics